Surface Processes on Metal Worlds:

Space Weathering and Regolith Formation on

Metal-Rich Asteroids

By

John M. Christoph

A Dissertation Presented in Partial Fulfillment
of the Requirements for the Degree
Doctor of Philosophy

Approved January 2023 by the
Graduate Supervisory Committee:

Linda Elkins-Tanton, Chair
David Williams
Catherine Dukes
Thomas Sharp
James Bell III

ARIZONA STATE UNIVERSITY

May 2023

ABSTRACT

With the National Aeronautics and Space Administration (NASA) Psyche Mission, humans will soon have the first opportunity to explore a new kind of planetary body: one composed mostly of metal as opposed to stony minerals or ices. Identifying the composition of asteroids from Earth-based observations has been an ongoing challenge. Although optical reflectance spectra, radar, and orbital dynamics can constrain an asteroid's mineralogy and bulk density, in many cases there is not a clear or precise match with analogous materials such as meteorites. Additionally, the surfaces of asteroids and other small, airless planetary bodies can be heavily modified over geologic time by exposure to the space environment. To accurately interpret remote sensing observations of metal-rich asteroids, it is therefore necessary to understand how the processes active on asteroid surfaces affect metallic materials. This dissertation represents a first step toward that understanding. In collaboration with many colleagues, I have performed laboratory experiments on iron meteorites to simulate solar wind ion irradiation, surface heating, micrometeoroid bombardment, and high-velocity impacts. Characterizing the meteorite surface's physical and chemical properties before and after each experiment can constrain the effects of each process on a metal-rich surface in space. While additional work will be needed for a complete understanding, it is nevertheless possible to make some early predictions of what (16) Psyche's surface regolith might look like when humans observe it up close. Moreover, the results of these experiments will inform future exploration beyond asteroid Psyche as humans attempt to understand how Earth's celestial neighborhood came to be.

ACKNOWLEDGMENTS

This dissertation has been made possible by more people than I could possibly list. A few deserve specific mention and gratitude.

As my primary advisor, Lindy Elkins-Tanton has been incredible throughout the last six years. She took me on as a student at perhaps the busiest point in her career, while simultaneously leading the NASA Psyche Mission, the ASU School of Earth and Space Exploration, the Interplanetary Initiative, and within a year the Origins Project. Lindy went out of her way to make time for me, not only amidst all her other responsibilities, but also graciously accommodating my own mental health and executive functioning challenges as I learned to work with them. All of this was enabled by her paradigmatic focus on metacognition and self-assessment: rigorously asking myself how I know what I know, and what is the natural next step to learning what I'm trying to learn.

Dave Williams is the reason I came to SESE in the first place. Dave encouraged me to apply to ASU when I began looking at grad schools in 2014, helped recruit me to the program in 2015, and provided my first year and a half of advising in 2016-'17. It's thanks to him that I could jump into this long process with two feet and find the absolute limit of what I'm able to teach myself.

Cathy Dukes went from a collaborating lab PI at an external institution to providing more direct one-on-one advising than anyone. At a time when administrative barriers presented challenges for me to access lab equipment at ASU, Cathy and her research group welcomed me warmly into their facility and workflow. So much of what I now know, from the nuts-and-bolts work of experiment design to the nuances of writing a manuscript, I owe to Cathy's continued mentorship and generosity.

Tom Sharp has been invaluable in helping me truly master electron microscopy. Despite the meandering path of my prior SEM background and plenty of resulting mistakes, Tom always made sure to emphasize what I had done well and identify specific things I could improve. But beyond his expertise, Tom's thoughtful kindness made him approachable even when I felt most uncertain, enabling me to learn so much more.

Jim Bell was the last addition to my committee, but his earliest advice preceded my time at ASU. One crucial part of his book *The Interstellar Age* describes how despite academic challenges, participating on the Voyager team as a student provided validation that space would still be a viable career. That idea has helped get me through my own academic struggles, and I intend to carry it forward to every student I mentor in future.

Beyond my committee, I owe so much to all my research collaborators. Caixia Bu was literally instrumental in the work of Chapter 2, providing both expertise and many, many long hours to help run the ion irradiation experiments. Grace Minesinger stepped in at a key moment, taking ownership of the SDTrimSP modeling that proved crucial to Chapter 2's interpretations, and doing graduate-quality work as an undergraduate. Laura Chaves, Michelle Thompson, and one anonymous reviewer provided highly insightful feedback on Chapter 2 during peer review. Mark Loeffler provided patient assistance with the laser irradiation procedures in Chapter 3, even through repeated postponement due to logistical challenges and the COVID-19 pandemic. Simone Marchi generously offered both the ejecta samples analyzed in Chapter 4, as well as ongoing support interpreting the imagery I was able to obtain from them. Erik Asphaug opened so many doors in my first year and was invaluable through project and adviser selection. Laurence Garvie provided most of my samples through the Buseck Center for Meteorite Studies,

and helped catch a few critical errors of mine before they became insurmountable challenges. None of this work would have been possible without training, resources, and support from Si Phrasavath, Ken Mossman, Axel Wittmann, Mark Mangus, Diana Convey, and the entire Eyring Materials Center staff.

I am indebted to the NASA Psyche Mission for both funding and collegiate support for all my research. I also owe much to colleagues throughout planetary science for crucial insights that improved my work: Tim McCoy, Dara Laczniak, Jamie Molaro, Saverio Cambioni, Joe O'Rourke, Andy Rivkin, Carver Bierson, and so many others. Of course I can't omit my fellow grad students: C. Adeene Denton, Jessica Noviello, Genevieve Studer-Ellis, Sierra Ferguson, Lucia Perez, Tessa Fisher, Steven Dibb, Stephen West, Soumya Ray, Kevin Hubbard, Hannah Bercovici, Lena Heffern, Morgan Shusterman, Sean Czarnecki, Rhonda Holton, Dan Sullivan, Tyler Richey-Yowell, Linnea Ravacz, Zoë Stein, Mara Karageosian, Shawn Peters, Madison Borelli, Kevin Trinh, Sam Courville, Amanda Alexander, Claire Blaske, and all. Also, every grad student needs a good therapist; I can recommend none so highly as Dr. Daniel Schulte.

Beyond ASU, the greater Phoenix community enabled so many extracurricular outlets that kept me sane: United Campus Workers AZ, Tempe Transportation Commission, SMRHS, SWMDOT, the Urban Phoenix Project, All Aboard AZ, Equality AZ, Trans Spectrum AZ, and so many campaigns and projects to build a better world.

I must finally thank my family, who have been my rock throughout: Alex, Cher, all my cousins, aunts, uncles, James, and Mom. Last of all, I would like to dedicate this thesis to my dad, Dr. Richard A. Christoph, for whom I will always be so grateful that he got to watch me cross the finish line after 30 years of encouraging me to do my best.

TABLE OF CONTENTS

Page

LIST OF TABLES…….vii

LIST OF FIGURES……..viii

CHAPTER

1. Introduction…….....1

    1.1. Metallic Asteroids……...1

    1.2. Iron Meteorites……3

    1.3. Exploration of Metal-Rich Worlds: Linking Meteorites and Asteroids…..9

    1.4. Airless Body Surface Processes……12

2. SPACE WEATHERING EFFECTS IN TROILITE BY SIMULATED SOLAR-WIND HYDROGEN AND HELIUM ION IRRADIATION……16

    Abstract……17

    Plain Language Summary……17

    2.1. Introduction……...18

    2.2. Methods …….……..21

    2.3. Results ……..28

    2.4. Discussion ……38

    2.5. Conclusion…….54

    Acknowledgments……55

    References……56

3. LASER IRRADIATION OF IRON METEORITES: REGOLITH PARTICLE FORMATION BY THERMALLY DRIVEN MECHANICAL BREAKDOWN..67

CHAPTER Page

Abstract……67

3.1. Background…….....67

3.2. Methods ……...70

3.3. Results……...72

3.4. Discussion…….....78

3.5. Conclusion…….86

4. CHARACTERIZING EJECTA FRAGMENTS FROM CRATERING EXPERIMENTS INTO IRON METEORITES…….87

Abstract……87

4.1. Background……...87

4.2. Methods…….....94

4.3. Results……...97

4.4. Discussion…….....106

4.5. Conclusion…….....112

5. SYNTHESIS AND FUTURE WORK……114

REFERENCES ……124

APPENDIX

A. COAUTHOR PERMISSIONS FOR CHAPTER 2……..146

B. SUPPORTING INFORMATION FOR CHAPTER 2…….148

LIST OF TABLES

Table Page

1.1. The Iron Meteorite Chemical Groups……..7

4.1. Ejecta Fragment Morphological Types…….101

LIST OF FIGURES

Figure Page

1.1. Photo of a Cut, Polished, and Etched Piece of the Gibeon Iron Meteorite……...5

2.1. High-Magnification SEM Images of the Toluca and Canyon Diablo Polished Surfaces Before and After Irradiation……29

2.2. AFM Images Showing Un-irradiated and Irradiated Surfaces of Canyon Diablo…..30

2.3. Atomic Abundances of the Major Elements on the Canyon Diablo and Toluca Surfaces at Varying Fluences of H^+ and He^+ Ions...……..32

2.4. High-Resolution XPS Spectra for S and Fe Observed on Canyon Diablo…….35

2.5. SDTrimSP Modeling Estimate of the Surface-Oxide Depth for Each Meteoritic Troilite Section..…….37

2.6. Comparison of The Troilite Surface Composition as Measured by XPS After Removal of the Oxide Layer……..41

2.7. Inclusion of Damage-Driven Diffusion for Sulfur in the SDTrimSP Simulation……..46

2.8. SDTrimSP Model for the Final Composition of Troilite After 3.6×10^{18} (H, He)/cm^2 as a Function of Depth..……..49

2.9. Sulfur Depletion Quantified via SDTrimSP in the Outermost Monolayer for Exposed Troilite Deposits within Psyche's Surface Regolith Over Time……52

3.1. Three Views of the Polished Thick Section of Canyon Diablo …….……71

3.2. Secondary Electron Image Centered on the Edge of a Laser Spot on Bulk Kamacite…….73

Figure Page

3.3. An SEM Image of the Top-Left Corner of a Laser Spot Irradiating the Schreibersite Inclusion and the Cohenite Rim…….74

3.4. The Same Laser Spot as Shown in Figure 3.3, but Focusing on the Cohenite Rim…….75

3.5. Higher-Magnification SEM Images of the Smooth Plates near the Center of Figure 3.4 and the Rough Surface Immediately Above Them.…….76

3.6. SEM Image of a Laser-Irradiated Troilite surface……..77

4.1. Cartoon Depictions of Fracture Modes in Metals..…….89

4.2. The Crater in the Center of the Target Block after Impact…….95

4.3. Backscatter Electron Image Mosaic of 291 Ejecta Fragments……...97

4.4. Size-Frequency Distribution of the Ejecta Fragments……98

4.5. Backscatter Contrast on the Exposed Faces of Some Fragments…….100

4.6. A Petal-Like Fragment……..102

4.7. A Branching Fragment……..102

4.8. A Portion of the Largest Fragment, Showing Interlocking Grains……...104

4.9. Two Fragments Exhibiting Plastic Deformation Larger than the Santiago Papasquiero Grain Size……106

CHAPTER 1: INTRODUCTION

Hardly mere barren, featureless rocks floating between the planets, the asteroids have proven endlessly complex subjects of scientific study. Human exploration of the solar system's minor bodies has only commenced in earnest within my lifetime, and only a handful of such objects have been imaged up close out of over a million identified to date with ground-based telescopes. Yet each successive mission to the asteroids has revealed ever more exciting novelties, with the promise of additional wonders to be found on those myriad tiny worlds we know only as lonely pixels wandering across the paths of sky surveys. Astronomical evidence suggests a portion of the asteroids are composed mostly of metal, but humans have never seen a metal-rich asteroid up close. Meteorites composed of iron abound in museum and university collections, but their origin remains mysterious. Seeking answers by merging these two scientific enigmas only created a greater enigma still: a type of asteroid we've yet to visit is the most likely parent body of a type of rock we've yet to find the source of – a liminal prediction, testable but not yet tested. The imminent exploration of such a metal-rich world by the NASA Psyche Mission grants this multifaceted enigma renewed priority, motivating the work begun as part of this dissertation.

1.1. Metallic Asteroids

The first classification of metallic asteroids as a taxonomic group was by Zellner and Gradie (1976), who introduced the M-type as a specific optical reflectance pattern, alongside the then-established S- and C-types with different reflectance patterns (Zellner 1973, Chapman et al. 1975). The Tholen (1984) classification system retained Zellner and Gradie's (1976) definition of the M-types and their metallic interpretation while

placing them into the X-group along with the brighter E-type and darker P-type asteroids. Subsequent asteroid taxonomies, including SMASS (Burbine and Binzel 2002) and the current Bus-DeMeo (DeMeo et al. 2009, DeMeo et al. 2020) have redefined the scope of this group into the X-complex, which includes both the featureless and red-sloped X-class spectra, as well as Xc, Xe, Xk, and Xn classes with faint absorption features at specific wavelengths. While the "X-class" is thus the most technically appropriate term for these asteroids, the "M-type" designation and its accompanying interpretation of a highly metal-rich composition are still commonly invoked in both public-facing communication and scientific writing (Burbine 2017).

Two primary lines of evidence suggest a metallic composition for the X-class asteroids: optical reflectance spectra and radar albedo. Optical reflectance spectroscopy takes advantage of absorption of photons from the Sun at specific wavelengths due to crystal field transitions (Burns 1993), interatomic charge transfer (Rossman and Ehlmann 2020), and atomic vibration (Clark 1999), all of which can be linked to specific minerals present on the asteroid's surface. Radar albedo refers to the fraction of a transmitted radar signal that returns from an object in space with the same polarization (Ostro 1993), which is a function of the bulk density, conductivity, and roughness of the material composing the object (Campbell 2002).

Crucially, the information depth of both radar and optical remote sensing techniques is related to the wavelength of the signal photon (Sabins 1997, Campbell 2002). Thus, while visible and infrared observations provide information about the uppermost few microns of an asteroid's surface (Burbine 2017), the longer wavelength of radar enables characterization of planetary surfaces and sub-surfaces at depths ranging

from tens of centimeters to hundreds of meters, depending on the instrument (Campbell 2002). While a lack of features in optical reflectance spectra might non-uniquely indicate the surface of an asteroid is metal-rich, the high radar albedo of M-type or X-class asteroids indicates their subsurface compositions are also metal-rich (Ockert-Bell et al. 2010).

Given the evidence pointing to a metal-rich composition for the M-type/X-class asteroids, identifying an analogous metallic material is a natural next question. The prevailing interpretation since the initial M-type classification (Zellner and Gradie 1976) has been iron meteorites. However, as discussed below, linking iron meteorites to asteroids raises numerous complexities.

1.2. Iron Meteorites

The precise origin of iron meteorites has long posed an enigmatic scientific problem. It is easy enough to discern they fell from space, as they fall onto people's property or homes by circumstance, are sometimes tracked by human eye or radar as they fall, are often covered by a fusion crust formed during atmospheric entry, and contain isotopic abundances inconsistent with terrestrial origin (Buchwald 1975, Grady et al. 2014). The petrology of iron meteorites more specifically points to an origin by igneous processing in the interiors of differentiated worlds.

Structurally, iron meteorites can be classified into *hexahedrites*, *octahedrites*, and *ataxites*, based on how they cooled from molten metal, which is controlled by the abundance of Ni and P (Yang and Goldstein 2005). The iron-nickel alloy that makes up the bulk of iron meteorites consists of two predominant minerals: kamacite (α-FeNi, <6 wt.% Ni) and taenite (γ-FeNi, >25 wt.% Ni) (Buchwald 1975). When a FeNi alloy

crystallizes from melt, as during planet formation and differentiation in the early Solar System, taenite is the initially stable solid phase regardless of Ni abundance. However, as the metal cools, taenite becomes unstable and can undergo a variety of solid-solution phase transitions depending on the cooling rate and the precise position of the metal on the Fe-Ni-P phase diagram, with three possible resulting structures (Grady et al. 2014). Hexahedrites, labeled "H," undergo a complete transition from single-crystal taenite to single-crystal kamacite. Octahedrites, labeled "O," exsolve kamacite lamellae along the octahedral lattice planes of the taenite crystals, producing a distinctive Widmanstätten structure visible when samples are polished and acid-etched. Octahedrites can be further sub-classified by the thickness of these kamacite lamellae, with the coarsest lamellae labelled "Og" and "Ogg" being >3 mm wide, through mm-scale medium lamellae labeled "Om," to the finest lamellae labeled "Of" and "Off" < 0.2 mm wide, and even finer plessitic kamacite spindle structures labeled "Opl" (Grady et al. 2014). Ataxites, labeled "D" have the finest structures of all iron meteorites, featuring a microscopic Widmanstätten structure.

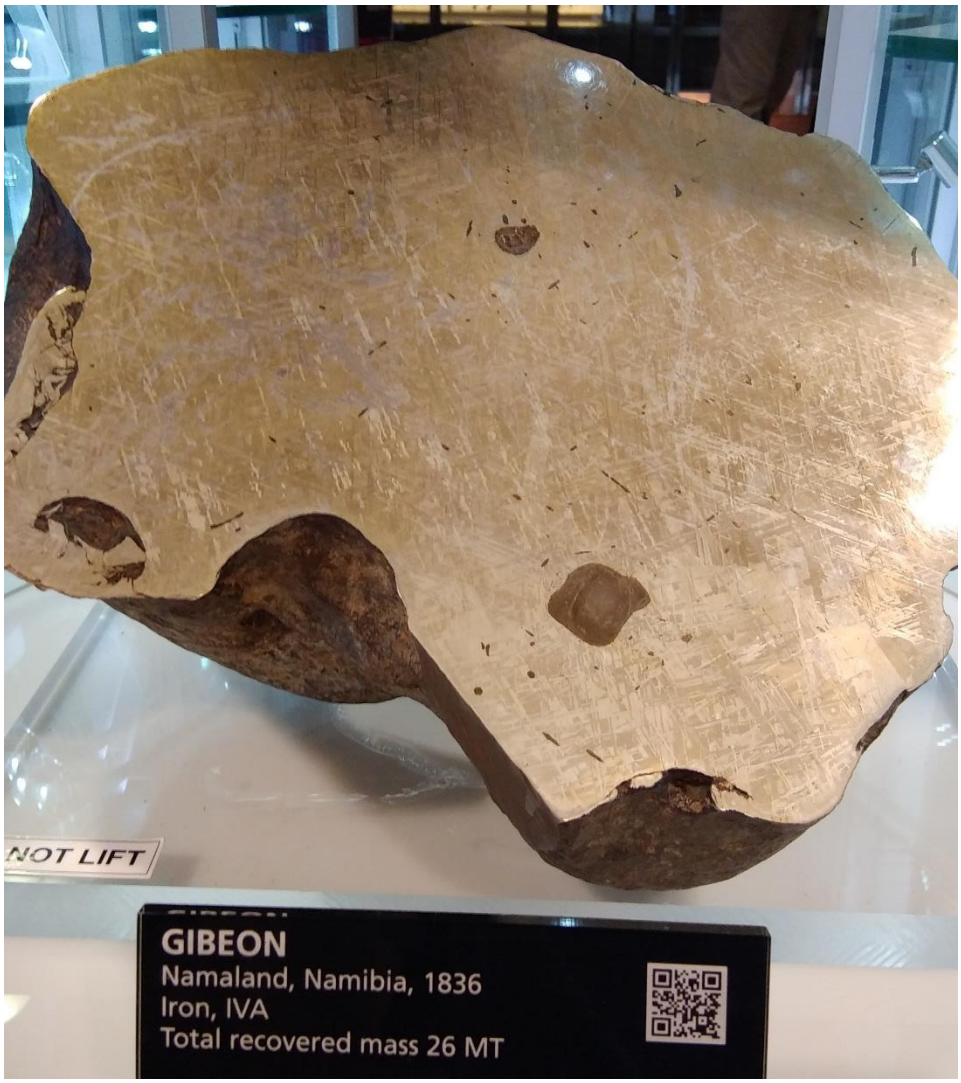

Figure 1.1 A photo by the author of a cut, polished, and etched piece of the Gibeon iron meteorite, a Group IVA fine octahedrite (Of), on display at the Buseck Center for Meteorite Studies at Arizona State University. The dark brown lower surface is the fusion crust that formed when the meteorite entered Earth's atmosphere. The Widmanstätten structure can be seen as three parallel sets of lineations across the flat, silvery, metal surface. Irregular round inclusions of accessory minerals such as troilite and graphite are also visible throughout the interior of the metal.

Chemically, iron meteorites are grouped based on their abundances of Ni, Ga, Ge, Ir, and Au, using a system developed by Wasson and colleagues over multiple decades (Wasson 1967, Wasson 1998). From the outset, these crystallization behaviors could be traced to specific processes that occurred on a particular meteorite's parent body as it

formed. The resulting groups can be broadly related in turn to the structural classification, since both are related to bulk Ni abundance. While these formation processes and their corresponding groups have been repeatedly re-interpreted over time, meteoriticists have recently been able to link specific iron meteorite cosmochemical groups to other stony and stony-iron meteorite taxonomies: the IAB and IIICD groups are linked to the winonaite primitive achondrites by silicate inclusions (Weisberg et al. 2006); the IIE group is linked to the H chondrites by silicate inclusions (Wasson and Wang 1986); the IIIAB group shares chemical features with pallasites (Wasson 1999), though they cooled at different rates (Yang and Goldstein 2006, Yang et al. 2010); and the IVA group may be related to L-LL chondrites (Wasson and Richardson 2001). Overall, there are 13 presently recognized iron meteorite groups (Grady et al. 2014), plus 147 individual iron meteorites that do not fit within any of the groups (Meteoritical Bulletin 2023), suggesting there are at least 13 iron meteorite parent bodies. These chemical groups are summarized in Table 1.1, with their corresponding structural classification, Ni abundance, and number of samples.

Group Name	Structure	Ni wt.% range	Quantity
IIG	H – Ogg	4.18 – 4.64	6
IIAB	H – Ogg	5.35 – 6.04	146
IC	Og	6.1 – 7.0	13
IIIF	Om – Of	6.8 – 8.5	9
IIE	Og – Om	6.1 – 10.6	25

IIIE	Og	7.81 – 9.6	19
IIIAB	Og – Om	7.57 – 10.2	345
IVA	Of	7.32 – 11.1	89
IID	Om – Of	9.6 – 11.1	29
IIC	Off – Opl	9.3 – 11.5	8
IAB-IIICD	Og – Off	6.68 – 17.7	365
IIF	Opl – D	10.6 – 14.3	7
IVB	D	15.9 – 18.0	18
Ungrouped	Varies	Varies	147

Table 1.1 The iron meteorite chemical groups, listed in increasing order of median Ni wt.% abundance. Structure data from Table 15.2 in (Grady 2014). Ni abundance data from (Moore et al. 1969). Quantity data from (Meteoritical Bulletin 2023).

The relationship between the chemical groups and the structural classification derives from the specific phase transitions that occur as the taenite cools. Many different mechanisms have been proposed for the formation of the FeNi Widmanstätten lattice, of which five occurred in iron meteorites (Yang and Goldstein 2005). In a pure FeNi alloy with >6 wt.% Ni, kamacite cannot nucleate directly from single-crystal taenite without significant under-cooling (Allen and Earley 1950), referred to as “Mechanism I” (Yang and Goldstein 2005). However, the presence of P within the metal enables crystallization of kamacite by entering the taenite + kamacite + phosphide phase field. In iron meteorites with high P abundance, phosphide minerals like schreibersite ($[FeNi]_3P$) form as the taenite cools, which causes the remaining metal to enter the kamacite stability field (Goldstein and Doan 1972); this process is referred to as “Mechanism II” (Yang and Goldstein 2005). In iron meteorites with low P abundance, the metal can enter the

kamacite stability field, but kamacite crystals do not actually nucleate until the metal reaches P-saturation (Narayan and Goldstein 1984); this is referred to as "Mechanism III" (Yang and Goldstein 2005). Alternatively, in the absence of phosphorus, kamacite can nucleate after taenite has cooled enough to undergo martensitic transformation (Owen 1940, Buchwald 1966). This is referred to as "Mechanism IV" if kamacite nucleates after taenite completely transforms to martensite (Yang and Goldstein 2005), or "Mechanism V" if kamacite nucleates while the taenite to martensite transition is incomplete (Yang and Goldstein 2003, Yang and Goldstein 2005). Since P abundance varies among members of each chemical group (Buchwald 1975, Goldstein et al. 2009), most groups' parent bodies would have experienced multiple cooling mechanisms, but the most numerous groups can be linked with one or more specific mechanisms. In particular, Group IVA can only have been produced by Mechanism V, Group IIIAB experienced all but Mechanism I, and plessitic structures are most likely associated with Mechanism IV (Yang and Goldstein 2005). Hexahedrites, which have <6 wt.% Ni lack a Widmanstätten structure, can undergo complete recrystallization of taenite to kamacite via a massive transformation, or by Mechanism V (Yang and Goldstein 2005).

With detailed modeling of iron meteorites' crystallization processes, it is possible to constrain the cooling rates and thus the core formation time scales of their parent bodies. Multiple simulation techniques have been developed over decades of work, with subsequent iterations replicating diagnostic iron meteorite petrologic features such as kamacite bandwidth, taenite Ni content, phosphide growth, and formation of cloudy zone structures with increasing fidelity (Goldstein et al. 2009). Cooling rate estimates vary among members of each iron meteorite chemical group, not just due to differences in

simulation method, but also due to the fact that the exteriors of planetesimal cores would lose heat more rapidly than their interiors. Nevertheless, consistent cooling rate estimates are possible for each chemical group, which combined with petrologic analysis permit detailed assessment of their parent bodies' formation histories, including their diameters, bulk composition, internal structure, and history of disruption (Grady et al. 2014).

1.3. Exploration of Metal-Rich Worlds: Linking Meteorites and Asteroids

With constraints on the petrology and crystallization history of iron meteorites, a search for their parent bodies is a natural next step. However, conclusive evidence linking iron meteorites to M-type/X-class asteroids has proven elusive. Two specific interplanetary missions, as well as the long-running discourse on asteroid resource extraction, illustrate why.

The ESA Rosetta mission flew past asteroid (21) Lutetia in 2010, *en route* to its primary rendezvous with comet 67P (Barucci et al. 2005). Lutetia was first observed in 1852 by Hermann Goldschmidt and had been initially interpreted as an M-type asteroid by Tholen (1984) and a possible iron meteorite parent body (Bowell et al. 1978, Dollfus et al. 1979). However, as the Rosetta mission approached, ground-based observations began to reveal an extremely fine dust-covered surface (Feierberg et al. 1983), optical absorption features consistent with non-metallic surface composition (Birlan et al. 2006, Belskaya et al. 2010), and lower radar albedo than previously measured (Ockert-Bell et al. 2010). Correspondingly, in the immediate lead-up to the Rosetta flyby Lutetia was predicted to have a surface composition consistent with either carbonaceous chondrites (Birlan et al. 2006, Barucci et al. 2008, Lazzarin et al. 2009, Belskaya et al. 2010), enstatite chondrites (Vernazza et al. 2009), or mesosiderites (Vernazza et al. 2009). The

observations Rosetta made during its flyby showed that while Lutetia has a high overall density requiring a metal-rich interior (Pätzold et al. 2011), its surface is an extremely fine-grained silicate regolith (Massironi et al. 2012), consistent with a body that only partially differentiated (Weiss et al. 2012, Formisano et al. 2013, Neumann et al. 2013).

The NASA Psyche Mission was proposed in 2013, selected as the fourteenth mission of the Discovery Program in 2017, is currently scheduled to launch in October 2023, and plans to orbit asteroid (16) Psyche in 2029. Unlike Rosetta, the primary science goals of the Psyche Mission are to explore a metal-rich asteroid for the first time, characterize the geophysical properties of this novel type of world, determine if it is indeed a remnant planetesimal core, or investigate how else it might have formed if it is not a remnant core (Elkins-Tanton et al. 2020). First observed in 1852 by Annibale de Gasparis, Psyche is the largest Tholen (1984) M-type asteroid, though it is classified Xk-type by Bus-DeMeo (2009). Unlike Lutetia, radar observations of Psyche and mass estimates from orbital dynamics suggest it is indeed mostly composed of metal (Shepard et al. 2017). Although Psyche's optical reflectance spectrum does show evidence of silicate minerals on its surface (Landsman et al. 2016) and possibly even hydrated minerals (Takir et al. 2017), recent ALMA millimeter-wave observations suggest that this stony material may be intimately mixed with metal on Psyche's surface (de Kleer et al. 2021), a finding reinforced by laboratory experiments showing that no single meteorite provides a one-to-one match for Psyche's optical spectrum (Dibb et al. 2021). In any case, while Psyche undoubtedly has a high metal fraction in its bulk composition, possibly higher than any planetary body humans have explored to date (Elkins-Tanton et

al. 2020), the best evidence available suggests a far more complex surface than a simple iron meteorite analog.

Beyond these scientific missions, metallic asteroids have become perennial objects of interest among private actors as targets for notional asteroid mining. The earliest technical proposals for asteroid mining (Lewis and Nozette 1983) focused on identifying the useful materials that could potentially be extracted from meteorite analogs, including Fe alloys from metallic asteroids with compositions similar to iron meteorites, albeit with a focus on uses in space to facilitate exploration. Kargel (1994) proposed that platinum-group elements could be profitably mined and returned to Earth, either from the metal fraction of an asteroid analogous to an ordinary chondrite or from a metallic asteroid analogous to an iron meteorite. These ideas were subsequently popularized by public-facing literature produced by scientists in the field (Lewis 1996). The prospect of mining metallic asteroids has pushed the United States Congress to explicitly legalize extraction and use of materials US companies obtain from planetary surfaces (Space Resource Exploration and Utilization Act, 2015) and multiple firms have started up with asteroid mining as an explicit goal, such as Planetary Resources in 2012, Deep Space Industries in 2013, and AstroForge in 2021. While subsequent studies have explored both the technical (Gertsch et al. 2006, Lewis 2016) and economic (Heln et al. 2020) viability of an asteroid mining business case, none of these firms has yet initiated a mission to rendezvous with, let alone extract or return samples from, an asteroid. Even for those enterprises possessing both the capital and technical expertise to support such a mission, any venture premised on obtaining meteorite-analog materials from an asteroid

must face the same challenges that publicly funded scientific missions face in attempting to link specific meteorites to specific asteroids.

Lutetia and Psyche point to some of the challenges of linking meteorites to asteroids in general. Although iron meteorites as a group are the best match for X-class asteroid spectra, no specific iron meteorites, nor even metal-rich meteorites of other types, are perfect matches (Dibb et al. 2021). While radar and optical remote sensing suggest the X-class asteroids generally have metal-rich compositions, for many individual X-class asteroids the predicted metal contents measured by these two techniques are inconsistent with each other (Ockert-Bell et al. 2010). Even in past cases where a meteorite group has been linked to a specific asteroid, such as the Howardite-Eucrite-Diogenite clan and (4) Vesta, the interpreted link faced enough contradictory evidence to be disputed (Schiller et al. 2011, Wasson 2012) until up-close exploration by the NASA Dawn mission established the link conclusively (McSween et al. 2013). Commercial ventures to extract asteroid resources are fundamentally constrained by the uncertainty that any given asteroid will match its proposed meteorite analogs, limiting their potential contributions to asteroid exploration. Finally, and most relevant for this thesis, airless planetary surfaces exposed to the space environment are significantly modified over geologic time, as discussed below.

1.4. Airless Body Surface Processes

When searching for a physical process to explain an observation in planetary science, meteoritic impacts are often the first candidate for investigation (Greeley 2013). Impacts occur at all sizes from microscopic to cataclysmic, however the size-frequency distribution of crater populations on rocky planets suggests that smaller impacts

uniformly occur more frequently than larger ones (Neukum et al. 1974). As a result, while a large impact might fracture a solid surface and form a crater that excavates and redeposits large blocks of material across a planetary surface, smaller impacts will progressively break down those boulders into finer and finer regolith particles (Gault 1970). Subsequent large impacts can then overturn and "garden" the regolith, resulting in a complex, multi-layered stratigraphy (Melosh 2011). On small bodies with low enough gravity that significant fractions of ejecta from cratering impacts can escape to space rather than falling back onto the surface, impact-driven fracturing of boulders may be sufficient to produce a rubble-pile regolith without crater excavation (Cambioni et al. 2021, Ballouz et al. 2023). A mature regolith composed of a thick layer of fine-grained particles processed many times over can display a reflectance spectrum with diminished absorption features as compared to fragmented breccia composed of the same minerals (Clark et al. 2002).

Recently it has been recognized that regolith particles can form without impacts, by a process known as thermal fatigue. "Fatigue" in materials science refers to cyclic or periodic stress applied over time (Meyers and Chawla 2010). On an airless planetary surface, such stresses can be applied as the body rotates on its axis: the Sun-facing side heats up and thermally expands, while the opposite side cools and contracts (Molaro and Byrne 2012). On objects with highly elliptical orbits or highly inclined rotation axes, there can be multiple overlapping cycles of thermal expansion and contraction, corresponding to diurnal, annual, or seasonal illumination cycles (Bierson et al. 2022). As the surface material expands, fractures present on the surface will also expand and thus propagate through the material, which cannot reverse during the cooling stage. Thus,

slowly over many repeated cycles, large blocks can be broken down into finer particles, without the need for high-energy impacts which may eject the fine particles into space. Fatigue is particularly important on small bodies such as asteroids with negligible surface gravity, as observed on Bennu and Ryugu (Molaro et al. 2017, 2020).

The other major process occurring on airless planetary surfaces is space weathering. For decades it has been understood that exposure to the space environment causes changes in the spectra and albedo of airless planetary bodies, including the Moon (Gold 1955, Hapke 2001) and asteroids (Chapman 1996). A variety of mechanisms have been interpreted to cause these spectroscopic changes, with the most prominent being solar wind ion irradiation (Hapke 2001) and micrometeorite impact (Sasaki et al. 2001). The relationship between these two mechanisms is complex. Ion irradiation can cause chemical reduction and sputtering from the sample surface (e.g., Dukes et al. 1999, Noguchi et al. 2014, Tanyeli et al. 2015), while also producing a variety of structural features, including amorphized rims and nanophase iron particles (npFe) in iron-bearing minerals (Auciello 1984, Gaffey et al. 1993, Keller and McKay 1997, Pieters et al. 2000). Meanwhile, recent evidence indicates that a combination of both processes may be necessary to achieve the observed differences in some remote-sensing data (Loeffler et al. 2008, Thompson et al. 2019). Observations of Fe whisker growth on returned lunar and asteroid samples point to additional complexly interrelated contributions of ion irradiation and heat to space weathering (Matsumoto et al. 2020, 2021).

Our knowledge of these surface processes is still incomplete even on planetary bodies we have explored for decades, yet on metal-rich asteroids the open questions are fundamental. How would a metallic surface change if exposed to the space environment

over geologic time? How would we observe and measure those changes? How might the cumulative modification of billions of years influence our interpretations of how these asteroids formed? How would we apply knowledge of surface processes on metal worlds to better understand other planetary surfaces throughout the Solar System?

These questions broadly motivate this dissertation, which investigates three specific space weathering and regolith formation mechanisms on metallic asteroid analog materials. Chapter 2 summarizes work done to simulate solar wind space weathering, by irradiating samples of iron meteorite inclusions with hydrogen and helium ions. Chapter 3 explores the role thermal stress would play in mechanically modifying a metallic asteroid, with laser irradiation experiments on iron meteorite samples. Chapter 4 discusses the ejecta produced during an impact into an iron meteorite target, using electron microscopy to characterize the fragments' fracture surfaces and corresponding mechanical deformation modes. Finally, Chapter 5 synthesizes the conclusions from these experiments, discusses their implications for the surface of asteroid Psyche, and explores the scope of future investigations, both planned and notional.

CHAPTER 2: SPACE WEATHERING EFFECTS IN TROILITE BY SIMULATED SOLAR-WIND HYDROGEN AND HELIUM ION IRRADIATION

J. M. Christoph[1], G. M. Minesinger[2], C. Bu[2,3], C. A. Dukes[2], and L. T. Elkins-Tanton[1]

[1]School of Earth and Space Exploration, Arizona State University, Tempe, AZ 85287

[2]Laboratory of Astrophysics and Surface Physics, University of Virginia, Charlottesville, VA 22904

[3]Columbia Astrophysics Laboratory, Columbia University, New York, NY 10027

Corresponding author: John M. Christoph (jmchri17@asu.edu)

Key Points:

- We irradiated samples of meteoritic troilite (iron sulfide) with H^+ and He^+ ions, simulating solar wind space weathering.
- We observed nanoscale roughening of the surface and formation of a sulfur-depleted layer as the irradiations progress.
- Using SDTrimSP modeling in combination with XPS, we quantify the surface oxide layer thickness, diffusion rate, altered-layer composition, and fluence-dependent sputtering yield.

Abstract

Space weathering is a key process in the interpretation of airless planetary surfaces. As we engage new missions to planetary objects with potentially novel surfaces such as 16 Psyche, there is renewed interest in expanding our knowledge of space weathering effects to a wider variety of analog materials, including the physical/chemical effects of solar-wind ions on planetary regoliths. We have experimentally simulated the effects of solar ions on two polished thick sections of meteoritic troilite (FeS) via irradiation with 1 keV hydrogen (H^+) and 4 keV helium (He^+), to investigate effects resulting from different ion species. We detected depletion of sulfur over the course of each irradiation using in-situ X-ray photoelectron spectroscopy (XPS). Sulfur depletion rates were surprisingly similar for H^+ and He^+, interpreted as a function of subsurface ion-activated diffusion. By comparing XPS-derived elemental abundances with SDTrimSP computer simulations, we further quantified sulfur diffusion, sputtering yield, and altered-layer composition with respect to incident-ion fluence, and accounted for the influence of surface oxidation due to atmospheric sample storage. Using scanning electron microscopy (SEM), we detected an increase in nanoscale surface roughness resulting from the irradiation, which we quantified using atomic force microscopy (AFM). Based on these results, we estimate an exposure time of order 10^3 Earth-years is required for troilite on Psyche to reach equilibrium sulfur depletion within the first atomic-layer.

Plain Language Summary

The NASA Psyche Mission will visit the metallic asteroid Psyche for the first time in 2026. Because metallic asteroid surfaces are expected to be compositionally

distinct from the rocky surfaces of asteroids previously visited by spacecraft, we must characterize the effects of the space environment on expected constituent materials to correctly interpret observational data at Psyche. Solar-wind irradiation is one process in the space environment that significantly changes the surface composition, reflectance and micro-structure of silicate minerals ubiquitous in rocky asteroid soils. We simulated solar-wind interaction with troilite (FeS), a common mineral found in iron meteorites and expected on Psyche, with hydrogen and helium ions in the laboratory. These simulations showed us that over time solar wind preferentially removes sulfur, enriching the mineral surface in iron, and roughens the surface at the nanoscale. These observed changes replicate observations in natural troilite returned from the asteroid Itokawa. Removal of sulfur and surface roughening could both affect how the instruments on the NASA Psyche Mission take measurements of the asteroid surface and how we interpret those measurements.

2.1. Introduction

Airless planetary surfaces are constantly bombarded by energetic particles, photons, and meteorites from the surrounding space environment, altering their optical, physical, or chemical properties; these interactions are known as "space weathering." Space weathering by solar-wind ions – the continuous stream of hydrogen, helium, and trace amounts of heavier elements radiating out from the sun with an average energy of ~1 keV/amu – was identified as a mechanism to explain spectral variation of Lunar crater rays with age and distance, and optical differences between returned Apollo soils and crushed regolith rocks (e.g. Gold 1955, Hapke 2001, Pieters and Noble 2016, Farrell et al. 2015). More recently, the spectral differences between asteroids and meteorite samples (Chapman

1996, Dukes et al. 1999) were also attributed to solar-wind irradiation. Radiation-exposed surfaces of mafic minerals decrease in albedo and become redder in overall reflectance over time, with commensurate attenuation of absorption features (Hapke 2001; Loeffler et al. 2009). On lunar grains and in Fe-bearing minerals such as olivine, these spectral effects have been associated with the formation of nanophase iron (npFe) particles within the amorphous rims of weathered surfaces (Gaffey et al. 1993, Keller and McKay 1997, Pieters et al. 2000, Matsumoto et al. 2021). Though a number of additional mechanisms have been proposed to play a role in formation of space weathering textures, including micrometeoroid impacts (Sasaki et al. 2001, Loeffler et al. 2016) and other sources of heating (Thompson et al. 2017), irradiation of surfaces by solar-wind ions is considered the principal weathering mechanism on asteroids (Schläppi et al. 2008), directly linked to the formation of npFe and iron-cladding on exposed surfaces (Noguchi et al. 2014; Matsumoto et al. 2020). Moreover, research on metals and oxides has identified other damage modes associated with light-ion irradiation at energies similar to solar-wind ions, such as phase-change, pitting, and blistering (Auciello 1984, Tanyeli et al. 2015, Kajita et al. 2016, Meyer 2018).

Much space weathering work historically focused on silicate minerals, the major mineral components of ordinary chondrites – the most abundant meteoritic type – which are linked to S-type asteroids (e.g., Clark et al. 1992, Gaffey et al. 1993, Pieters et al. 2000, Nakamura et al. 2011). Other minerals have received less attention. Only a small number of studies have investigated space-weathering effects on iron meteorites or their major mineral components (Loeffler et al. 2008, Harries and Langenhorst 2014, Bezaeva et al. 2015, Wu et al. 2017, Prince et al. 2020, Matsumoto et al. 2020, 2021). While there have

been extensive engineering studies on the effect of the space environment on structural metals for spaceflight applications, these synthetic materials are poor analogs for iron meteorites due to their orders-of-magnitude smaller crystal sizes and differing microstructures, both resulting from the inability to synthetically crystallize materials over geologic timescales (Petrovic 2011). Given that we have not yet visited a metallic asteroid with spacecraft (Elkins-Tanton et al. 2020) and the difficulties in identifying asteroids that have metallic surfaces (Rivkin et al. 2000, Landsman et al. 2015, Sanchez et al. 2017, Takir et al. 2017, Elkins-Tanton et al. 2020), any understanding of space weathering effects on iron meteorites as an analog for naturally-occurring metallic planetary surfaces must begin from laboratory experiments.

Troilite is the predominant sulfide mineral present in chondritic meteorites, one of the most common inclusions in iron meteorites (Grady et al. 2014), and possibly present on the Psyche surface or bulk (Elkins-Tanton et al. 2020). Previous studies invoked space weathering by solar wind to explain sulfur depletion observed at the near-Earth asteroid 433 Eros (Nittler et al. 2001, Killen 2003, Kracher and Sears 2005). Experimental work to test this hypothesis has used helium and/or argon ion irradiation to simulate solar wind and laser irradiation to simulate meteoritic impact space weathering. These experiments identified a two-step mechanism – sputtering initiated by incident solar-wind protons, and subsequent partial melting and vaporization by micrometeoroid impacts – depleting sulfur by a factor of 1.5-2.5 over a period of 10^4-10^5 years (Loeffler et al. 2008, Thompson et al. 2019). Recent laboratory studies point to the evolution of a surficial layer of metallic iron and subsurface iron-rich sulfide with ion irradiation (Keller et al. 2013). Additional studies have characterized space weathering effects on composition and microstructure of natural

troilite grains returned from 25143 Itokawa, (Harries and Langenhorst 2014, Matsumoto et al. 2020) and Apollo lunar samples (Matsumoto et al. 2021), identifying micron- and sub-micron-scale iron whiskers forming on the porous, amorphized, and sulfur-depleted surfaces of troilite grains.

We report the results of laboratory irradiation experiments using troilite thick-section samples from iron-meteorite inclusions, using protons and helium ions to better simulate the solar wind and identify species-specific differences. Using X-ray photoelectron spectroscopy (XPS) measurements and SDTrimSP computer simulations, we identify and characterize changes to surface composition and chemistry as a function of ion fluence and compare differences in sputtering by 1keV/amu H^+ and He^+. We also perform scanning electron microscopy (SEM) and atomic force microscopy (AFM) measurements to determine roughness originating during irradiation, which may play a role in altering the albedo and reflectance spectra of surfaces exposed to space, beyond the formation of npFe and loss of sulfur. Results from these experiments will be useful for the interpretation of observations from the NASA Psyche mission (Elkins-Tanton et al. 2020).

2.2. Methods

2.2.1. Samples

The Center for Meteorite Studies (CMS) at Arizona State University provided two polished thick sections of troilite-nodule inclusions taken from the Canyon Diablo and Toluca iron meteorites. We used polished thick sections instead of pressed powder slabs to optimize measurement of potential irradiation-induced surface roughness. While loose or pressed powder is generally considered an analog for fine-grained regoliths on airless planetary objects (e.g., Loeffler et al. 2008), Psyche may present us with a potentially novel

type of planetary surface (Elkins-Tanton et al. 2020) for which a powder sample may not be appropriate. Both Canyon Diablo and Toluca sections have been characterized with wavelength-dispersive X-ray spectroscopy (WDS) calibrated against standardized pyrite and olivine to confirm their bulk composition is 50 at% S, 50 at% Fe, <1% other.

2.2.2. Irradiation and In-Situ Characterization

Irradiation and in-situ characterization of the samples were performed at the University of Virginia. Samples were ultrasonically cleaned in an isopropanol bath before irradiation to remove any organic contaminants from sample handling. We irradiated the Canyon Diablo sample with only He^+ using an electron-bombardment-type ion gun on a PHI Versaprobe III XPS. We then irradiated the Toluca sample first with 4 keV helium (He^+) ions, followed by 1 keV hydrogen (H^+) ions using a similar ion gun on a highly-customized PHI-560 XPS system. The use of an initial He^+ irradiation on both samples allowed the removal of surficial oxide and ensured that we could compare the results of H^+ and He^+ irradiation on similarly-prepared sulfide surfaces. Details of the experimental setup can be found in Supplementary Text (S1) and have been described in earlier works (e.g., Dukes et al. 1999, Laczniak et al. 2021).

Both irradiations were designed to reach a comparable target fluence (~3×10^{18} ions/cm^2), enabling direct comparison between proton and helium irradiation. The target fluence falls in the saturation range of S-depletion observed previously for 4 keV He^+ irradiation of FeS pressed pellets (Loeffler et al. 2008). The average solar-wind flux at 1AU from the Sun is 2×10^8 ions/cm^2/s, consisting of ~96% H^+, ~4% He^+, and heavier highly-charged ions less than 0.1% (Johnson 1990). Since solar-wind flux decreases proportional to the square of the distance from the Sun, the target fluence of 3×10^{18} ions/cm^2 simulates

exposure times of ~100,000 years for He^+ and ~4000 years for H^+ at 16 Psyche (semi-major axis ~2.9 AU). To reach the target fluence in a practical laboratory time frame, we used an average flux of ~1×10^{13} ions cm^{-2} s^{-1}. In both systems, low energy electrons (< 5 eV) from an electron flood gun prevent surface charging of the sample during irradiations and XPS analysis. The samples were at room temperature (300 K) during irradiation and characterization.

2.2.3. X-ray Photoelectron Spectroscopy

X-ray photoelectron spectroscopy (XPS) is a quantitative surface analytical technique, providing concentration and chemical state information for elements within the top monolayers of a material (less than 10 nm). On both PHI560 and Versaprobe III, Al-K_α X-rays ($E_{x\text{-}ray}$ = 1486.6 eV) interact with the samples, producing photoelectrons ejected into the vacuum with a characteristic kinetic energy (E_k) given by $E_k = E_{x\text{-}ray} - E_B - \Phi$, where Φ is the measured work function of the spectrometer, and E_B is the binding energy of the core-level (or valence) electron with respect to the Fermi level. Photoelectrons from deeper in the material lose energy as they travel through the solid and contribute to the spectral background. The measured energy distribution of the ejected electrons is displayed as counts/s *vs.* E_B. The area of an individual photoelectron peak after background subtraction, together with the corresponding normalization ("sensitivity") factor, is used to obtain elemental abundance, while the peak position (E_B) and shape give information on the chemical state of the element.

In this work, the S-2p, O-1s, C-1s, and Fe-3p photoelectron peaks were selected for troilite compositional determination; spectral background due to inelastically scattered electrons was subtracted using the iterative-Shirley method (Shirley 1972). We chose the

Fe-3p feature with its low background for use in quantification, as the Fe-3p and S-2p features provide information from a similar sampling depth – critical for direct comparison of S:Fe abundance. However, the Fe-2p region, which is complicated by dual spin-orbital features, multiplet splitting and energy-loss satellites, exhibits greater sensitivity to chemical change and was monitored in the high-resolution XPS data sets. For more detail, see the Supplemental Section Figures S1 and S2, which show survey and high-resolution XPS spectra respectively, including Fe-3p and Fe-2p photoelectron peaks.

We confirmed our derived elemental concentrations utilizing manufacturer-provided instrument-specific sensitivity factors (Multipak v9.8, Wagner et al. 1981), by comparison with results utilizing the Fe-2p3/2 and full Fe-2p feature with both Wagner et al. (1981) and Loeffler et al. (2008) sensitivity factors; compositions were in agreement within 26% for each element/method. Versaprobe instrument sensitivity factors were confirmed by measurement of freshly-cleaved pyrite, analyzed in the same manner (Fe-3p and S-2p) immediately upon fracture and found to be appropriately stoichiometric (S:Fe = 2.05 ± 0.05); Loeffler et al (2008) did not measure a sensitivity factor for the Fe-3p."

2.2.4. Sample Imaging and Surface Roughness Characterization

We imaged the polished samples using the FEI XL30 Field-Emission Environmental Scanning Electron Microscope (SEM) at ASU's Eyring Materials Center. We obtained images at >20,000x magnification of the sample surfaces *before* irradiation, as well as images at the center of the irradiation spot and outside the irradiation spot *after* irradiation to identify any radiation-induced changes to the surface roughness, topography, or texture. Because troilite is weakly conductive, we were able to obtain high-resolution

images operating the XL30 at low electron-beam voltage (5 kV) without carbon-coating the sample.

After confirming that the irradiated surface had roughened in the SEM measurements, we quantified the change in surface roughness using the Bruker Dimension 3000 Atomic Force Microscope (AFM) at ASU's Eyring Materials Center with a NCHV-A probe in tapping mode. AFM measures the height (Z) of successive points across the sample surface by measuring the slight deflection of the nano-scale probe as it interacts with the surface. The probe rasters across a square subdivided into 512 × 512 probe measurement points. By decreasing the size of the square, the distance between probe measurement points decreases, enabling roughness characterization across a range of length scales. We selected squares with sizes: 2 × 2, 5 × 5, and 20 × 20 μm, at locations within the irradiated area and without any visible large scratches or other features not obviously caused by irradiation. Once the raster image is obtained, MM-8 software included in the Dimension 3000 calculates the Z range, average, and standard deviation, as well as the projected surface area of the rastered region. To minimize the statistical influence of pre-irradiation roughness, we then selected smaller sub-regions within the 512 × 512 point raster images which displayed minimal height variation from sample polishing scratches and re-calculated the same statistics.

2.2.5. SDTrimSP Modeling

SDTrimSP 6.0 is a 1D Monte Carlo simulation that uses the binary-collision approximation to model atomic-collision processes for projectiles incident on amorphous targets, both gaseous and condensed (Mutzke et al. 2019). This method improves upon some of the known limitations with the SRIM simulations, which do not model accurately

the effects of non-normal projectile incidence, sputtering yield angular distributions, multicomponent sputtering yields, and interpolated stopping powers; comparisons of SDTrimSP output to experimental data are detailed in Hofsäss et al. (2014) and others (e.g. Arredondo et al. 2019; Wittmaack and Mutzke 2017) along with a discussion of limitations and error. The program can output ion ranges, sputtering yields, reflection coefficients, damage cascades, target compositions as functions of depth or fluence, and specific target atom/molecule information such as: trajectories, energies, exit angles, vacancies, and displacements for comparison with measured parameters (e.g., Szabo et al. 2020a; Stadlymayr et al. 2018; Wittmack and Mutzke 2017). Unlike its predecessor, SRIM (Ziegler et al. 1985), SDTrimSP provides (1) the option for a dynamic mode, which periodically updates the stoichiometry of the target throughout the simulation, (2) incorporates outgassing and diffusion of both projectiles and target atoms, (3) includes chemical sputtering for carbon, (4) allows additional changes in atomic interaction potential, (5) facilitates multiple "concurrent" projectile types and energy/velocity distributions, and (6) provides a new inelastic energy model for projectiles exceeding 25 keV. The user can modify many parameters including the method to solve the scattering angle and time integrals, the surface binding-energy model, and the atomic/molecular interaction potential model. Our simulations typically used the recommended Gauß-Legendre integration method; atom-specific surface binding-energy "model two;" and the KrC interaction potential. The resulting target-compositional output of the SDTrimSP simulations of H^+ and He^+ irradiation on troilite can be directly compared to experimental data – such as XPS spectra – and used to predict the effects of solar-wind ion impact on airless planetary surfaces, such as Psyche.

We ran SDTrimSP with variations of 4 keV He^+ and 1 keV H^+ normally incident on a planar target, using the laboratory flux of ~1×10^{13} ions/cm^2/s to a fluence of ~3×10^{18} ions/cm^2 in order to identify optimal parameters for surface binding energy and diffusion. The upper-surface composition of the Canyon Diablo and Toluca samples were modeled with 150 Å and 46 Å oxide layers, respectively (see Section 3.4). Both oxides are atop a target composed of FeS. The outermost surfaces of the modeled targets were ~3 Å of adventitious carbon, typical of most atmosphere-exposed materials (Sinha and Mukherjee 2017; Barr and Seal 1995). The sample temperature was defined to be 300 K, consistent with laboratory measurements. Projectile ions and sulfur target atoms were allowed to diffuse via radiation-enhanced diffusion and outgassing, where levels were controlled via their respective diffusion coefficient inputs. Undefined inputs, such as diffusion coefficients, surface binding energies, and sample oxide characteristics, were manipulated in these simulations to produce data that most closely resembles that from our experiments.

2.2.6. Conversion of SDTrimSP Output to XPS Information Depth

SDTrimSP provides compositional atomic fractions on a monolayer scale, while XPS provides elemental atomic fractions of the integrated upper surface (~50 Å) as a function of fluence. Thus, to directly and quantitatively compare the simulation results to those from the lab, SDTrimSP outputs require conversion to match the XPS information depth.

Photoelectrons from deeper in the target are less likely to be detected in XPS, due to their increased interactions within the solid. Thus, the likelihood of detecting a photoelectron (and thus, its parent atom) is dependent on depth and the electron inelastic mean free path

(IMFP) within the target (e.g., Powell 2020). The IMFP was calculated for each (element) photoelectron using the NIST SRD71 TPP-2M model (Powell and Jablonski 2010) with a density of 4.74 g/cm^3 for FeS (Skala et al. 2006). The signal intensity (I_d) from each atomic layer can be described as:

$$I_d = I_s \times e^{-\left(d \cdot \frac{\cos\theta}{\lambda}\right)} \quad \text{Eq (1)}$$

where I_s is the photoelectron intensity from the surface layer, d is the depth, θ is the photoelectron detection angle (45°) with respect to the surface normal, and λ is the IMFP. To convert modeled data to XPS composition, an individual SDTrimSP simulation must be run where the final fluence is the respective XPS fluence. For each of those simulations, the final atomic fraction at each depth was weighted per Eq (1) for the individual element through the first 7.5 nm, then summed and normalized. Because XPS cannot detect helium or protons, the atomic fractions of the implanted helium or protons were not included in this normalization.

2.3. Results

2.3.1. Ion-induced surface roughness

SEM images of both Canyon Diablo and Toluca sample post-irradiation clearly show the development of nanoscale ion-induced surface texturing. Fig. 2.1 shows high-magnification images (20,000x) comparing outside and inside the irradiated region on both Canyon Diablo and Toluca. For both samples, the surface outside the irradiated area is smooth apart from striated scratches made during sample polishing. These polishing scratches are observed also within the irradiated area, overlain by additional pitting and other roughness features at a length scale smaller than 10 nm, a result of ion bombardment.

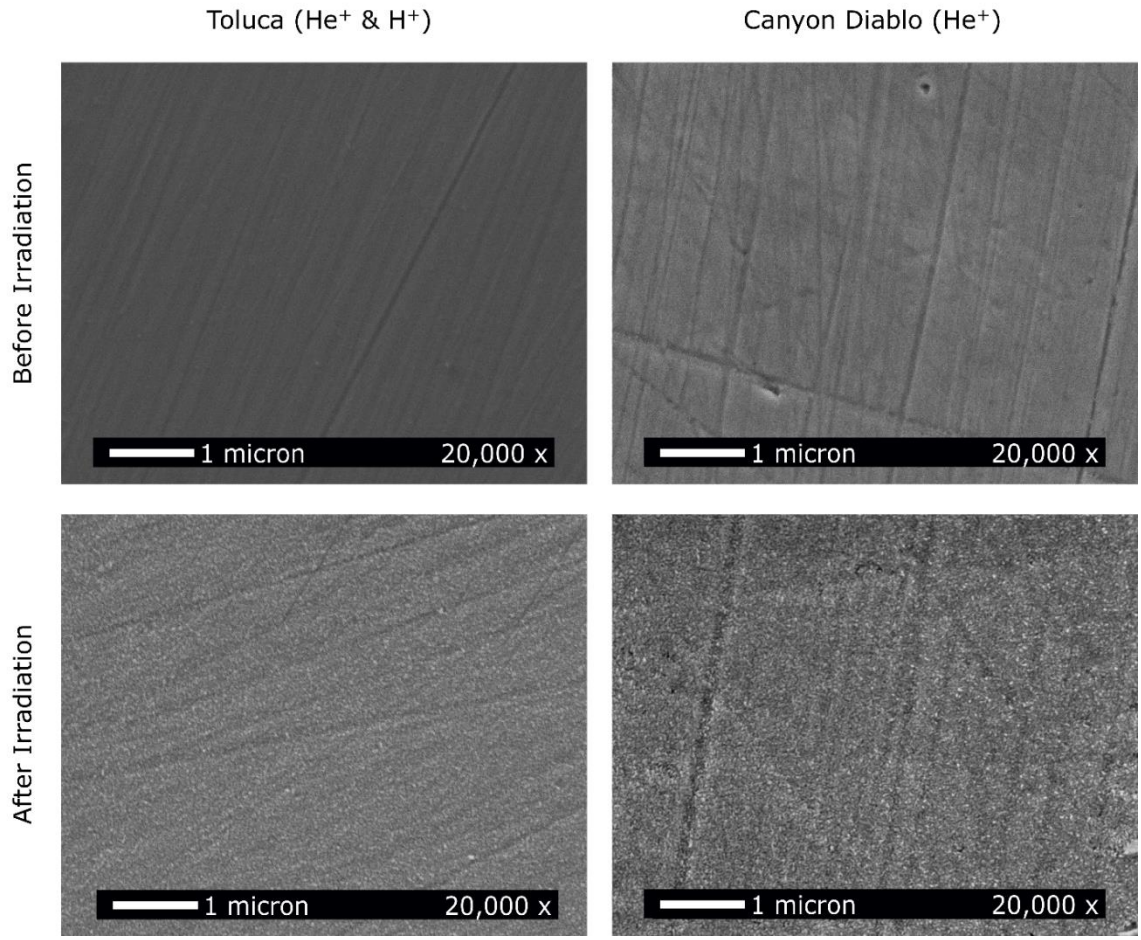

Figure 2.1. High-magnification (20kx) SEM images of the Toluca and Canyon Diablo polished surfaces outside the irradiated area and within the irradiated surfaces showing nanoscale texturing by both 1 keV H and 4 keV He.

The AFM surface roughness measurements were similar across both samples (Fig 2.2). On the un-irradiated surfaces, the average of the Z standard deviations across eight AFM measurement sites was 2.36 +/- 0.25 nm for Canyon Diablo and 2.26 +/- 0.25 nm for Toluca. On the irradiated surfaces, the average of the Z standard deviations was 5.94 +/- 0.36 nm for Canyon Diablo and 5.49 nm +/- 0.41 for Toluca.

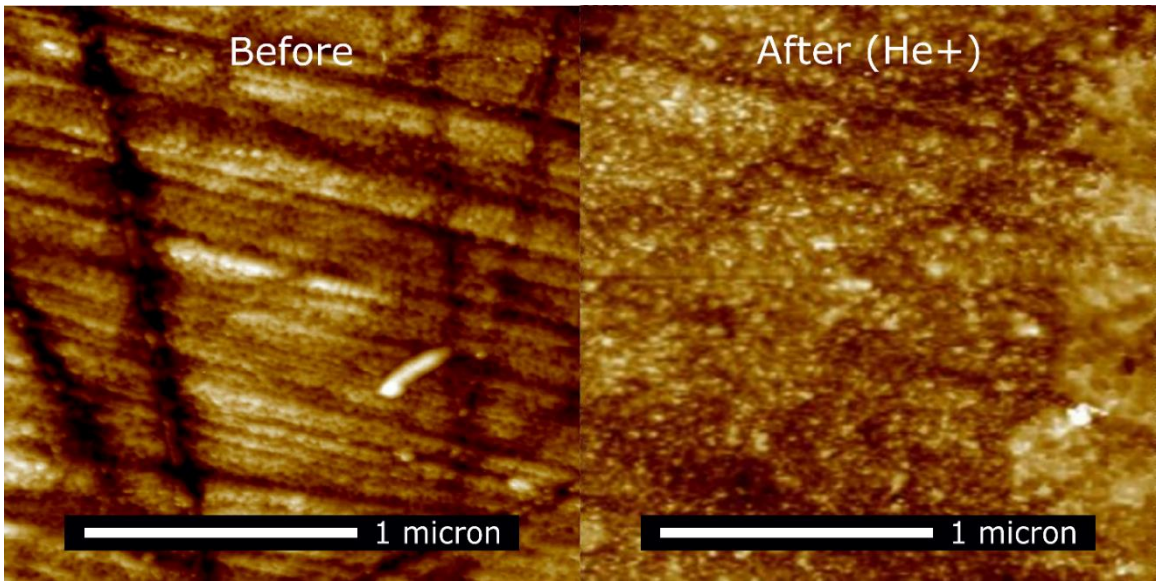

Figure 2.2. AFM images showing the un-irradiated (left) and irradiated (right) surfaces of Canyon Diablo; both images are 2-micron squares.

2.3.2. Surface Compositional Change:

Figure 2.3 shows the elemental abundances of Fe, S, O, and C with fluence as measured by XPS on the Canyon Diablo and Toluca samples. At low fluences on both samples, we observed a S:Fe ratio lower than the expected 1:1 stoichiometric ratio for troilite due to the presence of a surface oxide. Oxide formation occurs rapidly on iron sulfide exposed to O_2 in the atmosphere, as well as with the polishing required for SEM and AFM measurements. As this oxide layer was removed by sputtering during the early stage of the irradiation, the S:Fe ratio reached a relative maximum, after which it decreased as sulfur was preferentially removed.

On the Canyon Diablo sample, after removal of the surface oxide layer (described below), we measured a maximum S:Fe ratio of 0.60 at a fluence of 4.8×10^{17} He^{+}/cm^{2}, after which the S:Fe ratio decreased with continued irradiation (Fig. 2.3a) to a final S:Fe

ratio of 0.36 at the end of irradiation. The oxide-troilite interface is identified as the region where the surface oxide is reduced to 50%, after irradiation by 3.2×10^{17} He^{+}/cm^{2}.

For the Toluca sample, irradiated with primarily protons, the S:Fe ratio is largest at 0.51 with 2.6×10^{17} ions/cm^{2} (Fig. 2.3b). Again, after removal of the surface oxide (described below), we observed sulfur loss for fluences above 2.6×10^{17} ions/cm^{2}. The final S:Fe ratio for the Toluca sample after a fluence of 6×10^{16} He^{+}/cm^{2} and then at 2.8×10^{17} H^{+}/cm^{2} was 0.22. The oxide-troilite interface at 50 % of the maximum oxygen concentration is found at a total fluence of 2.4×10^{17} ions/cm^{2}. Carbon appears within and above the oxide layer for Toluca, and with proton irradiation both carbon and oxygen appear well-beyond the fluence identified as the interface, suggesting a broader interface region potentially due to a reduced sputtering yield by protons in the oxide layer. Indeed, we found that the O was retained in the Toluca FeS at higher concentrations after the interface than for Canyon Diablo, even after ~3×10^{18} ions/cm^{2}. This is consistent with sputtering yield measurements and models for metal oxides, which find that protons sputter 10^{-1} less efficiently compared with helium (Betz and Wehner 1983; Schaible et al 2017).

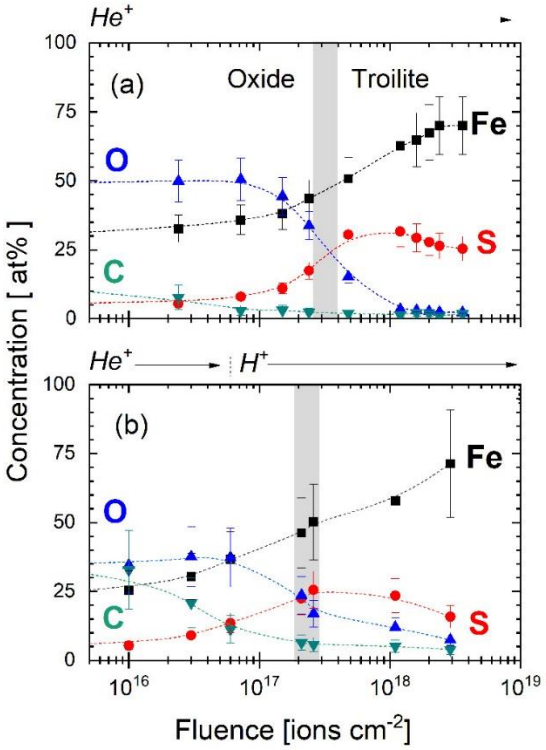

Figure 2.3. Atomic abundances of the major elements on the Canyon Diablo (a) and Toluca (b) surface at varying fluences of H^+ and He^+ ions. The gray bar indicates the fluence where the interface between the surface oxide coating and bulk troilite is reached.

2.3.3. Fe and S Surface Chemistry:

Photoelectron binding energies are sensitive to the difference between the surface-atom final-state and ground-state configurations and reflect the local chemistry. We examined the chemical state of the Canyon Diablo and Toluca surface layers, using high-resolution (low pass-energy) XPS spectra. Fig. 2.4 shows the Fe2p and S2p regions measured at 1.5×10^{17} He^+/cm^2, just before the oxide-surface interface for Canyon Diablo, and again at the end of the 4 keV He irradiation (3.6×10^{18} He^+/cm^2). Spectra for the O1s and C1s peaks were also collected (see Fig. S5). For Toluca, the surface chemistry was analyzed after 6.6×10^{16} He^+/cm^2 and again after additional irradiation with 2.8×10^{18}

H^+/cm^2. No difference in chemical state was noted between proton and helium irradiations to imply the formation of new hydrogenated species, although the extent of chemical reduction was greater for 4 keV He^+. Results are described below in detail for the Canyon Diablo sample; the Toluca spectra are broadly similar.

As the precise surface potential for troilite is unknown during XPS acquisition, the binding-energy scale must be referenced for each spectral-acquisition dataset. Adventitious carbon (C-1s = 284.8 eV) was used to affix the absolute binding-energy scale, with subsequent spectra adjusted to the dominant sulfur (S-2p) feature, which showed no significant chemical change with irradiation (Fig. 2.4a). The S-$2p_{3/2}$ and S-$2p_{1/2}$ photoelectron peaks were fit with an area ratio of 2:1 to three doublets corresponding to: S^{2-} (troilite), S_2^{2-} and S_n^{2-} (surface defects) with a binding-energy separation constrained by troilite measurements of Terranova et al. (2018). With irradiation, the fractional abundance of the sulfur initially increases as the sulfur-poor surface oxide is removed and the underlying troilite is sampled by XPS.

Once the material sampled is exclusively troilite, the S:Fe ratio is observed to decrease under both He^+ and H^+ impact. The primary (~70%) S-$2p_{3/2}$ peak at 161.5 eV is indicative of native Fe-S bonds as expected for troilite (Fig. 2.4a) (Schaible et al. 2019; Loeffler et al. 2008). Features due to defects as well as bond-breaking and reformation with irradiation, e.g., S_n^{2-}, increased ~3.7% with 4 keV He^+ (Fig. 2.4a) and 1 keV H^+. We observed no spectral shifts in the S-2p feature that would indicate the formation of new species such as SOH (~163 eV) or adsorbed/trapped H_2S (~162.8 eV) with proton impact. No indication of S-O bonding was apparent at ~168 – 169 eV that would indicate S-O

bonds (Terranova et al. 2018; Loeffler et al. 2008; Thomas et al. 2003); thus, any surface sulfates have been removed by a fluence of 1.5×10^{17} He^{+}/cm^{2}.

The Fe-2p photoelectron peaks, a well-separated spin couplet, within Canyon Diablo and Toluca show a convolution of features from the iron-oxide surface, the bulk troilite, and sulfur-depleted iron after irradiation. For the Canyon Diablo sample just prior to the oxide-troilite interface at ~1.5×10^{17} He^{+} cm^{-2}, Fe-S bonds ($Fe2p_{3/2}$: 707.25 eV) make up only ~10.5% of the observed Fe; Fe(II)-O bonds (~17.5% $Fe2p_{3/2}$: 708.3eV with ~19% $Fe2p_{3/2}$ shakeup: 713.6eV) and Fe(III)-O (~53% $Fe2p_{3/2}$: 710.7 eV) in the surface oxide comprise the remainder (Bagus et al. 2021; Biesinger et al. 2011; Descostes et al. 2000; Brion 1980).

The prevalence of Fe(III)-O is consistent with a measured O:Fe ratio of ~1.5 in the survey spectra (Fig 2.3a), indicating a native Fe_2O_3-type surface oxide. With irradiation Fe-molecular bonds are broken by the kinetic energy transferred to the solid, preferentially sputter removing oxygen (Fig. 2.4b) (Dukes et al. 1999; Loeffler et al. 2008). After 3.6×10^{18} He^{+}/cm^{2}, ~15% of the Fe remains as intact Fe-S, while the primary (65% of the signal) $Fe2p_{3/2}$ photoelectron peak appears at 706.4 eV, indicative of Fe-Fe bonds (Fe^{0}) based on electron binding energy (Mcintyre and Zetaruk, 1977; Dukes et al. 1999; Skinner et al. 2004). This interpretation is also consistent with Fe-Fe at ~706 eV for a subsequent measurement of Fe^{0} in 99.95% Fe metal slug (Alfa Aesar), as well as with published values (e.g., Biesinger et al. 2011; Idczak et al. 2016). The remaining $Fe2p_{3/2}$ photoelectron feature(s) (~20%) indicate a small amount of Fe-oxide remains within the near-surface, likely due to ion-induced shadowing (roughness) during sputtering and sputter-induced layer mixing. This interpretation is consistent with information from the O1s photoelectron feature, which decreases in intensity by > 90% (see Fig. S5). A small shift to lower electron

binding energy (283.8 eV) is observed with irradiation for recoil-implanted C-1s; a change in surface potential was considered, but contraindicated by resulting inconsistent O, S, and Fe chemistry. Instead, the C-1s shift suggests the formation of a minor concentration (<1 at%) of iron carbide (Goretski et al 1989) or a transition in the carbon sp-hybridization. While no differences in chemical outcome were observed between H^+ and He^+ irradiations, the extent of change over the course of the irradiation was slightly lower for protons (22% Fe-Fe; 32% Fe-S; ~45% Fe oxides). The reduced rate of change for protons in comparison to helium is consistent with previous work on olivine (Dukes et al. 1999).

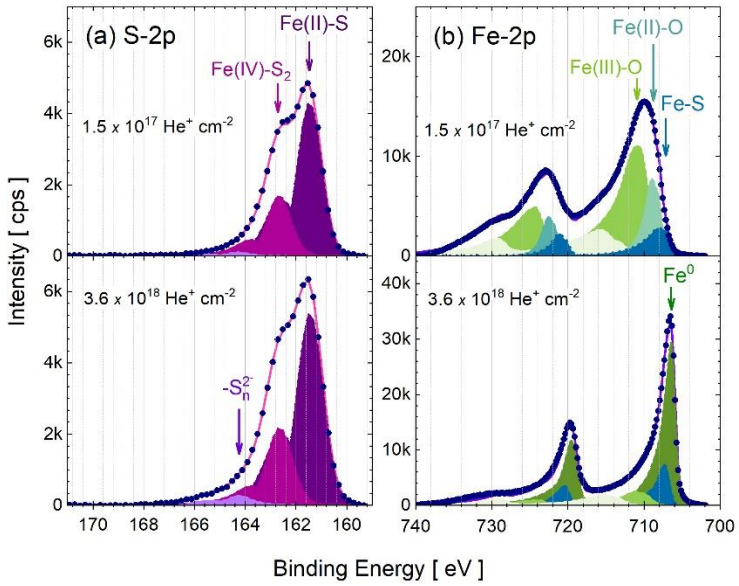

Figure 2.4. High-resolution XPS spectra for S (a) and Fe (b) observed on Canyon Diablo describe changes in chemistry with fluence, where the differently shaded photoelectron peaks indicate distinct chemical states. (a) The S-2p$_{3/2}$ and 2p$_{1/2}$ photoelectron peaks show that the surface sulfur remains primarily troilite S^{2-}, with a minor increase in concentrations of S_2^{2-} and S_n^{2-} ion-induced defects. (b) At low fluence significant Fe(II)-O (cerulean) and Fe(III)-O (light olive) features are apparent from atmospheric exposure along with FeS, while at higher fluence the oxide and troilite (blue) are chemically reduced to Fe^0 (dark olive). Energy loss features (lightest green) also appear when oxide is present. Although the magnitude of both S-2p and Fe-2p features was observed to increase with removal of surface oxide and adventitious carbon, the ratio of S:Fe is reduced (e.g., Fig. 2.3).

2.3.4. Oxide Layer Composition and Thickness Estimate:

To estimate the thickness of the oxide layers on our samples, we used the XPS-measured surface composition. This is 45.4 at% Fe, 44.9 at% O, 7.0 at% S, 1.3 at% N, 1.0 at% F, and 0.3 at% Ca for Canyon Diablo, as detected before any ion irradiation – without the contribution of adventitious carbon, which resides atop the oxide layer. After defining the oxide composition, we varied the thickness of the oxide layer in SDTrimSP to best fit the ion-induced depletion rate of oxygen to that of the XPS data, while also matching the measured Fe and S data. Based on the minimized chi^2 for all data points, oxide layers with thickness ~15 nm and ~4.6 nm respectively atop the Canyon Diablo and Toluca samples most accurately matched the SDTrimSP simulation to the XPS measurements (Fig. 2.5). XPS showed some remaining oxygen (2.5% and 7.5%) in the samples after irradiation to a fluence of $\sim 3 \times 10^{18}$ He^+/cm^2, while the SDTrimSP simulations indicate <0.1% remaining – likely resulting from the 1D simulation not accounting for surface roughness (Szabo 2018).

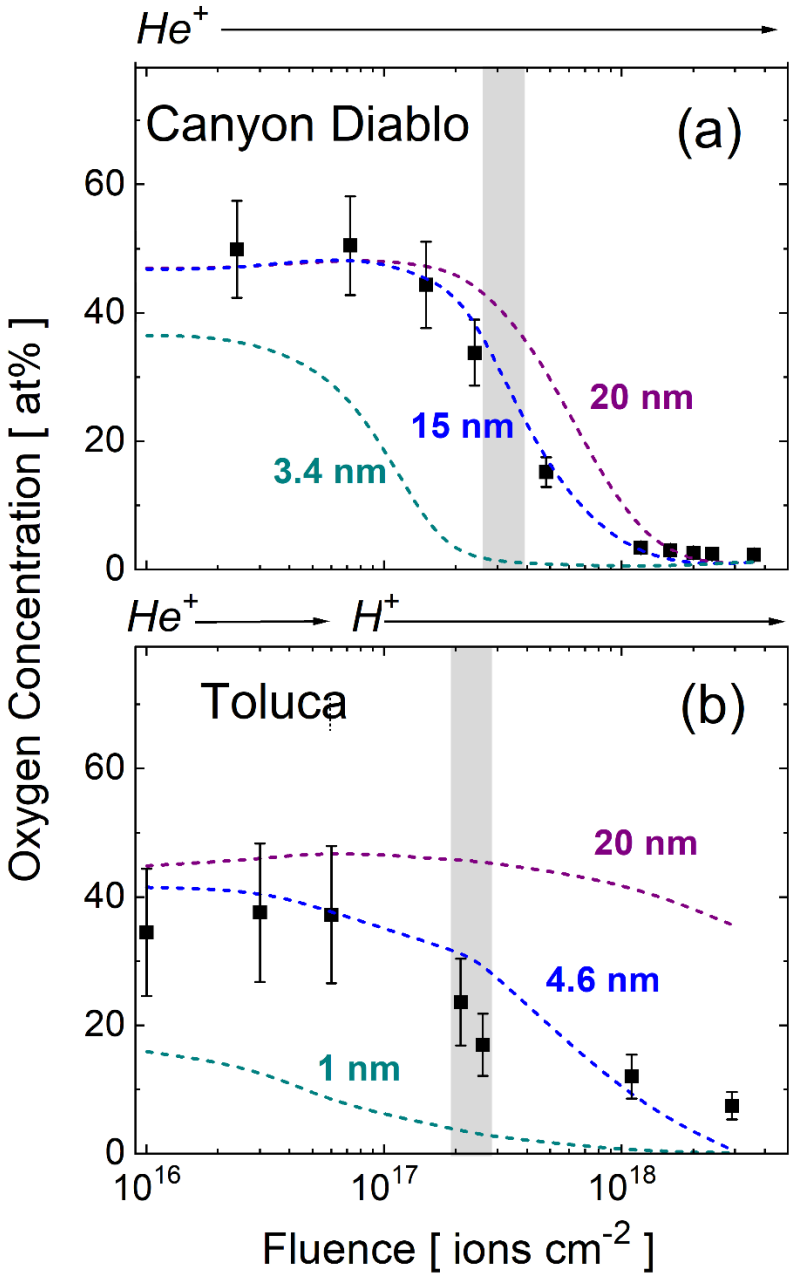

Figure 2.5. SDTrimSP modeling was used to estimate the surface-oxide depth for each meteoritic troilite section by modifying the oxide-layer thickness in the simulation, then comparing computational results to measured composition. XPS data (black squares) are compared to oxide layers of varied thickness (dashed lines) as a function of ion fluence. Based on a chi^2 analysis, oxide layers of ~15 nm and ~4.6 nm in the SDTrimSP

simulation most accurately match XPS-measured O-concentration with fluence on the a) Canyon Diablo and b) Toluca samples. As in Figure 2.3, the gray bar indicates the fluence where the interface between the surface oxide coating and bulk troilite is reached in the experimental results.

2.4. Discussion:

2.4.1. Ion-induced surface roughness and microstructure:

In SEM images, the polished meteorite surfaces showed nanoscale surface roughening which evolved with irradiation (Fig. 2.1). Though these nanofeatures were difficult to resolve individually even at high-magnification, they appear to be uniformly distributed across the irradiated area with minimal variation in scale. AFM analysis indicated that this post-irradiation nanotopography was approximately 5 nm in height and confirmed minimal variation in feature size across the irradiated area. We did not observe a significant difference in feature size or distribution between the Canyon Diablo sample (irradiated only with He^+) and the Toluca sample (irradiated with both He^+ and H^+). With microscopy alone we could not conclude that these features differed in composition from the bulk troilite. However, as noted in the discussion of the Fe and S chemistry derived from XPS, we do observe the formation of surficial Fe^0, and nano-features are known to result from subsurface defects and deformation that occur with the implantation of H/He (Auciello 1984; Scherzer 1983). We do not directly observe any physical structures larger than nanoscale via SEM/AFM, and the roughness we do observe is orders of magnitude smaller than previously observed iron whiskers and nanoparticles in naturally space weathered samples (e.g., Matsumoto et al. 2020, 2021). This is not too surprising, given the importance of diffusion and surface conditions in controlling the mechanism of sulfur depletion as noted by (Matsumoto et al. 2021) and as we further discuss below.

2.4.2. XPS Sulfur Depletion:

Physical sputtering is largely driven by elastic and inelastic collisions that exchange momentum between the projectile ions and atoms/electrons in the material, and is strongly affected by the elemental composition of the surface material, the existence of adsorbed layers, the chemical state (e.g., oxidation state of Fe), and the presence of implanted ions/atoms. Atoms within the solid are sputtered from a target when light keV ions are backscattered from heavier target atoms within the solid, transferring momentum toward the surface in subsequent interactions (Baragiola 2004; Betz and Wehner, 1983). The proportion of momentum transferred is a function of mass, energy and scattering angle. With the onset of irradiation, the near-surface region can become transiently enriched in the lower-mass component of a binary target by momentum-exchange with backscattered light (H, He) ions. With continued irradiation, a steady-state low-mass atom depletion at higher fluence (~10^{17} ions/cm^2) typically results (Betz and Wehner, 1983; Dukes et al. 2011). In dual-component materials such as troilite, the non-stoichiometric (preferential) removal of one species over another is anticipated, until a surface compositional equilibrium is reached. Note that this ion-induced equilibrium is not necessarily equivalent to the material bulk composition (e.g., Taglauer and Heiland 1976).

We observed Fe enrichment within the surface (<10 nm) of irradiated meteoritic troilite (Fig. 2.3), with an average concentration of ~70 at% Fe after ~3×10^{18} ions/cm^2, resulting in an S:Fe ratio of ~ 0.36 and 0.22, for He^+ and H^+ respectively, with normal ion incidence on a polished target. This is roughly twice the S-depletion measured by Loeffler et al. (2008) on 4 keV He^+ irradiated-troilite pressed pellets (S:Fe ~0.60). Increased S-loss from our polished sample was expected, as surface roughness reduces sputtering yields due to topographic shadowing and enhanced sputter redeposition. Models estimate a 25 – 90%

reduction in sputtering yield (Carey and McDonnell 1976; Hapke and Cassidy 1978; Cassidy and Johnson 2005), while experimental tests using granular surfaces suggest a 15 – 67% decrease (Loeffler et al. 2009; Boydens et al. 2013). Strong surface enhancement of Fe in troilite and in pyrite after 1.5 keV Ar^+ and O^+ irradiation has been previously observed by Tsang et al. (1970). Energy-Dispersive X-ray spectroscopy (EDS) analyses have also shown increasing S-loss in synthetic FeS and MgS, inversely-proportional to depth after irradiation by 4 keV He^+ and 5 keV Ga^+, suggesting universal S-depletion in metal sulfides with ions (Keller et al. 2013; Keller and Rahman 2014).

2.4.3. Comparing Proton & Helium Induced Sulfur Depletion:

To identify resultant compositional variation between proton and helium irradiation, the contribution of the surface oxide must be removed. Data normalization is done by shifting the total fluence of sample with the thicker oxide (Canyon Diablo) such that the oxide-substrate interface occurs at the same position; this position becomes the nominal null fluence. We used the oxygen composition of ~50%, to mark this location, which appears in the Canyon Diablo sample at 3.2×10^{17} He^+/cm^2 and at 2.4×10^{17} $(He^+,H^+)/cm^2$ for Toluca; this is well beyond the initial irradiation by He^+ (6×10^{16} He^+/cm^2) in the He^+/H^+ irradiated sample, allowing a direct comparison of proton to helium irradiation effects. Error bars in Fig. 2.6 describe the maximum uncertainty in S/Fe atomic concentration, inclusive of photoelectron transition and sensitivity factor selection. However, the measured relative error for S and Fe within each individual dataset is less than 13.5% (as detailed in the Supplementary Text S3).

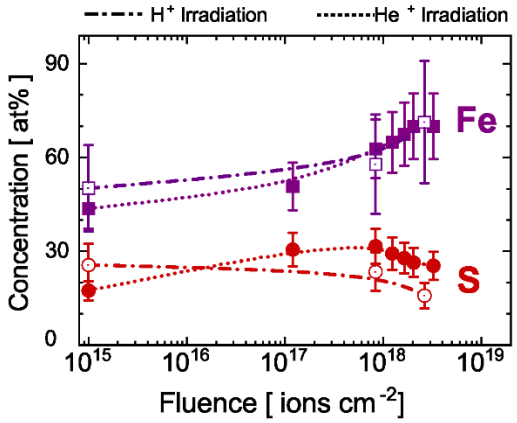

Figure 2.6. Comparison of the troilite surface composition as measured by XPS after removal of the oxide layer, shows similar S and Fe removal rates for 1 keV protons (open points) and 4 keV helium ions (closed points), as described by the change in (a) concentration with fluence and (b) the S:Fe ratio. Data are shifted so that fluence at the oxide-troilite interface (50 at% O) is located at the origin. Interpolated curves between points are meant to guide the eye. Error bars represent the maximum compositional variation due to selection of Fe photoelectron feature (Fe-2p vs. Fe-3p vs. Fe-2p3/2) and experimental error, derived from multiple data acquisitions at adjacent locations. Relative error within each data set is less than <13.5% for Fe and S, confirming near-surface sulfur depletion with respect to iron for both H+ and He+.

We observe that the Fe and S curves trend similarly with fluence (1015 – 1018 ions/cm2) for both He+/H+ irradiations (Fig. 2.6), From the XPS-derived elemental abundance data (Fig. 2.6), comparing the three data points for H+ to the overall trend for He+ suggesting rates of sulfur depletion for each ion species may not be as dissimilar as their measured sputtering yields would suggest (Roth et al. 1979). For a multicomponent material such as troilite, the equilibrium or steady-state sputtering yield generally follows the monoatomic species component with the lowest yield; this is most often the constituent with the greatest mass, as lighter elements are typically preferentially removed (Betz and Wehner 1983, Roth et al. 1980). Therefore, for FeS, one would expect Fe enrichment with extended irradiation, and the sputtering yield would follow the trend of monoatomic Fe,

measured as 10^{-1} atoms/ion for He^+ and 10^{-2} atoms/ion for H^+ (Yamamura and Tawara 1996; Bodhandsky et al. 1977). SDTrimSP calculations for 1 keV/amu He^+ and H^+ on stoichiometric troilite using standard surface binding energies identify similar order-of-magnitude differences, calculating Y_{He+}/Y_{H+} ratios of ~8 (0.08/0.01) and ~11 (0.045/0.004) for sulfur and iron, respectively at low fluence (Fig. S7).

These values imply that the Fe-enrichment should occur roughly a decade faster for He^+ irradiated troilite. However, this is not the case, as the final S:Fe ratio is 0.32 for the He^+ irradiation (Canyon Diablo) and 0.22 for the H^+ irradiation (Toluca) after ~3 x 10^{18} ions cm^{-2}. While only a minimal number of measurements with protons were acquired (due to the oxide overlayer), the similarity between He^+/H^+ curves over a wide range of fluences is intriguing and merits further investigation.

We found no evidence of new chemical species formation in the high-resolution XPS data (e.g. Fig. 2.4) to a level ~100 ppm, suggesting that chemical sputtering enhancement of yield is unlikely, nor indication of beam contamination with heavier ions. Identification of a thermal dependence could provide more definitive information, as reactivity is a strong function of temperature (Roth 1983). Irradiation by diatomic molecular ions such as H_2^+ have been shown to increase the sputtering from surfaces at high energies (> 10 keV) due to overlapping of collision cascades; similarly, at energies < 1 keV the sputtering yield deviates from twice the monatomic yield due to variation in the molecule effective mass (Yao et al 1998; Dobes et al. 2011). However, low-energy ion scattering measurements for 2 keV H_2^+ and microbalance analysis for 2, 4 keV O_2^+ have shown that for singly-ionized diatomic molecules, the kinetic energy is divided quite equally between atoms (Dukes et al. 1999; Szabo et al. 2020b). Since irradiations in

the current project fall in the low keV range, between 0.5 and 10 keV, we do not expect molecular ions to enhance the sputtering rate. Lastly, radiation-enhanced diffusion, the increase in target-atom self-diffusion precipitated by the growth of irradiation-induced defects in the solid, can increase the mobility of S-atoms to the surface to be sputter-removed. This mechanism will investigate H^+ and He^+ irradiation in detail in Section 2.4.4.2.

2.4.4. Investigating Sulfur Depletion with SDTrimSP:

The preferential removal of S over Fe with irradiation results from either (1) surface composition changes due to differences in constituent masses or surface binding energy (U_s), or (2) compositional changes in the altered layer through the ion penetration depth, or (3) both. Elemental concentrations through the ion range derive from thermal diffusion, radiation-enhanced diffusion, recoil implantation and mixing, species surface segregation and radiation-enhanced segregation (Betz and Wehner, 1983). Diffusion mechanisms assist in depletion by transporting the more volatile species (e.g. S) in vacancies and interstitials through a concentration gradient toward the surface, where it is subsequently sputter removed. Segregation traps the S at the solid-vacuum interface where free energy is minimized. Both diffusion and segregation mechanisms are a function of temperature, and thus may perform differently on the surface of Psyche and other objects within the Asteroid Belt, where temperatures can reach from ~240 K (e.g. Tosi et al. 2018) to significantly below. To identify the most-influential parameters driving ion-induced sulfur depletion in troilite, we simulated the process using SDTrimSP.

2.4.4.1. Effect of Surface Binding Energy:

We evaluated the effect of surface binding energy (U_s) on the FeS composition with ion irradiation by modifying the atom-specific parameters in SDTrimSP. For the knock-on collision regime of keV protons and helium interactions, the sputtering yields for troilite are highly-dependent on internal kinetics governed by the target mass distribution, and to a lesser extent, by the atom surface binding energy. We confirmed this by independently varying U_s for sulfur, while monitoring the effect on the target composition with irradiation and holding all other variables constant. We found that even large changes in U_s (0 vs. 10 eV) for sulfur relative to iron did not affect the depletion profile significantly using either independent values for U_s (model 1) or composition weighted values (model 2) (see Fig. S6). Thus, we conclude that U_s had a minor effect on the preferential sputtering of S, insufficient to explain the magnitude of the observed S:Fe depletion. Therefore, sulfur segregation or diffusion effects within the ion-altered region must account for discrepancies between the simulation and XPS data. In subsequent SDTrimSP simulations, we retained U_s default values, equivalent to the heat of sublimation.

2.4.4.2. Effect of Ion-induced Diffusion of Sulfur:

SDTrimSP has recently been updated to include diffusion within the target, including: (1) solid-state thermal diffusion, where given sufficient thermal energy, target atoms move through the solid-state lattice filling vacancies or occupying interstitial regions; and (2) radiation-enhanced diffusion, in which the mobility of target atoms is enhanced by the greater ion-induced defect density. In addition, simulations may also include (3) diffusion of the implanted projectile via pressure-driven transport and by (4) outgassing of the projectile due to sputter-induced compositional gradients. At 300K target atoms are mobilized exclusively by concentration gradients within the damage-region,

diffusing toward the surface at rates dependent on concentration and on the temperature-dependent diffusion coefficient with a probability dependent on location within the ion range (nearby atomic displacement). SDTrimSP employs variations of Fick's laws to describe the diffusion of target atoms toward the surface, as detailed in the Supplementary Data section and in von Toussaint et al. (2016).

We evaluated the effect of S-diffusion by comparing the simulated target composition with fluence to XPS laboratory data, enabling and disabling diffusion in SDTrimSP. The compositional fit to data was vastly improved when damage-driven diffusion was included in the model (Fig. 2.7), suggesting that radiation-induced diffusion plays a critical to establishing S:Fe equilibrium values. We were able to estimate the sulfur diffusion coefficient η_T by running multiple SDTrimSP simulations with different settings and obtaining a best fit against our experimental data. SDTrimSP does not provide default diffusion coefficients except for H, Ar, and Xe. Since the ratio of diffusivity between helium and hydrogen was found to be 0.897 through gypsum (Yang et al. 2013) and 1.012 through air (Cussler et al. 1985), both close to unity, we equated the He and H diffusion coefficients. For target atoms, no published values appear in the literature for sulfur diffusion through troilite, thus, we extracted these values from SDTrimSP-XPS data best fits. Radioactive tracer measurements of diffusion through metals show that the diffusivity for S can be orders of magnitude larger than that of Fe (Haynes et al. 2016), thus Fe remained static in our models.

Using order of magnitude estimations, the values for the damage-driven sulfur diffusion coefficients that have the lowest chi^2 when compared to the Canyon Diablo and Toluca XPS data were respectively: $\sim 1 \times 10^3$ and $\sim 5 \times 10^2$ $Å^4$ per atom, roughly 10^{-3} of

the helium/hydrogen coefficients thus, we determined $\eta_T(S)$ = 7.5 × 10^2 Å^4 per atom (Fig. 2.7).

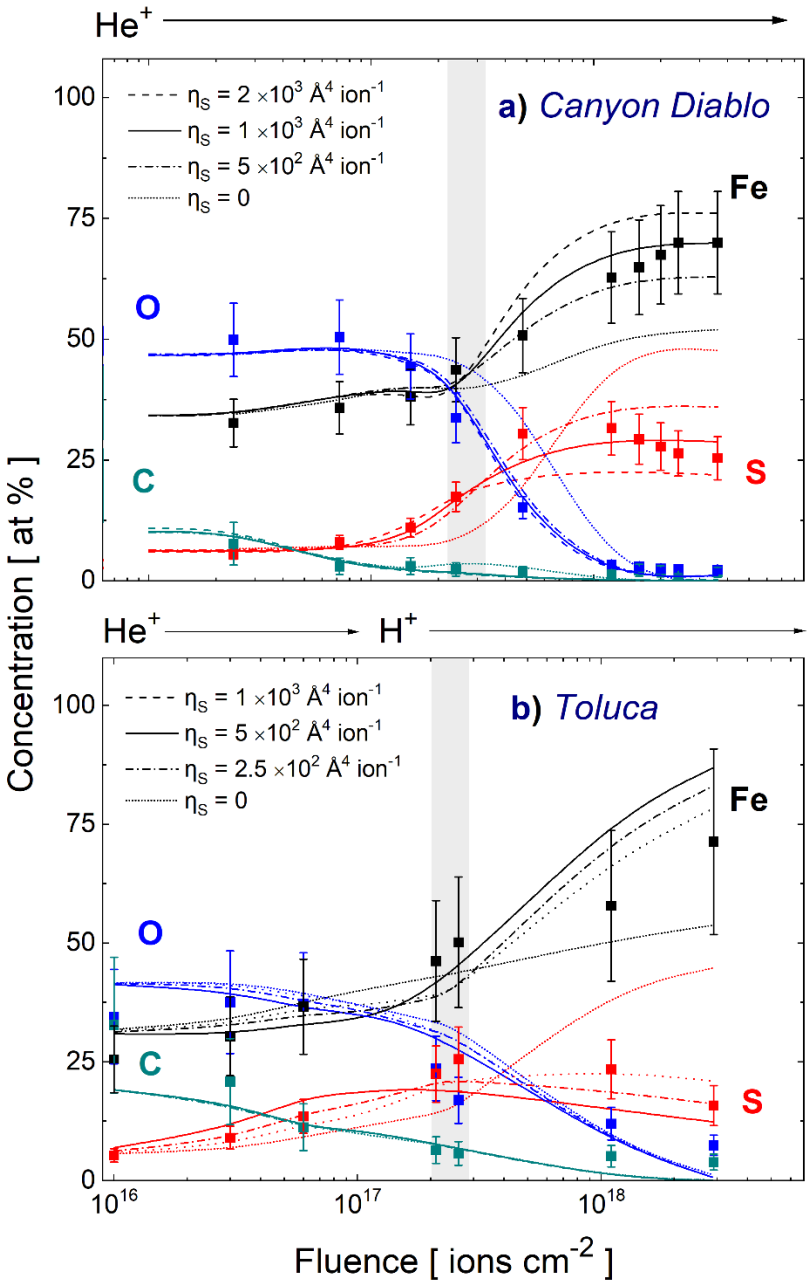

Figure 2.7. Inclusion of damage-driven diffusion for sulfur in the SDTrimSP simulation has a strong effect on modeled surface compositional changes in meteoritic troilite with ion irradiation. With no sulfur diffusion ($\eta_S = 0$) in the model (a & b: dotted curves), the simulations do not replicate the measured surface composition (squares) for fluences beyond 5 x 10^{-17} ions cm^{-2}. (a) Adjustment of the sulfur diffusion coefficient (dashed & solid curves) improves the model, where a chi^2 best fit to S, Fe, O, and C compositions was identified for $\eta_S = 1 \times 10^3$ Å^4 per He^+ (solid curve). (b) Similarly, inclusion of damage-driven diffusion and variation of the coefficient for sulfur (dashed & solid curves) in the Toluca troilite identified a best fit with $\eta_S = 5 \times 10^2$ Å^4 per H^+ (dash-dot curve). Implanted H and He were also allowed to diffuse in the simulations. As in Figures 2.3 and 2.5, the gray bar indicates the fluence where the interface between the surface oxide coating and bulk troilite is reached in the experimental results.

To quantify the sulfur diffusion in standard units (cm^2/s), we compared the concentration of sulfur at a depth of 150Å in the Canyon Diablo target after two different He^+ fluences: (1.2×10^{18} He^+/cm^2 and 3.6×10^{18} He^+/cm^2), resulting in an estimated sulfur flux through the sample of 7.6×10^7 atoms/cm^2/s (see Supplementary Text S5). Thus, we find the sulfur-diffusion coefficient $D_T(S)$ through the damage region of irradiated amorphous FeS is approximately 5.6×10^{-22} cm^2/s at 300K. This is significantly larger than diffusion measurements for isotopically-labelled ^{34}S through natural crystalline pyrite as measured by Rutherford backscattering for temperatures 500 – 725°C; extrapolating the coefficient to 300 K yields $D_S = 1.75 \times 10^{-37}$ cm^2/s (Watson et al. 2009), although such an extrapolation below the explicitly defined temperature range introduces substantial uncertainty. There is not a large body of literature comparing diffusion rates for amorphous vs. crystal structures (Lazarus 1985). Coffa et al. (1992) found the diffusivity for transition-metal species through silicon was larger for amorphous phases and suggested that transitory trapping at defects may inhibit interstitial diffusion in amorphous structures. While troilite demonstrates continued crystalline phases with irradiation (Christoffersen and Keller 2011), defects and damage may similarly inhibit diffusion, resulting in a larger sulfur-diffusion coefficient.

2.4.5. Effect of Elemental Composition within the Altered Layer:

With the inclusion of diffusion processes for sulfur and helium (or hydrogen), the altered layer directly below the surface through the ion range was inspected in the SDTrimSP simulations (Fig. 2.8). The simulation results were compared with our XPS measurements, as well as Keller et al. (2013) interpretations for 4 keV He^+ (45° incidence; 2.3×10^{18} He^+/cm^2) irradiated FeS and Matsumoto et al. (2020) observations of naturally space weathered Itokawa FeS grains. In transmission electron microscopy (TEM) cross-sections, Keller et al. (2013) identified a Fe-enriched surface region of 2-3 nm with S-depletion throughout the outermost ~10 nm of the irradiated troilite, which was interpreted as the formation of a metallic skin atop a strongly S-depleted region roughly equivalent to the ion range. Similar results were found in natural Itokawa FeS grains exposed to the solar-wind, along with vesicles throughout the damaged region to a depth of 40-50 nm (Matsumoto et al. 2020, Chaves et al. 2021). The vesicles, which in some cases are open to the surface, are expected to result from the aggregation of implanted solar gases, since they appear through the ion penetration region. Partially amorphized sulfur-depleted rims were also found on lunar FeS grains (Matsumoto et al. 2021), although these were significantly thicker (~80-100), suggesting a contribution from other space weathering mechanisms such as meteorite-impact vapor deposition or more-energetic ions.

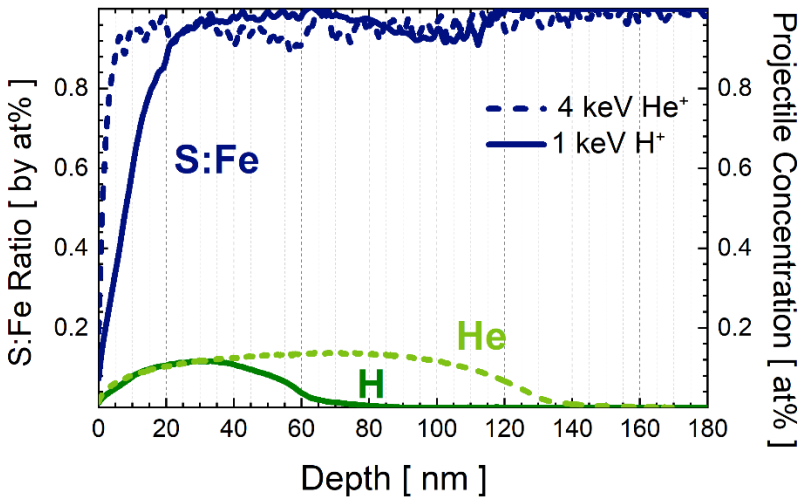

Figure 2.8. SDTrimSP model for the final composition of troilite after 3.6 × 10^{18} (H, He)/cm^2 as a function of depth, including implanted projectile species, with flux of 1 × 10^{13} (H, He)/s/cm^2. The ratio of S:Fe illustrates the significant S-depletion in the near-surface with helium irradiation (~5 nm; dashed blue) and with proton irradiation (~20 nm), with minor depletion (5 - 10%) extending even beyond the projectile penetration range due to diffusion resulting from the compositional gradient within the solid. The projectile implantation depth extends to ~60 nm for 1keV H^+ (solid green) and ~130 nm for 4 keV He^+ (dashed green).

Both Matsumoto et al. (2020) and Keller et al. (2013) results are consistent with our XPS measurements of S:Fe concentration, where 95% of the S-2p and Fe-3p peak intensity derive from the surface-most ~8 nm, based on the calculated IMFP (Powell and Jablonski 2010). These results are also consistent with SDTrimSP results for 4 keV He^+ irradiation to the fluence used in our experiments on meteoritic troilite (3.6 × 10^{18} He/cm^2), where a strong Fe-enrichment (S:Fe ~0.1) is seen at the surface, decreasing swiftly with depth such that S:Fe ~0.7 at 5 nm and 95% bulk stoichiometry is reached at ~10 nm (Fig. 2.8). The implanted He appears to be mainly distributed through depths of 10 – 110 nm – directly below the significant S-depletion region and diffusing well beyond the classical

penetration depth of 48 nm (range + straggle) calculated via TRIM (Ziegler et al. 1985). The ability for projectile ions to appear well beyond the ion range has been noted by many researchers and has been ascribed to ion-enhanced diffusion, lattice swelling, discrete breathers and other mechanisms (deBroglie et al. 2015; von Toussaint et al. 2016; Zhang et al. 2010). The helium concentration decrease with proximity to the surface is due to the low U_s, which results in preferential sputtering at the outermost monolayer; this creates a concentration gradient for helium – from bulk to surface through the damage region – driving diffusion outward. Pressure-driven outgassing of the unbound projectiles additionally increases their transport from the implantation position.

For 1 keV protons the damage layer thickness differs due to the decreased penetration depth, although the absolute near-surface Fe-enrichment is enhanced, similar to our experimental data. We suggest that, for identical fluence, the decreased S:Fe for protons is due to an increase in the density of recoil displacements localized in the near-surface region (< 10 nm) facilitating S-diffusion with subsequent sputter removal.

Similar to helium, SDTrimSP describes the presence of hydrogen, enhanced in the 10 – 30 nm range after irradiation by 3.6×10^{18} H^+/cm^2. This correlates with the embedded deep-vesicle region (40 -50 nm) identified in the Itokawa troilite particles (Matsumoto et al. 2020). This trapped hydrogen is then available for the formation of new molecular species, e.g. H_2O and H_2S, in the irradiated grain rim region (Schaible et al. 2014, Zhu et al. 2019).

2.4.6 Solar-ion weathering of 16 Psyche:

Having benchmarked our model parameters with XPS laboratory data, we are able to predict the effect of solar wind irradiation on *pure* troilite at Psyche. A simultaneous

mixture of 4 keV He^+ (4%) and 1 keV H^+ (96%) at a total ion flux (2.9 A.U.) of 2.4×10^7 ions cm^{-2} s^{-1} were used in the simulation. Since S-diffusion plays the major role in the depletion process, the contribution of heavy ions (Ar^+; O^+, etc.) was not included in this simulation. However, appropriate flux is critical, as concentration gradients are driven by the counterpoint between sputtering rate and subsurface radiation-induced diffusion (von Toussant et al. 2016), changing significantly over the course of the irradiation as a function of surface atomic concentration (Fig. S7). Initially, S sputters more rapidly (0.08 S/He; 0.01 S/H) from troilite than Fe (0.05 Fe/He; 0.005 Fe/H), preferentially removing sulfur from the near surface, such that by the time steady-state conditions – beyond 3×10^{18} ions cm^2 – are reached, SDTrimSP sputtering yields are dominated by Fe (protons: S: 0.004; Fe: 0.009; H: 0.004 atoms/H^+ and helium: S: 0.03; Fe: 0.08; He: 0.02 atoms/He^+) at Psyche solar-wind fluxes.

Our results suggest a rapid depletion of surficial sulfur on Psyche's surface over the first 100 years (Fig. 2.9), consistent with sulfur depletion observed on other airless asteroid surfaces, such as Eros (Nittler et al. 2001) and Itokawa (Arai et al. 2008), where S-depletion appears to correlate with space-weathered regions. From the simulation, we expect that the S:Fe ratio in surficial fresh-regolith troilite on Psyche should decay from unity to a level of ~7% as a function of time. The depletion curve is best fit with a logistic model: $y = A_2 + [(A_1 - A_2) / (1 + (t / t_0)^{\rho})]$, where A_1 is the initial S:Fe ratio (1), A_2 is the equilibrium ratio after extended irradiation (0.067), t_0 is the midpoint of change (1.21 years), and ρ is the fitting power (0.70). This type of fit is frequently used as an empirical model for sputter depth profiling to describe concentration changes at the interface between two dissimilar layers, such as FeS and the resultant S-depleted Fe (e.g. Kirchhoff 2012).

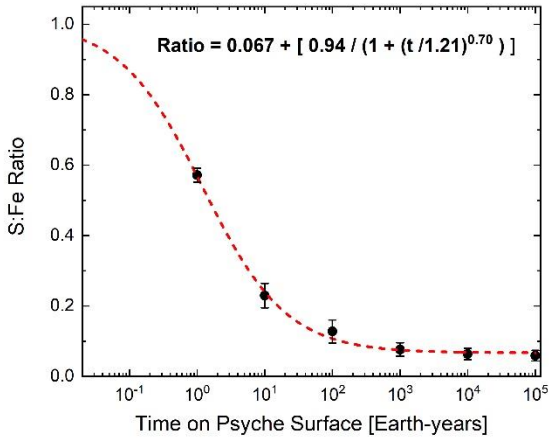

Figure 2.9. Sulfur depletion was quantified via SDTrimSP in the outermost monolayer (1 ML) for exposed troilite deposits within Psyche's surface regolith over time (Earth-years), given a solar wind flux of 2.4 × 10^7 ions cm^{-2} s^{-1} for a combination of 1 keV/amu protons (96%) plus helium (4%) is calculated via SDTrimSP. The S:Fe ratio decays at a geophysically-rapid rate from unity to a level of ~7% within 10 kyr, fit with a logistic curve. The ability to observe this depletion with the Psyche Mission's GRNS Spectrometer will depend on multiple parameters, including the asteroid surface composition, troilite abundance, average grain size, and the regolith gardening rate.

Psyche's uppermost monolayer is expected to record the greatest extent of sulfur-depletion from solar-wind ion irradiation – of high-significance for exospheric production; thus, we focus our SDTrimSP studies on depletion in this region. Secondary-ion mass spectrometers directed toward the surface of an airless body are able to identify species sputtered from the surface monolayer of an airless body such as the Moon (e.g. Johnson 1991; Elphic 1992; Yokota et al. 2009) or Mercury (e.g. Zurbuchen et al. 2008; Raines et al. 2013). However, while Schläppi et al. (2008) identify solar-wind ion sputtering as the dominant mechanism for exospheric production at asteroids 2867 Steins and 21 Lutetia and transient OH and H2O has been noted at Ceres, no exosphere has been definitively detected yet around an asteroid (Grava et al. 2021). Thus, the potential to identify a thin

sulfur-exosphere sputtered from the surface of Psyche is intriguing, with further study merited.

In addition, while ion irradiation directly depletes surficial (10 nm) sulfur in laboratory samples, regolith gardening processes at Psyche should cycle irradiated surface particles, thus propagating the sulfur-depleted region to greater depth. Though gardening rates and depths have yet to be quantified on a metallic surface, studies of S-complex asteroid surfaces suggest time scales ranging from 10^4 years (Loeffler et al. 2008) to 10^5 years (Willman et al. 2010) and depths from 1 cm (Loeffler et al. 2008) to 1 km (Housen et al. 1979).

Two instruments aboard the Psyche spacecraft will measure surface properties potentially relevant to space weathering. The Gamma Ray & Neutron Spectrometer (GRNS) will measure bulk elemental abundances in the upper 10-100 cm across large-footprint (~10s of km diameter) regions of Psyche's surface beginning in Orbit D, with the ability to detect sulfur with 15% measurement precision if it is present at >3 wt.% abundance (Peplowski et al. 2018). The Multispectral Imager will infer surface mineralogy using eight filter bands in the visible to near-infrared (~400 to ~1100 nm) built into twin CCD cameras (Dibb and Bell 2018). Changes in surface micro-roughness and chemistry may both play a role in altering the optical reflectance, slope, and albedo of troilite and other minerals present on the surface of Psyche (Yon and Pieters 1987). The size and relative abundance of troilite grains in the regolith, as well as gardening rates and other concurrent sulfur-depleting processes (e.g. Prince et al. 2020), will influence the detectability of weathering-induced sulfur depletion by both instruments, while not being directly measured.

Once the GRNS measures the sulfur content of a region and mineralogy is derived from multispectral images, a suite of compositions with different mixtures of rock, metal, and sulfide will non-uniquely match these measurements. In a compositional mixing model, the troilite fraction may be assumed to have reached full depletion of its sulfur content, or the degree of weathering may be included as a free parameter. Compositional models must also account for sputtered sulfur, which if it does not escape into space (Schläppi et al. 2008), redeposits across a wide area of the asteroid surface. Finally, the presence, strength, and structure of a magnetic field at Psyche would affect the flux of solar wind at the asteroid surface (Elkins-Tanton et al. 2020, Oran et al. 2018).

2.5. Conclusion:

We experimentally simulated space weathering by solar-wind ions on meteoritic troilite samples, irradiating with both 1 keV H^+ and 4 keV He^+. Irradiation resulted in an ion-induced increase in sample surface roughness to ~5 nm uniformly distributed across the irradiated area, with H^+ and He^+ ions appearing equally effective at roughening polished surfaces. We observed loss of sulfur due to ion-induced sputtering, with H^+ irradiation surprisingly similarly effective at removing sulfur relative to iron as He^+. Sputtering yields for troilite are fluence-dependent, with near-surface sulfur preferentially sputter-removed at low fluences leaving a Fe-enriched surface.

Minimal chemical variation is observed in S, while Fe is reduced from air-formed oxide and native troilite at high fluences to Fe^0. We modelled these irradiations with SDTrimSP, concluding that surface binding energy has only a minor effect on the distribution of S within the solid; rather, sulfur diffusion effects in the ion-altered region account for the magnitude of the observed S:Fe depletion. Without invoking gardening or

other processes, detecting S-depleted troilite with the Psyche spacecraft's instruments may be challenging. These findings should be generally applicable to any troilite-containing airless planetary body.

Acknowledgements:

This work is supported by NASA contract NNM16AA09, "Psyche: Journey to a Metal World." We acknowledge the use of facilities within the Eyring Materials Center at Arizona State University supported in part by NNCI-ECCS-1542160. J.M.C thanks the staff and researchers at the Center for Meteorite Studies and the Eyring Materials Center at Arizona State University. C.A.D. acknowledges support from the NASA SSW Working Program (NNX15AM38G) and NSF Astronomy (2009365). The NSF MRI Program (1626201) is acknowledged for UVa's PHI Versaprobe III XPS. G.M.M. was supported by the Virginia Initiative for Cosmic Origins (VICO) and the Psyche Mission. We are grateful to M. Thompson, L. Chaves, and one anonymous reviewer for their recommendations, which improved this paper significantly. Thanks also to D. Rogers, S. Dibb, A. Gerhard, and others for editorial assistance. Data for this research are available at: Christoph (2021).

References

Arai, T., Okada, T., Yamamoto, Y. et al. (2008) Sulfur abundance of asteroid 25143 Itokawa observed by X-ray fluorescence spectrometer onboard Hayabusa, *Earth Planet Space* 60, 21–31.

Arredondo, R., Oberkofler, M., Schwarz-Selinger, T., von Toussaint, U., et al. (2019) Angle-dependent sputter yield measurements of keV D ions on W and Fe and comparison with SDTrimSP and SDTrimSP-3D *Nuclear Materials and Energy* 18, 72–76.

Auciello, O. (1984) Historical Overview of ion-induced morphological modification of surfaces, In *Beam Modification of Materials*; Elsevier, Amsterdam.

Bagus, P.S, Nelin, C.J., Brundle, C.R., Crist, B.V., Lahiri, N., and Rosso, K.M., (2021) Combined multiplet theory and experiment for the Fe 2p and 3p XPS of FeO and Fe_2O_3, *The Journal of Chemical Physics* 154, 094709.

Baragiola, R.A., (2004) Sputtering: survey of observations and derived principles. *Philosophical Transactions of the Royal Society of London A: Mathematical, Physical and Engineering Sciences* 362, 29-53.

Barr, T. L. and Seal, S. (1995) Nature of the use of adventitious carbon as a binding energy standard, *Journal of Vacuum Science & Technology* 13, 1239-1246.

Betz, G. and Wehner, G.K., 1983. Sputtering of multicomponent materials. In *Sputtering by Particle Bombardment II* (pp. 11-90). Heidelberg: Springer.

Bezaeva, N. S., Gattacceca, J., Rochette, P., Duprat, J., Rizza, G., Vernazza, P., Trukhin, V. I., and Skripnik, A. (2015) The effect of irradiation on the magnetic properties of rock and synthetic samples: Implications to irradiation of extraterrestrial minerals in space, *Physics of the Solid Earth* 51 336-353.

Biesinger, M. C., Payne, B. P., Grosvener, A. P., Laua, L. W. M., Gerson, A. R., and Smart, R. St. C. (2011) Resolving surface chemical states in XPS analysis of first row transition metals, oxides and hydroxides: Cr, Mn, Fe, Co and Ni, *Applied Surface Science* 257 2717-2730.

Brion, D. (1980) Etude par spectroscopie de photoelectrons de la degradation superficielle de FeS2, CuFeS2, ZnS et PbS a l'air et dans l'eau, *Applications of Surface Science* (in French) 5, 133-152.

Bohdansky, J., Bay, H. L., and Roth, J. (1977) In: Proceedings of the 7th International Vacuum Congress and 3rd Interactional conference of Solid Surfaces, ed. by R. Dobrozemsky, F. Rudenauer, F.P. Viehbock, A. B. Reth, Private publisher: Vienna.

Boydens, F., Leroy, W.P., Persoons, R., and Depla, D. (2013) The influence of target surface morphology on the deposition flux during direct-current magnetron sputtering, *Thin Solid Films*, 531, 32-41.

Cassidy, T. A., and Johnson, R. E. (2005) Monte Carlo model of sputtering and other ejection processes within a regolith, *Icarus* 176, 499

Carey, W. C. & McDonnell, J. A. M. (1976) Lunar surface sputter erosion - A Monte Carlo approach to microcrater erosion and sputter redeposition in Lunar Science Conference, 7th, Houston, Tex., March 15-19, 1976, Proceedings. Volume 1. (A77-34651 15-91) Pergamon Press, Inc: New York.

Chapman, C.R. (1996) S-type asteroids, ordinary chondrites, and space weathering: the evidence from Galileo's Fly-bys of Gaspra and Ida. (Invited review). *Meteoritics & Planetary Science* 31, 699-726.

Chapman, C.R. (2004) Space weathering of asteroid surfaces, *Annual Review of Earth and Planetary Sciences* 32, 539-567

Chaves, L.C., et al. (2021) Space Weathering Features in a Sulfide Grain from Asteroid Itokawa. Presented at *Lunar and Planetary Science Conference LII* Abstract #1770

Christoffersen, R. and Keller, L.P. (2011), Space radiation processing of sulfides and silicates in primitive solar systems materials: Comparative insights from in situ TEM ion irradiation experiments. *Meteoritics & Planetary Science* 46, 950-969. https://doi.org/10.1111/j.1945-5100.2011.01203.x

Christoph, J. M. (2021, April 2). Interpretation of solar wind ion irradiation experimental and model simulations. Retrieved from https://osf.io/st79b/?view_only=690588e64f5c4fe8bf19a6b1e77ae303 (peer review link)

Clark B.E., Fanale, P., and Salisbury, J.W. (1992) Meteorite-asteroid spectral comparison: The effects of comminution, melting, and recrystallization, *Icarus* 97, 288-297

Coffa, S., Poate, J. M., and Jacobson, D. C. (1992) Determination of diffusion mechanisms in amorphous silicon, *PHYSICAL REVIEW B* 45

DeBroglie, I., Beck, C., Liu, W. & Hofmann, F. (2015) Temperature Dependence of Helium--Implantation--Induced Lattice Swelling in Polycrystalline Tungsten: X--ray Micro--Diffraction and Eigenstrain Modelling, *Scripta Materialia* 107, 4

Descostes, M., Mercier, F., Thromat, N., Beaucaire, C. and Gautier-Soyer, M. (2000) Use of XPS in the determination of chemical environment and oxidation state of iron and sulfur samples: constitution of a data basis in binding energies for Fe and S reference compounds and applications to the evidence of surface species of an oxidized pyrite in a carbonate medium, *Applied Surface Science* 165, 288-302

Dibb, S.D. and Bell, J.F. (2018) Optimization of Narrowband Visible to Near-IR Filters for the Psyche Multispectral Imager. Presented at *Lunar and Planetary Science Conference XLIX* Abstract #2083

Dobes, K., Naderer, P., Lachaud, N., Eisenmenger-Sittner, C., & Aumayr, F. (2011). Sputtering of tungsten by N+ and N2+ ions: Investigations
of molecular effects. *Physica Scripta*, T145, 014017. https://doi.org/10.1088/0031-8949/2011/T145/014017

Dukes, C. A., Baragiola, R. A., and McFadden, L. A. (1999) Surface modification of olivine by H^+ and He^+ bombardment, *Journal of Geophysical Research: Planets* 104, 1865-1872

Dukes, C. A., Chang, W., Famá, M., and Baragiola, R. A. (2011) Laboratory studies on the sputtering contribution to the sodium atmospheres of Mercury and the Moon, *Icarus* 212, 463-469

Elkins-Tanton, L.T., Bell, J.F, Bercovici, H., Bills, B., Binzel, R., Bottke, W.F., Dibb, S., Lawrence, D.J., Marchi,S., McCoy, T.J., Oran, R., Park, R.S., Peplowski, P.N., Polanskey, C.A., Prettyman, T.H., Russell, C.T., Schaefer, L., Weiss, B.P., Wieczorek, M.A., Williams, D.A., and Zuber, M.T. (2020) Observations, meteorites, and models: a pre-flight assessment of the composition and formation of (16) Psyche, *Journal of Geophysical Research, Planets* 125

Farrell, W.M., Hurley, D.M., and Zimmerman, M.I. (2015) Solar wind implantation into lunar regolith: Hydrogen retention in a surface with defects, *Icarus* 255, 116-126

Fick, A. (1855). Ueber Diffusion, *Annalen der Physik* (in German) 94, 59–86

Fink, D., Meirav, O., Paul, M., Ernst, H., Henning, W., Kutschera, W., Kaim, R., Kaufman, A., and Magaritz, M. (1984) Experiments on the sputtering if group VI elements, *Nuclear Instruments and Methods in Physics Research Section B: Beam Interactions with Materials and Atoms* 1, 275-281

Gaffey, M., Bell, J.F., Brown, R., Burbine, T., Piatek, J., Reed, K., and Chaky, D. (1993) Mineralogical variations within the s-type asteroid class, *Icarus* 106, 573-602

Gold, T. (1955) The lunar surface, *Royal Astronomical Society* 115, 585-604

Goretzki H., Rosenstiel P.V., Mandziej S., and Fres. Z. (1989) *Analytical Chemistry* 333, 451

Grady, M.M., Pratesi, G., and Cecchi, V.M. (2014) *Atlas of Meteorites*, Cambridge University Press

Grava, C., Killen, R.M., Benna, M., et al. (2021) Volatiles and Refractories in Surface-Bounded Exospheres in the Inner Solar System. *Space Science Reviews*, 217, 61, https://doi.org/10.1007/s11214-021-00833-8

Haynes, W. M., Lide, D. R., & Bruno, T. J. (2016) *CRC handbook of chemistry and physics: a ready-reference book of chemical and physical data*. 97th ed. CRC Press: Boca Raton, Florida:.

Hapke (2001) Space weathering from Mercury to the asteroid belt, *Journal of Geophysical Research* 106, 10,039-10,073

Hapke, B., & Cassidy, W. (1978) Is the Moon really as smooth as a billiard ball? Remarks concerning recent models of sputter-fractionation on the lunar surface, *Geophysical Research Letters* 5, 297

Harries and Langenhorst (2014) The mineralogy and space weathering of a regolith grain from 25143 Itokawa and the possibility of annealed solar wind damage, *Earth, Planets, and Space* 66, 1-11

Hofsäss, Zhang, and Mutzke (2014) *Applied Surface Science* 310, 134-141.

Housen, K.R., Wilkening, L.L., Chapman, C.R., and Greenberg, R. (1979) Asteroidal regoliths, *Icarus* 39, 317-351

Idczak, K., Idczak, R., and Konieczny, R. (2016) An investigation of the corrosion of polycrystalline iron by XPS, TMS and CEMS, *Physica B: Condensed Matter* 491, 37-45

Kajita, S., Ishida, T., Ohno, N., Hwangbo, D., and Yoshida, T. (2016) Fuzzy nanostructure growth on Ta/Fe by He plasma irradiation, *Scientific Reports* 6, 1-10

Keller, L. P., Loeffler, M. J., Christoffersen, R., Dukes, C., Rahman, Z., and Baragiola, R. (2010) Irradiation of FeS: Implications for the lifecycle of sulfur in the interstellar medium and presolar FeS grains, *Lunar and Planetary Science Conference XLI*

Keller, L. P. and McKay, D.S. (1997) The nature and origin of rims on lunar soil grains, *Geochimica et Cosmochimica Act* 61, 2331-2341

Keller, L. P. and Rahman, Z. (2014) Relative sputtering rates of FeS, MgS, and Mg Silicates: Implications for ISM Gas Phase Depletions of Rock-Forming Elements, *NASA NTRS*

Keller, L. P., Rahman, Z., Hiroi, T., Sasaki, S., Noble, S. K., Hörz, F., and Cintala, M. J. (2013) Asteroidal space weathering: the major role of FeS. Presented at *Lunar and Planetary Science Conference XLIV* Abstract #2404

Killen, R. M. (2003) Depletion of sulfur on the surface of asteroids and the moon, *Meteoritics & Planetary Science* 38, 383-388

Kirchhoff, W.H. (2012) Logistic Function Profile Fit: A least-squares program for fitting interface profiles to an extended logistic function, *Journal of Vacuum Science & Technology A* 30, 5

Kracher, A. and Sears, D.W.G. (2005) Space weathering and the low sulfur abundance of Eros, *Icarus* 174, 36-45

Landsman, Z.A., Campins, H., Pinilla-Alonzo, N., Hanus, J., and Lorenzi, V. (2015) A new investigation of hydration in the M-type asteroids, *Icarus* 252, 186-198

Laczniak, D. L., Thompson, M. S., Christofferson, R., Dukes, C.A., Clemett, S.J., Morris, R.V., and Keller, L.P. (2021) Characterizing the spectral, microstructural, and chemical effects of solar wind irradiation on the Murchison carbonaceous chondrite through coordinated analysis. *Icarus* 364, https://doi.org/10.1016/j.icarus.2021.114479

Lazarus, D. (1985) Diffusion in Crystalline and Amorphous Solids, Presented at *Symposium I – Phase Transitions in Condensed Systems--Experiments and Theory* 57, 297

Lennie, A. and Vaughan, D. J., ed. Dyar, M. D., McCammon, C., and Schaefer, M. W. (1996) Spectroscopic studies of iron sulfide formation and phase relations at low temperatures, *The Geochemical Society, Special Publication No.5*

Loeffler, M. J., Dukes, C. A., Chang, W. Y., McFadden, L. A., and Baragiola, R. A. (2008) Laboratory simulations of sulfur depletion at Eros, *Icarus* 299, 240-252

Loeffler, M.J., Dukes, C.A., and Baragiola, R.A. (2009) Irradiation of olivine by 4keV He^+: Simulation of space weathering by the solar wind, *Journal of Geophysical Research Planets* v. 114 https://doi.org/10.1029/2008JE003249

Loeffler, M.J., Dukes, C.A., Christoffersen, R., and Baragiola, R.A. (2016) Space weathering of silicates simulated by successive laser irradiation: In situ reflectance measurements of Fo_{90}, Fo_{99+}, and SiO_2, *Meteoritics & Planetary Science* 51, 261-275

Mahjoub, A., Poston, M.J., Blacksberg, J., Eiler, J.M., Brown, M.E., Ehlmann, B.L., Hodys, R., Hand, K.P., Carlson, R., and Choukroun, M. (2017) Production of Sulfur Allotropes in Electron Irradiated Jupiter Trojans Ice Analogs, *The Astrophysical Journal* 846, 148

Matsumoto, T., Harries, D., Miyake, A., and Langenhorst, F. (2018) Space weathering of iron sulfide grains from asteroid 25143 Itokawa, Presented at *The Meteoritical Society LXXXI* Abstract #6096

Matsumoto, T., Harries, D., Langenhorst, F., Miyake, A., and Noguchi, T. (2020) Iron whiskers on asteroid Itokawa indicate sulfide destruction by space weathering. *Nature Communications* 11, 1117 https://doi.org/10.1038/s41467-020-14758-3

Matsumoto, T., Noguchi, T., Tobimatsu, Y., Harries, D., Langenhorst, F., Miyake, A., and Hidaka H. (2021) Space weathering of iron sulfides in the lunar surface environment. *Gheochimica et Cosmochimica Acta*, 299, 69-84, https://doi.org/10.1016/j.gca.2021.02.013

Mcintyre, N. S., and Zetaruk, D. G. (1977) X-ray photoelectron spectroscopic studies of iron oxides, *Analytical Chemistry* 49, 1521-1529.

Meyer, F.W. (2018) He-ion induced surface morphology change and nanofuzz growth on hot tungsten surfaces, *Journal of Physics B: Atomic, Molecular, and Optical Physics* 52, 1-22

Moulder, J. F., Stickle, W. F., Sobol, P. E., Bomben, K. D., ed. Chastein, J. (1991) *Handbook of X-ray Photoelectron Spectroscopy*, Physical Electronics Inc.: Chanhassen, MN

Mutzke, A., Schneider, R., Eckstein, W., Dohmen, R., Schmid, K., Toussaint, U. v., et al.(2019). SDTrimSP Version 6.00 (IPP 2019-02). Max-Planck-Institut für Plasmaphysik: Garching. doi:10.17617/2.3026474

Nakamura, T., Noguchi, T., Masahiko, T., Zolensky, M., Kimura, M., Tsuchiyama, A. et al. (2011) Itokawa Dust Particles: A Direct Link Between S-Type Asteroids and Ordinary Chondrites. *Science*, 333, 1113-1116, doi:10.1126/science.1207758

Nittler, L.R., Starr, R.D., Lim, L., McCoy, T.,J., Burbine, T.H., Reedy, R.C., Trombka, J.I., Gorenstein, P., Squyres, S.W., Boynton, W.V., Mcclanahan, T.P., Bhangoo, J.S., Clark, P.E., Murphy, M.E., and Killen, R. (2001) X-ray fluorescence measurements of the surface elemental composition of asteroid 433 Eros, *Meteoritics & Planetary Science* 36, 1673-1695 https://doi.org/10.1111/j.1945-5100.2001.tb01856.x

Noguchi, T., Kimura, M., Hashimoto, T., Konno, M., Nakamura, T., Zolensky, M. E., Okazaki, R., Tanaka, M., Tsuchiyama, A., Nakato, A., Ogami, T., Ishida, H., Sagae, R., Tsujimoto, S., Matsumoto, T., Matsuno, J., Fujimura, A., Abe, M., Yada, T., Mukai, T., Ueno, M., Okada, T., Shirai, K., and Ishibashi, Y. (2014) Space weathered rims found on the surfaces of the Itokawa dust particles, *Meteoritics & Planetary Science* 49, 188-214

Oran, R., Wiess, B. P., and Cohen, O. (2018) Were chondrites magnetized by the early solar wind? *Earth and Planetary Science Letters* 492, 222-231 https://doi.org/10.1016/j.epsl.2018.02.013

Payne, B. P., Biesinger, M. C. and McIntyre, N. S. (2011) X-ray photoelectron spectroscopy studies of reactions on chromium metal and chromium oxide surfaces, *Journal of Electron Spectroscopy and Related Phenomena* 184, 29-37

Peplowski, P.N., Lawrence, D.J., Beck, A.W., Burks, M., Chabot, N.L., Goldsten, J.O., Wilson, J., Yokley, Z, and the Psyche Science Team. (2018) Nuclear Spectroscopy of Asteroid 16 Psyche, Presented at *Lunar and Planetary Science Conference XLIX* Abstract #2114

Petrovic, J.J. (2011) Mechanical properties of meteorites and their constituents, *Journal of Materials Science* 36, 1579-1583

Pieters, C. M., and Noble, S. K. (2016), Space weathering on airless bodies, *Journal of Geophysical Research – Planets* 121, 1865– 1884, doi:10.1002/2016JE005128.

Pieters, C.M., Taylor, L.A., Noble, S.K., Keller, L.P., Hapke, B., Morris, R.V., Allen, C.C., McKay, D.S., and Wentworth, S. (2000) Space weathering on airless bodies: Resolving a mystery with lunar samples, *Meteoritics & Planetary Science* 35, 1101-1107

Pinos, J., Mikmekova, A., and Frank, L. (2017) About the information depth of backscattered electron imaging, *Journal of Microscopy* 226, 335-342

Powell, C.J., Jablonski, A. (2010) NIST Electron Inelastic-Mean-Free-Path Database, *NIST Standard Reference Database 71* v. 1.2

Prince, B. S., Magnuson, M. P., Chaves, L. C., Thompson, M. S., & Loeffler, M. J. (2020). Space weathering of FeS induced via pulsed laser irradiation. *Journal of Geophysical Research: Planets*, 125, e2019JE006242. https://doi.org/10.1029/2019JE006242

Raines, J.M., Gershman, D.J., Zurbuchen, T.H., Sarantos, M., Slavin, J.A., Gilbert, J.A., et al. (2013) Distribution and compositional variations of plasma ions in Mercury's space environment: the first three Mercury years of MESSENGER observations. *Journal of Geophysical Research – Space Physics*, 118, 1604-1619

Rivkin, A.S., Howell, E.S., Lebofsky, L.A., Clark, B.E., and Britt, D.T. (2000) The nature of M-class asteroids from 3-μm observations, *Icarus* v. 145, p. 351-368

Roth J. (1983) Chemical sputtering. In: Behrish R. (eds) *Sputtering by Particle Bombardment II. Topics in Applied Physics*, v 52. Springer, Berlin, Heidelberg. https://doi.org/10.1007/3-540-12593-0_3

Roth, J., Bohdansky, _., and W. Otternberger, Report IPP 9/26 (1979) Max Planck Institut fur Plasmaphysik, Garching, FRG Sanchez, J.A., Reddy, V., Shepard, M.K., Thomas, C., Cloutis, E.A., Takir, D., Contrad, A., Kiddell, C., and Applin, D. (2017) Detection of rotational spectral variation on the M-type asteroid (16) Psyche, *The Astronomical Journal* v. 153, p. 1-8

Sasaki, S., Nakamura, K., Hamabe, Y., Kurahashi, E., and Hiroi, T. (2001) Production of iron nanoparticles by laser irradiation in a simulation of lunar-like space weathering, *Nature* 410, 555-557

Schaible, M. J., and Baragiola, R. A. (2014), Hydrogen implantation in silicates: The role of solar wind in SiOH bond formation on the surfaces of airless bodies in space, *Journal Geophysical Research Planets* 119, 2017–2028

Schaible, M. J., Dukes, C. A., Hutcherson, A. C., Lee, P., Collier, M. R., & Johnson, R. E. (2017). Solar wind sputtering rates of small bodies and ion mass spectrometry detection of secondary ions, *Journal of Geophysical Research: Planets* 122, 1968– 1983. https://doi.org/10.1002/2017JE005359

Schaible, M. J., Pinto, H. P., McKee, A. D., Leszczynsky, J., and Orlando, T. M. (2019) Characterization and Simulation of Natural Pyrite Surfaces: A Combined Experimental and Theoretical Study. *Journal of Physical Chemistry* 123, 26397-26405, https://doi.org/10.1021/acs.jpcc.9b07586

Scherzer, B.M.U. (1983) Development of Surface Topography dues to Gass ion Implantation, in *Sputtering by Particle Bombardment II*, ed. R. Behrisch, Springer-Verlag: New York

Schläppi, B., Altwegg, K., and Wurz, P. (2008) Asteroid exosphere: A simulation for the ROSETTA flyby targets (2867) Steins and (21) Lutetia, *Icarus* 195, 674-685

Schmitz, J., Mutzke, A., Litnovsky, A., Klein, F., Tan, X.Y., Wegener,T., Hansen, P., Aghdassi, N., Eksaeva, A., Rasinski, M., Kreter, A. J., Gonzalez-Julian, J., Coenen, J. W., Linsmeier, Ch., and Bram, M. (2019) Preferential sputtering induced Cr-Diffusion during plasma exposure of WCrY smart alloys, *Journal of Nuclear Materials* 526, 151767

Shabanova, I. N. and Trapeznikov, V. A. (1975) A study of the electronic structure of Fe3C, Fe3Al and Fe3Si by photoelectron spectroscopy, *Journal of Electron Spectroscopy and Related Phenomena* 6, 297-307

Shirley, D.A. (1972) High-Resolution X-Ray Photoemission Spectrum of the Valence Bands of Gold *Physical Review B* 5, 4709

Sinha, S. and Mukherjee, M. (2018) A study of adventitious contamination layers on technically important substrates by photoemission and NEXAFS spectroscopies, *Vacuum* 148, 48-53

Skala, R., Cosarova, I., and Drabek, M. (2006) Inversion twinning in troilite, *American Mineralogist* 91, 917-921

Skinner, W. M., Nesbitt, W. H., and Pratt, A. R. (2004) XPS identification of bulk hole defects and itinerant Fe 3d electrons in natural troilite *Geochimica et Cosmochimica Acta* 68, 2259–2263

Stadlmayr, R. et al. (2018). Fluence dependent changes of surface morphology and sputtering yield of iron: Comparison of experiments with SDTrimSP-2D. *Nuclear Instruments and Methods in Physics Research Section B: Beam Interactions with Materials and Atoms* 430, 42-46. doi:10.1016/j.nimb.2018.06.004.

Starukhina, L.V. (2001) Water detection on atmosphereless celestial bodies: Alternative explanations of the observations, *Journal of Geophysical Research* 106, 14,701-14,710

Szabo, P. S. et al. (2018) Solar wind sputtering of wollastonite as a lunar analogue material – Comparisons between experiments and simulations. *Icarus*, 314, 98-105

Szabo, P. S. et al. (2020a). Dynamic Potential Sputtering of Lunar Analog Material by Solar Wind Ions. *The Astrophysical Journal* 891, 100

Szabo, P. S., Biber, H., Jäggi, N., Wappl, M., Stadlmayr, R., & Primetzhofer, D., et al. (2020b). Experimental insights into space weathering of phobos: laboratory investigation of sputtering
by atomic and molecular planetary ions. *Journal of Geophysical Research: Planets*, 125, e2020JE006583. https://doi.org/10.1029/2020JE006583

Taglauer, E. and Heiland, W. (1976) Surface analysis with low energy ion scattering, *Applied Physics* 9, 261–275

Takir, D., Reddy, V., Sanches, J.A., Shepard, M.K., and Emery, J.P. (2017) Detection of water and/or hydroxyl on asteroid (16) Psyche, *The Astronomical Journal* 153, 31-37

Tanyeli, I., Marot, L., Mathys, D., van de Sanden, M.C.M, and De Temmerman, G. (2015) Surface Modification Induced by High Fluxes of Low Energy Helium Ions, *Scientific Reports* 5, 1-9

Terranova, U., Mitchell, C., Sankar, M., Morgan, D., and de Leeuw, N. H. (2018) Initial oxygen incorporation in the prismatic surfaces of troilite FeS, *Journal of Physical Chemistry* 122, 12810-12818

Thomas, J. E., Skinner, W. M., and Smart, R. (2003) A comparison of the dissolution behavior of troilite with other iron(II) sulfides; implications of structure, *Geochimica et Cosmochimica Acta* 67, 831–843

Thompson, M.S., Zega, T.J., and Howe, J.Y. (2017) In situ experimental formation and growth of Fe nanoparticles and vesicles in lunar soil, *Meteoritics & Planetary Science* 52, 413-427 https://doi.org/10.1111/maps.12798

Thompson, M.S., Loeffler, M.J., Morris, R.V., Keller, L.P., and Christoffersen, R. (2019) Spectral and chemical effects of simulated space weathering of the Murchison CM2 carbonaceous chondrite, *Icarus* 319, 499-511

Tosi, F., Carrozzo, F.G., Raponi, A., De Sanctis, M.C., Thangjam, G., Zambon, F., Ciarniello, M., Nathues, A., Capria, M.T., Rognini, E., Ammannito, E., Hoffmann, M., Krohn, K., Longobardo, A., Palomba, E., Pieters, C.M., Stephan, K., Raymond, C.A. and Russell, C.T. (2018), Mineralogy and temperature of crater Haulani on Ceres. *Meteoritics and Planetary Science*, 53: 1902-1924

von Toussaint, U.; Mutzke, A.; Sugiyama, K.,; and Schwarz-Selinger, T. (2016) Simulation of coupled sputter-diffusion effects. *Physica Scripta* T167, 014023

Wagner, C.D., Davis, L.E., Zeller, M.V., Taylor, J.A., Raymond, R.H. and Gale, L.H. (1981), Empirical atomic sensitivity factors for quantitative analysis by electron spectroscopy for chemical analysis. *Surface and Interface Analysis* 3, 211-225. https://doi.org/10.1002/sia.740030506

Watson, E. B.; Cherniak, D. J.; Frank, E. A. (2009) *Geochimica Cosmochimica Acta* 73, 4792

Wittmaack, K., & Mutzke, A. (2017). Highly accurate nuclear and electronic stopping cross sections derived using Monte Carlo simulations to reproduce measured range data. *Journal of Applied Physics* 121, 105104. doi:10.1063/1.4978016.

Wu, Y., Li, X., Yao, W., and Wang, S. (2017) Impact Characteristics of Different Rocks ina Pulsed Laser Irradiation Experiment: Simulation of Micrometeorite Bombardment on the Moon. *Journal of Geophysical Research: Planets*, 122, 1956-1967. https://doi.org/10.1002/2016JE005220

Yamamura, Y. and Tawara, H. (1996) Energy Dependence Of Ion-Induced Sputtering Yields From Monatomic Solids At Normal Incidence, *Atomic Data and Nuclear Data Tables*, v. 62, p. 149-253Yang, J.C., Pitts, W.M., Fernandez, M., and Prasad, K. (2013) Measurements of Effective Diffusion Coefficients of Helium and Hydrogen through Gypsum, *International Journal of Hydrogen Energy* 38, 8125-8131

Yao Y., Hargitai, Z., Albert, M., Albridge, R.G., Barnes, A.V., Gilligan, J.M., Pratt Ferguson, B., Lüpke, G., Gordon, V.D., and Tolk, N.H. (1998) New Molecular Collisional Interaction Effect in Low-Energy Sputtering, *Physical Review Letters* 81, 550

Yon, S. A. and Pieters, C. M. (1987) Interactions of light with rough dielectric surfaces – Spectral reflectance and polarimetric properties. Proceedings, *Lunar & Planetary Science Conference XVIII*, 581-592

Zhang, L.; Tang, G.; Ma, X., (2010) Long range effect of ion irradiation on diffusion, *Physics Letters A*, 374, 2137-2139.

Zhu, C., Góbi, S., Abplanalp, M. J., Frigge, R., Gillis-Davis, J. J., & Kaiser, R. I. (2019). Space weathering-induced formation of hydrogen sulfide (H_2S) and hydrogen disulfide (H_2S_2) in the murchison meteorite. *Journal of Geophysical Research: Planets*, 124, 2772– 2779.

Ziegler, J. F., Biersack, J. P., and Ziegler, M. D. (1985) *SRIM – The Stopping and Range of Ions in Solids*, SRIM Co.: Chester, MD

Zurbuchen, T.H., Raines, J.M., Gloeckler, G., Krimigis, S.M., Slavin, J.A., Koehn, P.L., et al. (2008) MESSENGER observations of the composition of Mercury's ionized exosphere and plasma environment. *Science,* 321, 90-92

CHAPTER 3: LASER IRRADIATION OF IRON METEORITES: REGOLITH PARTICLE FORMATION BY THERMALLY DRIVEN MECHANICAL BREAKDOWN

Authors: J. M. Christoph, M. J. Loeffler, T. Sharp

Abstract:

While laser ablation is typically used to simulate space weathering by micrometeorite impact in stony materials, metallic asteroids may be subject to additional, potentially novel mechanisms of thermally driven surface modification. Thus, we have performed a suite of laser irradiation experiments on four constituent minerals of iron meteorites. We observe textures and fracture patterns in the laser-irradiated regions consistent with thermally driven mechanical failure both above and below the melting temperature of the respective minerals. Morphological and topographic changes are consistent with thermal expansion, plastic deformation, localized melting, decomposition, and outgassing. The resulting highly fractured surface may promote further breakdown by subsequent sources of mechanical stress. We hypothesize that on a metallic planetary surface, thermal stress at temperatures below the melting temperature of the surface material may play an important role in space weathering, regolith formation, gardening, and other surface evolution processes.

3.1. Background:

Laser ablation experiments have been used in recent years to simulate micrometeoroid impacts (Sasaki et al. 2001, Loeffler et al. 2008, Loeffler et al. 2016, Gillis-Davis et al. 2017), a primary mechanism for both regolith formation and space weathering. While larger impacts can effectively break down a solid planetary surface

into smaller blocks, smaller impacts are generally more frequent (Neukum et al. 1974) and pulverize those surface blocks into progressively finer powder *in-situ* (Gault 1970, Melosh 2011). Over geologic time, many subsequent impacts "garden" this pulverized surface, cycling additional large blocks to the surface where they are broken down, deepening the equilibrium thickness of the resulting regolith (Gault 1970, Housen et al. 1979, Durda 1999, Moretti et al. 2007, Durda et al. 2011). Micrometeorite impacts produce characteristic petrologic features within their resulting craters and surrounding rock – e.g. glassy material within the crater, spallation deposits, and halos of highly shocked material – which are distinct from the signatures left by other planetary surface processes (Hörz et al 2020). Micrometeorite impacts have also been associated with the formation of nanophase iron particles (npFe) (Sasaki et al. 2001, Moretti et al. 2007, Loeffler et al. 2016, Thompson et al. 2019) and have been invoked as a source of thermal energy to drive diffusion within the near surface of mineral grains (Chapman 2004, Loeffler et al. 2008). Both processes are key mechanisms in space weathering, observed as changes in the spectra and albedo of airless planetary surfaces (Gold 1955, Hapke 2001), and the ability of laser irradiation to reproduce these space weathering features has motivated its extensive use as a laboratory analog method for the process (Sasaki et al. 2001, Loeffler et al. 2008, Prince et al. 2020).

As compared to a microscopic impact, nanosecond-duration laser pulses can deliver similar energy over a similar interaction volume, with the advantage that the incident energy is uniform across the laser-irradiated surface (Sasaki et al. 2001, Prince et al. 2020). However, the laser does not directly replicate the process of an impact. Heating by absorption of incident photons is the primary mode by which energy from the laser is

transferred to the sample (Sasaki et al. 2001), with excavation and shock resulting from explosive superheating (Gregossian et al. 2009, Ehsani et al. 2021), rather than mechanical compression (Melosh 2011). This thermal energy component is nevertheless important in both space weathering and regolith formation, independent of whether a laser or a micro-impact is the heat source. In space weathering, heat from micrometeoroid impacts drives diffusion of atoms from below the penetration depth of incident ion irradiation, which can help propagate the space-weathered surface from nanometer-scales to thicknesses comparable to the information depth of optical remote sensing (Chapman 2004, Loeffler et al. 2008, Christoph et al. 2022). At the same time, other thermally-driven process can also mechanically modify airless planetary surfaces – examples include fatigue breakdown from diurnal and annual temperature cycling (Molaro and Byrne 2012, Delbo et al. 2014, Molaro et al. 2017), re-solidification of melt from larger impacts (Hörz et al. 2020), and contact metamorphism associated with igneous processes (Melosh 2011).

On a metallic asteroid surface, such as we plan to explore with the NASA Psyche Mission, the material properties of metals suggest potentially novel modes of thermally driven surface modification. The high thermal conductivity of metals might imply heat from remote sources could modify material at greater depth or distance than would occur under the same conditions on a stony object (Porneala and Willis 2006). Likewise, the ductile behavior of metals may enable modes of thermally driven mechanical deformation absent on surfaces composed of more brittle stony minerals (Marchi et al. 2020). Finally, high-temperature processes common on rocky planetary surfaces may

have metallic equivalents, albeit with dramatically different geomorphology, such as ferrovolcanism (Abrahams and Nimmo 2019).

Given the variety of thermally-driven processes hypothesized on metallic asteroid surfaces, it is useful to establish experimentally how rapid heating can alter analog metallic materials. In this study, we use laser irradiation to simulate rapid heating driven by micrometeoroid impacts or other natural processes on an asteroid surface. Using scanning electron microscopy (SEM) imaging, we compare the morphological and compositional changes resulting from laser irradiation on metallic and nonmetallic constituent minerals of iron meteorites. We use the results to estimate what characteristics may be observed on a thoroughly space-weathered metallic asteroid surface, such as we may find at Psyche.

3.2. Methods:

3.2.1. Samples

We chose to study two thick section slabs from the Canyon Diablo meteorite. The first thick section is 1.5 cm x 1.0 cm, consisting mostly of kamacite with an irregular ~5 mm schreibersite inclusion near the center. We obtained element maps of the thick section containing the schreibersite inclusion using a combination of Energy-Dispersive and Wavelength-Dispersive X-ray Spectroscopy (EDS / WDS) on the JEOL 8530 EPMA at the ASU Eyring Materials Center (Figure 3.1). Using vibratory polishing, we polished one side of each of our thick samples to a surface roughness < 1 μm to maximize visibility of any surface modification occurring during laser irradiation.

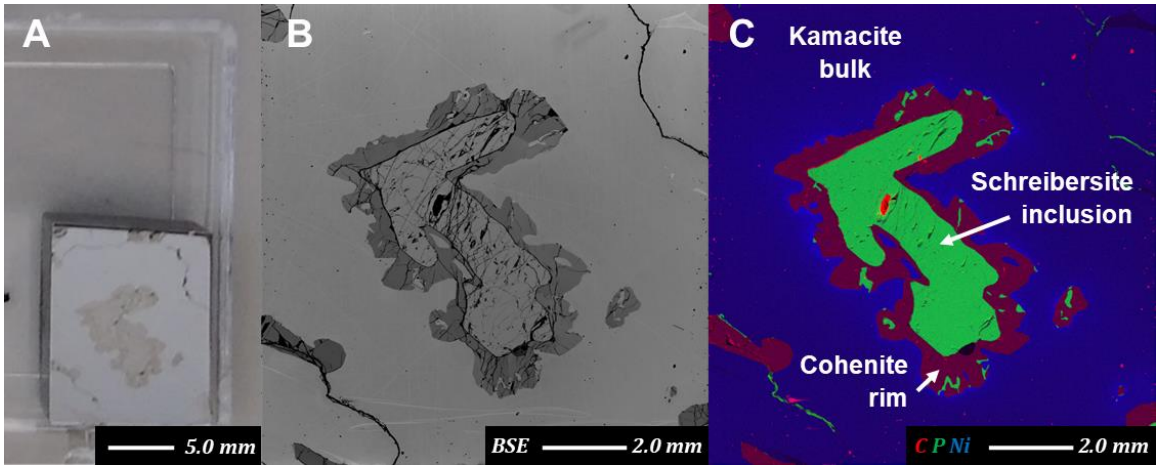

Figure 3.1. Three views of the polished thick section of Canyon Diablo used in this experiment. A) photograph of the sample in its storage box. B) a backscatter electron microscope image of the thick section surface. C) an elemental abundance map made with Energy-Dispersive X-ray spectroscopy. Three mineral phases predominate: the bulk is single-crystal kamacite (FeNi), with an irregular schreibersite ($[FeNi]_3P$) inclusion in the center surrounded by cohenite (Fe_3C). Additional cohenite inclusions are present elsewhere on the sample surface, and smaller graphite and rhabdite inclusions are visible as single pixels scattered within the bulk metal.

The schreibersite inclusion ($[FeNi]_3P$) is surrounded by a cohenite (Fe_3C) rim. Despite the difficulty of measuring carbide phases using EPMA, Canyon Diablo is carbon-saturated and cohenite rims are typically present around its schreibersite inclusions (Buchwald 1975). All troilite (FeS) inclusions in this sample are smaller than the laser spot diameter, thus we separately irradiated a second thick section with comparable dimensions cut from a large Canyon Diablo troilite nodule.

3.3.2. Laser Irradiation

We irradiated our sample using a Continuum Minilite Nd-YAG (1064 nm) laser, which emits 6-8 ns pulses at 1 Hz. The laser beam entered the chamber through a glass window and was imaged onto the sample at normal incidence. The resulting spot size on the sample was measured to be ~0.7 mm (~0.4 mm^2); each pulse had an energy fluence of ~10 J/cm^2. Unlike previous studies attempting to irradiate a large sample area to obtain

optical reflectance spectra of a simulated “fully weathered” surface (Prince et al. 2020; Thompson et al. 2020), here we performed a suite of individual pulses on each phase on the sample surface, with >1 mm lateral spacing between each ablated area, so the modification resulting from a single pulse could be analyzed with electron microscopy.

3.3.3. Electron Microscopy

We imaged the laser-irradiated regions using two Field-Emission Scanning Electron Microscopes (SEM) at the ASU Eyring Materials Center: the FEI XL 30 and the Thermo-Scientific Helios 5 UX. Except where indicated on the images, we maintained the electron beam voltage at 10 kV for the XL30 and 20 kV for the Helios instruments. We initially used both backscatter (BSE) and secondary (SE) imaging for low-magnification survey images, while subsequently relying on secondary imaging with the Everhard-Thornley Detector on both instruments for higher-magnification investigations of detailed features.

3.3. Results:

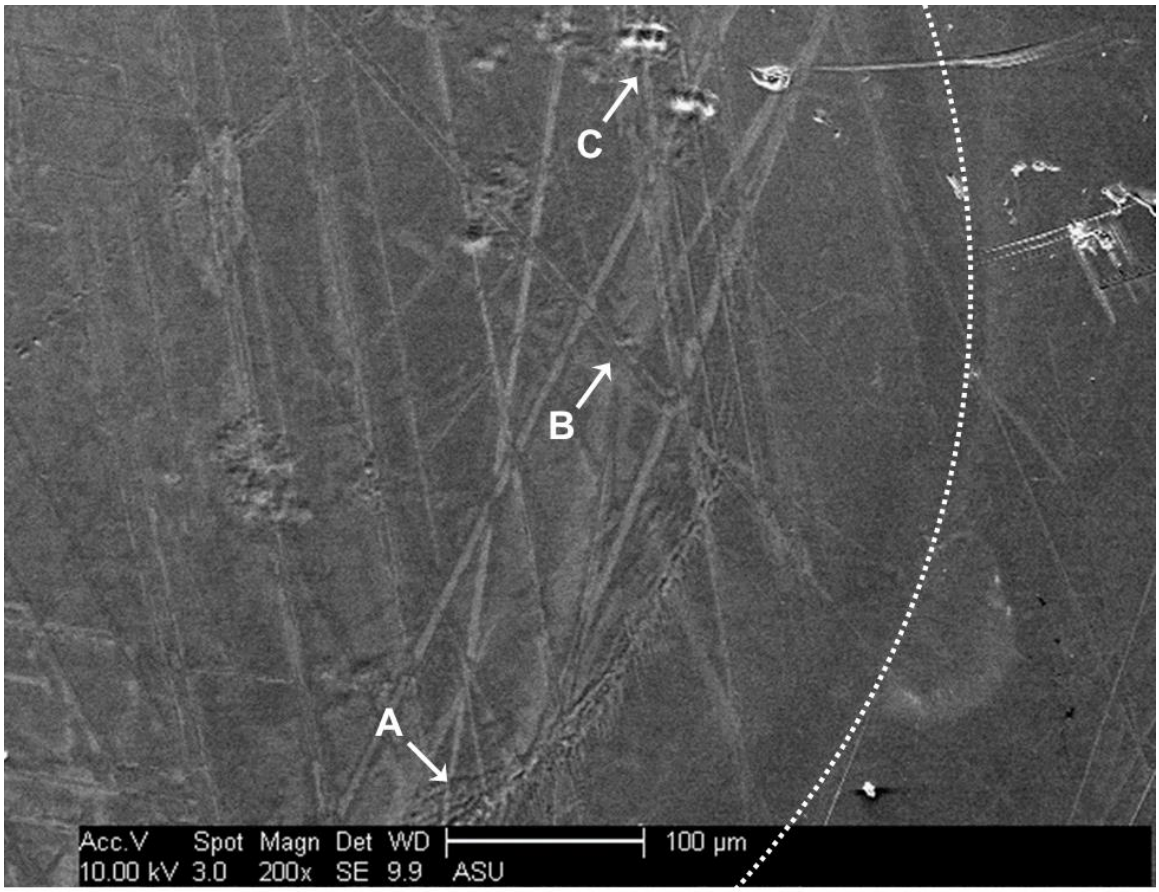

Figure 3.2. *Secondary electron image centered on the edge of a laser spot on bulk kamacite, with the laser-irradiated material inside the dashed circle. The SE detector and resulting apparent illumination is at the top of the image. An irregularly curved ripple or ridge (A) forms ~100 microns inside the irradiated area. The diagonal lineations crossing the image near the center (B) are polishing scratches with exaggerated topography, as compared to equivalent un-irradiated scratches in the bottom-right corner. A cluster of 10-micron-diameter circular depressions appears at the top center (C).*

The edge of the 1-mm-diameter laser spot in Kamacite is visible as a faint dark ring (Figure 3.2), with a set of curved ripples or ridges approximately 10 μm wide and 100 μm inward from the edge. Polishing scratches visible as fine lineations on the unirradiated side are exaggerated within the laser-irradiated region, as the scratches appear wider and have higher contrast with the surrounding material. Rounded

depressions approximately 1-10 microns in diameter appear in clusters throughout the laser-irradiated region.

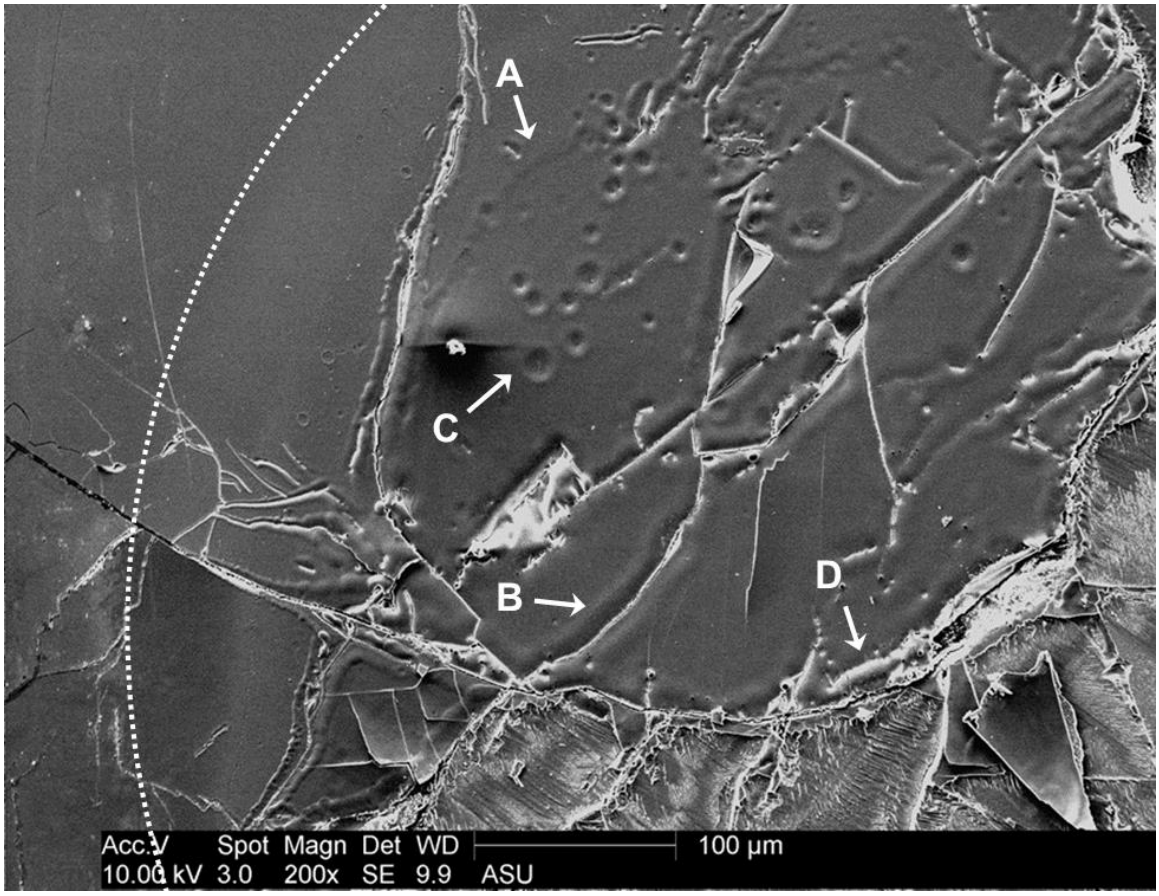

Figure 3.3. An SEM image of the top-left corner of a laser spot irradiating the schreibersite inclusion (center) and the cohenite rim (lower right), with irradiated material inside the dashed circle. The lower portion of this image and the same laser spot partially overlap Figure 3.4, so we focus on the schreibersite here. An irregular curved ripple or ridge forms ~100 microns inside the edge of the irradiated area (A). Pre-irradiation fractures and scratches are highly exaggerated, with ~10μm-wide rounded ridges running parallel on either side (B). Numerous circular depressions are present in the irradiated area, ranging in diameter from 20 microns down to sub-micron (C). Deformation is particularly extensive within a few microns of the schreibersite grain boundary (D).

The edge of the laser spot in Schreibersite (Figure 3.3) is again visible as a faint bright ring and a curved ripple ~100 μm inward from the edge of the irradiated area. The edges of pre-irradiation fractures and scratches within the Schreibersite are highly

topographically exaggerated into smooth, well-rounded ridges as wide as 10 μm. Many circular depressions are visible in the laser-irradiated schreibersite, ranging in diameter from 20 μm to sub-micron pits. Both the circular depressions and the exaggerated edges resemble those observed in the kamacite but their topography is greater and their morphology is more distinctly visible. The extent of deformation is greatest near the schreibersite grain boundary, with a greater frequency of smaller fractures and circular depressions within ~10 microns of adjacent grains, while features within the schreibersite interior are larger and less frequent.

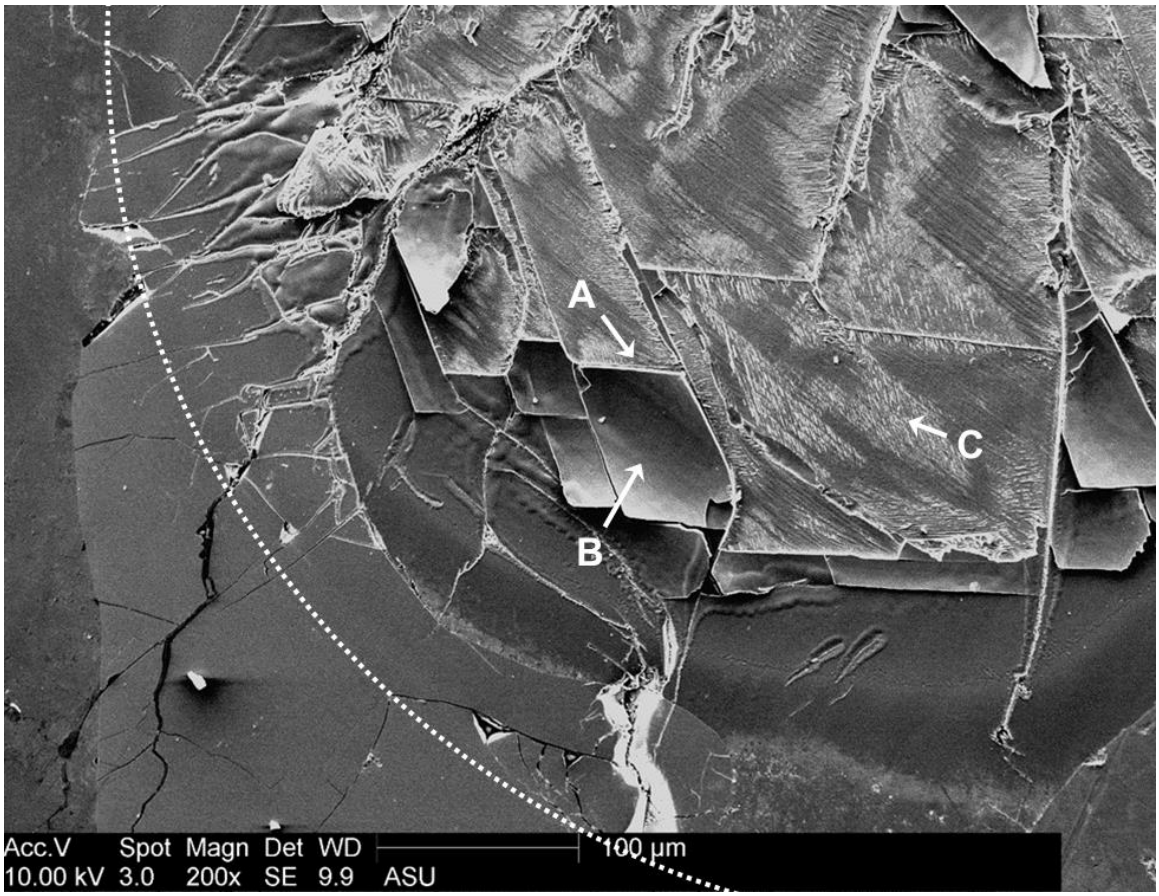

Figure 3.4. The same laser spot as shown in Figure 3.3 but focusing on the cohenite rim. The edge of the laser spot is again visible as a faint darkening of the material, with the irradiated region inside the dashed circle. Numerous linear fractures are visible in three parallel orientations within the irradiated region (A). Two types of surfaces are visible

between the fractures: dark, smooth, concave, parallelogram-shaped flakes or plates (B); and bright, rough, flat, striated regions (C).

Fractures crisscross the laser-irradiated cohenite (Figure 3.4). Some fractures correspond to pre-irradiation cracks and scratches visible in backscatter imaging (Figure 1). The remaining fractures are strongly linear and in parallel sets with at least three orientations. On the left side of the image, some fractures appear to propagate from the cohenite into adjacent mineral grains, though notably not into the kamacite bulk.

Between these fractures are two types of surfaces: smooth, thin, polygonal plates; and brighter regions indicating fine-scale roughness (Figure 3.5). The smooth plates are slightly curved and concave upward with their edges raised above sample surface. Bright contrast on the flake edges reveals a thickness of up to a few μm. The brighter, rougher surface regions consist of sub-parallel terraces separated by angular ridges ~1 μm apart. The more prominent ridge crests stand out as high contrast features in secondary electron imaging.

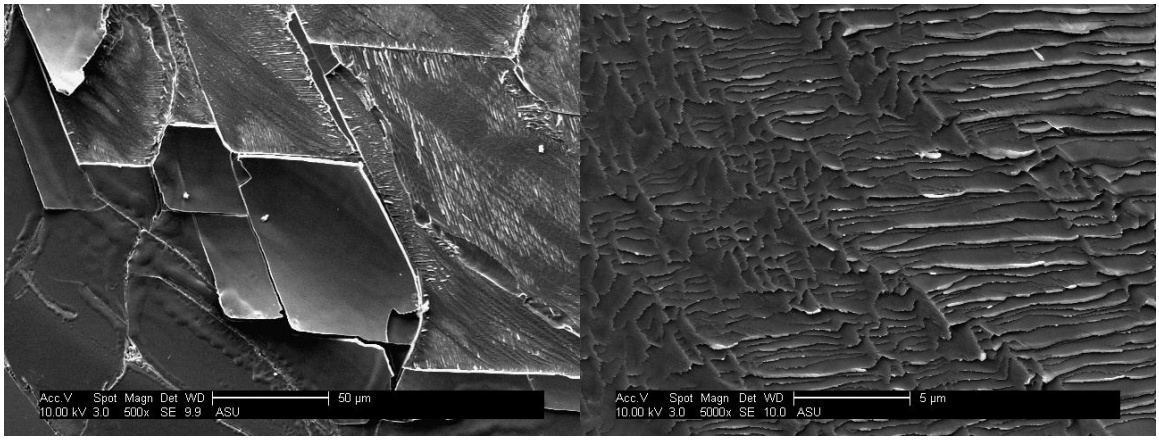

Figure 3.5. Higher-magnification SEM images of the smooth plates near the center of Figure 3.4 (left) and the rough surface immediately above them (right). The ETD detector and corresponding apparent illumination is at the top. On the left, concave flakes are dark on the upper surface where they are relatively shadowed, with bright edges in direct illumination. On the right, parallel and sub-parallel bright linear features indicate edges of a stepped or striated fracture surface.

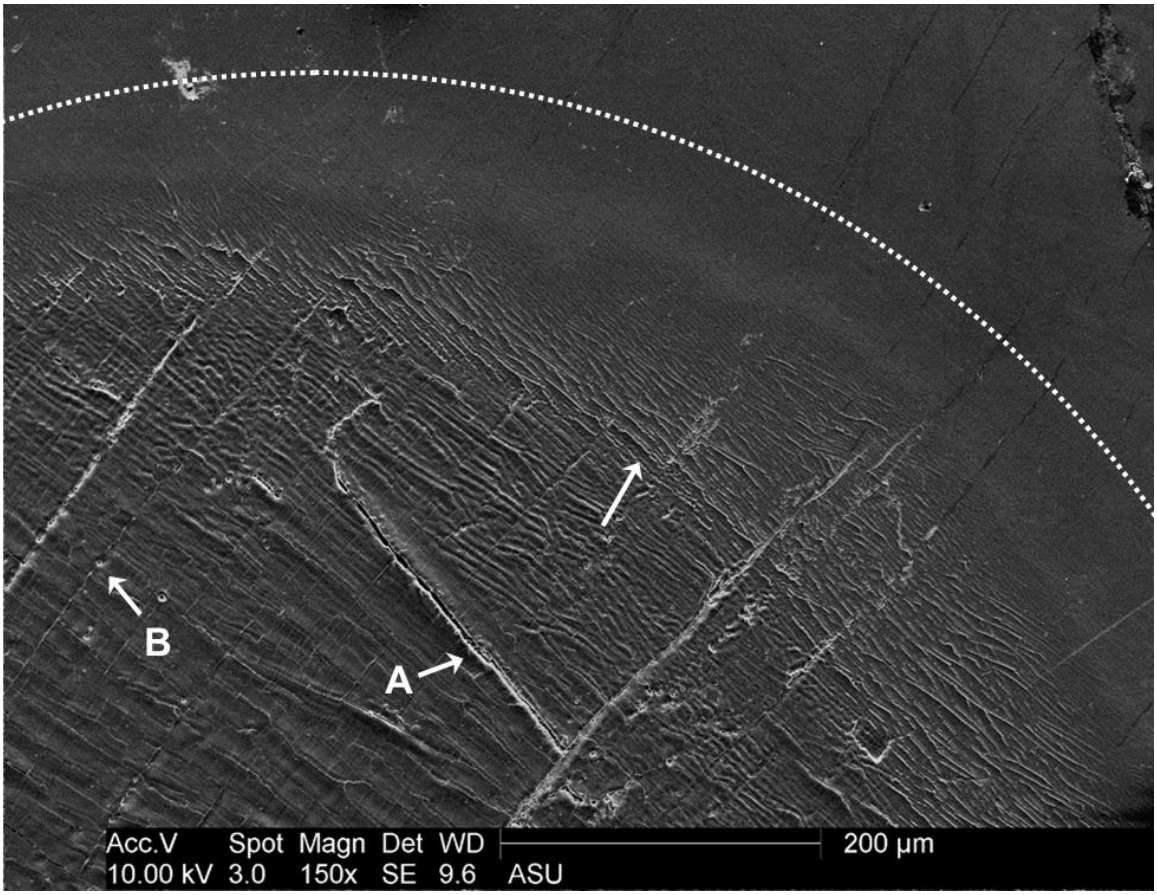

Figure 3.6. SEM image of a laser irradiated troilite surface. A faint, bright ring marks the edge of the laser spot, with the irradiated material inside the dashed circle. Parallel to sub-parallel bright linear features in the irradiated region correspond to fractures with topographically exaggerated edges that take the form of rounded ripples or ridges (A). 10 micron and smaller circular depressions are concentrated close to these ridges, although some are visible solitary or in clusters, e.g.(B).

Multiple sets of parallel fractures are visible in the irradiated troilite (Figure 3.6). The widest fractures continue into the unirradiated region while the smaller, more closely spaced fractures terminate near the edge of the laser spot. The sides of each fracture are accentuated by raised ridges similar to those observed in schreibersite but appearing less rounded and with sharper exposed edges. Near the fractures themselves, the ridges are pockmarked with micron-scale circular pits along the exposed edge. In some places,

linear chains of these pits extend outward from the fractures and may in turn open into new fractures. Among the fractures contained within the laser-irradiated region, those closer to the edge of the laser spot appear shorter, more closely spaced, and with more-exaggerated ridges than those toward the center of the laser spot.

To summarize, we observe a consistent range of deformation features across the four minerals. All four phases feature a faint change in SEM image contrast at the edge of the laser-irradiated area, with an annular ripple or ridge approximately 100 microns inward. Within the schreibersite, troilite, and cohenite, we observe formation of new fractures and expansion of existing ones, features absent in the kamacite. In the irradiated kamacite, schreibersite, and troilite we observe contrast-exaggerated scratches, while the cohenite surface is modified extensively enough to erase any evidence of this process. We also observe circular depressions in all four phases, consistent with either plastic deformation (kamacite), vesiculation (troilite, cohenite), or both (schreibersite). Where the laser irradiated area overlaps a grain boundary, as in the schreibersite and cohenite, we observe an increase in extent of deformation, as compared to the bulk interior of the same phases, and especially as compared to the kamacite. Only cohenite exhibits formation and removal of thin plates between newly-formed fractures, and as we discuss below the most likely mechanism is unique to this mineral. While these features may be grouped and discussed together, they each occur under different thermal conditions and may thus require subtly different explanations.

3.4. Discussion:

3.4.1. Surface heating by laser absorption.

Multiple potential mechanisms are consistent with the deformation and fracture observed in each mineral phase, all relying on the laser irradiation heating the surface. However, the extent of modification on each phase depends both on the mineral and on the surface geometry. Absorption and ablation efficiency of laser energy increases with surface roughness (Ihlemann et al. 1992), such that highly polished reflective or transparent surfaces may be minimally modified at low laser fluences until sufficient defects can form to increase absorption. In similar laser irradiation experiments, Loeffler et al. (2016) found that multiple laser pulses were required to melt samples of silica, olivine, and synthetic forsterite, with smoother surfaces exhibiting minimal mechanical deformation or chemical alteration. It is thus striking that we observe any surface modification at all on our vibrationally polished surfaces irradiated with single laser pulses. A more thorough quantification of how much laser energy is absorbed by each phase will be forthcoming. Based on the smooth surface texture, we estimate the laser-heated kamacite reflected the majority of the incident laser energy, but was still significantly heated. The circular ripples and depressions may represent small areas within the laser spot where the kamacite locally melted, perhaps due to microscopic structural heterogeneities or inclusions. The high surface temperature required to melt kamacite would also cross the kamacite-taenite phase transition temperature (Yang et al. 1996), however we lack a means to measure this transition in our sample if it indeed occurred during laser irradiation. The lack of an obvious ablation crater indicates the kamacite did not approach the thermodynamic critical temperature necessary for laser-induced phase explosion (Porneala and Wills 2006, Gregossian et al. 2009). We thus

attribute the modification observed in kamacite either to melting and solidification, or to plastic deformation below the melting temperature.

The thermodynamics of cohenite are significantly more complex than for kamacite. Cohenite initially crystallizes when an iron-carbon alloy containing >6 wt.% C crystallizes from a melt below 2110 K (Biele et al. 2022). However, at atmospheric pressure cohenite becomes unstable below ~1300 K and decomposes to ferrite + graphite (Ringwood 1960). Cohenite inclusions in meteorites are preserved below ~1000 K because diffusion is too slow for the decomposition reaction to proceed (Ringwood 1960), and they are preserved only in those iron meteorites in which alloying elements like Ni extend the cohenite stability field into the 1000-1300 K temperature range (Robin 1966). However, when cohenite samples are heated above 1000 K in laboratory experiments, they can decompose over time scales ranging from minutes to years, depending on the rate of graphite nucleation (Lipschutz and Anders 1964). While such time scales are orders of magnitude longer than the nanosecond duration of the laser pulse, the well-established heat-sensitivity of cohenite in the 1000-1300 K range is relevant to interpreting the observed fractures.

The troilite surface exhibits the greatest extent of textural modification consistent with melting, such as vesicles and melt cracks. Troilite can also undergo a decomposition reaction to ferrite + sulfur gas at elevated temperature, but unlike cohenite, troilite remains stable up to the pyrrhotite eutectic at 1260 K (Ferro et al. 1989). It is therefore likely that the laser-irradiated surface of the troilite did indeed melt rather than decompose, but it may have also partially vaporized with loss of sulfur, contributing to vesicle formation.

3.4.2. Deformation in Kamacite and Schreibersite

The kamacite and schreibersite are the most morphologically similar phases, albeit the degree of surface modification is significantly greater in schreibersite than in kamacite. No significant fractures are present in the kamacite before or after irradiation, only widened and deepened polishing scratches. It is tempting to attribute the presence of fractures in schreibersite to the proximity of the grain boundary with the cohenite rim, which would geometrically constrain thermal expansion occurring at different rates in each phase. Similar mechanics have been invoked in other petrologic examples of thermally-driven plastic deformation, including weathering of Rapakivi Granite (Backlund 1938), Zener pinning (Smith 1948), and two-phase grain flow (Bercovici 2012). However, although we observe more frequent fractures, ridges, and vesicles near the schreibersite grain boundary, there is not enough evidence to attribute these features to any specific mechanism of grain-boundary-constrained deformation. The simplest and most plausible explanation for the features observed in both kamacite and schreibersite is plastic deformation by thermal expansion as the surface approaches the melting temperature of each mineral. The greater extent of modification in schreibersite as compared to kamacite may be due to the kamacite surface being smoother, and thus containing both fewer and smaller surface defects before irradiation, consistent with previous laser irradiation experiments (Loeffler et al 2016).

3.4.3. Fracture in Cohenite

The parallel fractures and thin plates that form in the cohenite warrant a more specific mechanism than simple plastic deformation. Although flat, planar fragments are typical among impact ejecta (Michikami et al. 2016), these are mechanistically dissimilar

due to absence of shock in our experiment. The flat edges of the plates appear to be defined by linear fractures that form in multiple parallel sets during the laser pulse. The concave upper faces with upturned edges and corners indicate the plates are lifting off the surface in a manner resembling delamination. We interpret the rough surfaces of parallel ridges between the linear fractures as regions where plates have been removed completely, exposing the material underneath. We will discuss each step in more detail.

Delamination is most common along interfaces beneath and parallel to the surface, as in exfoliation and sheeting of a thin surface layer or coating (Holzhausen 1989, Martel 2017). The only possible thin surface layer on the cohenite would be a surficial oxide coating formed during sample storage or preparation. However, the approximately 1-μm thickness of the plates as shown in Figure 3.5 is comparable to the information depth of the EDS detector used to measure the surface elemental composition prior to laser irradiation. If the plates represent a delaminating surface oxide ~1 μm thick, that layer would have been detected during initial EPMA analysis, however we did not measure significant oxygen abundance in the cohenite or any other mineral phase on the sample.

In a cohesive single-layer material, delamination can also occur by fracture propagation parallel to the surface with similar mechanics to other non-interfacial fracture growth modes, provided a source of stress with the correct orientation (Liechti 2008). The thickness of the plates is comparable to the thermal skin depth calculated in *3.4.1* above, suggesting that the plates may form by horizontal fracture propagation at the lower extent of the region heated by the laser pulse. The rough surface of parallel ridges left behind underneath the plates suggests these fractures may not be perfectly horizontal

relative to the sample surface, but instead follow the internal microstructure of the cohenite or defects therein.

Finally, we must discuss the role the cohenite decomposition reaction at 1000-1300 K may play in the formation of the fractures. The three apparent preferred orientations of the parallel linear fractures are consistent with the crystallographic planes of cohenite's crystal structure. As the decomposition reaction initiates, graphite crystals would preferentially nucleate and grow along these planes. It is thus possible that the fractures form as the heated cohenite surface cools, with nucleated graphite crystals providing weak points along which the fractures propagate both across the surface and horizontally beneath it. However, we do not directly observe any graphite crystals on the irradiated cohenite surface, and so cannot confirm this interpretation.

3.4.4. Troilite fracture and melting

The fractures, pits, and ridges observed in the troilite surface are all consistent with melting and accompanying thermal expansion. The presence of multiple sets of parallel fractures in the troilite surface initially appears similar to the cohenite but without the distinct plates, suggesting that these fractures may be crystallographically controlled. However, the fractures in troilite are more sinuous than those in the cohenite and may instead be forming along some other internal fabric of the mineral. Notably, the circular pits and depressions in troilite are significantly more abundant, deeper, and more closely associated with the fractures than those in the other three minerals. It is likely that these pits are a product of sulfur gas released from vesicles as the troilite decomposes.

We can directly compare these results with previous laser irradiation experiments on troilite surfaces. Prince et al. (2020) irradiated pressed pellets of troilite powder with

the same laser apparatus as used in our experiment, finding evidence of surface melt and deformed boundaries on grains irradiated with 8 laser pulses, similar to the melting and modified fractures observed in our experiment. Continued irradiation through hundreds of laser pulses produced an Fe-enriched surface bearing little resemblance to the troilite grains' original morphology and structure, but with optical reflectance spectra consistent with thermally driven decomposition. We therefore interpret the fracture growth, melting, and vesiculation observed in our laser-irradiated troilite thick section as very early stages of the processes Prince et al. (2020) observed in laser-irradiated troilite powder.

3.4.5. Relationship of fracture initiation with regolith formation.

Fracture nucleation is an important step for regolith formation by thermal fatigue. Fatigue refers to the breakdown and failure of a material under cyclic stress loading, such as thermal expansion and contraction. Long studied as a problem in engineered materials, fatigue driven by the expansion and contraction of rocks during diurnal and seasonal temperature changes has been proposed as a regolith formation mechanism on airless planetary surfaces (Molaro and Byrne 2012, Molaro et al. 2017, Molaro et al. 2020), especially on small objects with insufficient gravity to retain ejecta from impacts or other high-energy disruption events (Graves et al. 2019). In both engineering and planetary science contexts, real-world fatigue stress conditions are neither uniform in magnitude nor precisely regular in frequency, thus failure by cyclic loading is often conceptualized as cumulative damage (Sandor 1972). Growth of fractures by thermal fatigue occurs in three stages: initiation, stable growth, and unstable growth. The duration of the stable growth phase is described by the Paris Law (Paris and Erdogan 1963, Delbo et al. 2014, Molaro et al. 2017), while unstable growth occurs rapidly just before failure. Crack

initiation by fatigue alone requires microscopic fractures to form at the material surface and coalesce into a single crack 0.1 to 1.0 mm in length (Meyers and Chawla 2010). The initiation phase dominates the total time to failure if no existing cracks or fracture nucleation sites are present (Janssen et al, 2002), while high-amplitude fatigue stress can accelerate initiation causing stable growth to dominate (Meyers and Chawla 2010).

In our experiment we observe the formation and expansion of sub-mm fractures within mineral inclusions, facilitated by thermally driven decomposition reactions and plastic deformation. While the presence of an inclusion is often sufficient to initiate a fatigue crack in the surrounding bulk material (Grosskreutz 1970), we find it notable that the heat delivered by the laser pulse can initiate fractures within inclusions in mere nanoseconds. Furthermore, we directly observe fractures widening and elongating during a single episode of heating by the laser, suggesting repeated heating pulses would propagate these fractures even further. In some locations (e.g. Figure 3.4) we observe these fractures propagating across grain boundaries from one inclusion to another, although we do not observe fractures propagating into the bulk kamacite. Notably, ferrous alloys can exhibit a fatigue stress amplitude threshold, referred to as the endurance limit, which must be exceeded for a fracture to initiate (Meyers & Chawla 2010), though it is unclear whether meteoritic iron is subject to such an endurance limit. Nevertheless, thermally driven breakdown of inclusions within an iron meteorite will be relevant for future studies on iron meteorite fracture mechanics, either by fatigue or shock stress.

3.5. Conclusion:

We performed exploratory laser irradiation experiments simulating rapid heating characteristic of micrometeoroid impacts on four constituent minerals in an iron meteorite sample. All four minerals exhibit thermally driven deformation: bulk plastic deformation in kamacite, fracture extension and plastic deformation constrained by grain boundaries in schreibersite, fracture initiation and delamination due to decomposition in cohenite, and melting and volatilization in troilite. These deformation modes indicate that abrupt, non-cyclic thermal stress from micrometeoroid impacts, or other thermal energy sources can initiate mechanical breakdown within iron meteorite inclusions. Taken as an analog for a metallic asteroid surface, this mechanical breakdown may produce micron-scale fragments contributing to regolith and may also provide nucleating sites for subsequent thermal fatigue or other mechanical stresses to break down the bulk material further. Taken together, these results illustrate some of the novel mechanisms of regolith formation and weathering on metallic asteroid surfaces.

CHAPTER 4: CHARACTERIZING EJECTA FRAGMENTS FROM CRATERING EXPERIMENTS INTO IRON METEORITES

Authors: J. M. Christoph, T. Sharp, S. Marchi, & L. T. Elkins-Tanton.

Abstract:

Impacts are a main regolith-forming process on airless planetary objects explored thus far, and likely also on objects yet to be explored. The bulk material properties of the impacted planetary surface influence the properties of both the resulting crater and impact-driven regolith formation. Metallic planetary surfaces, as hypothesized for asteroid (16) Psyche, present a relatively new domain of impact processes due to their higher strength and differing deformation and fracture modes as compared to stony surfaces. While a metallic regolith is still hypothetical, it is necessary to characterize a laboratory analog in advance of exploring a metal-rich world for the first time. Using Scanning Electron Microscopy (SEM), we imaged ejecta fragments from a previously reported impact gun experiment into an iron meteorite target. By characterizing the ejecta fragments' fracture surfaces, we attempt to constrain the deformation and failure modes occurring during the impact. We find that these ejecta fragments exhibit a wide range of surface morphologies, including rounded, angular, flattened, curved, and cupped, consistent with multiple modes of both brittle and ductile mechanical deformation. We predict that a regolith composed of such metallic ejecta particles may have a higher slope angle of repose compared to silicate regolith due to the hypothetical increased cohesiveness of such irregular particles in a low-gravity environment.

4.1. Background:

4.1.1. Impact-driven regolith formation

Impacts at all sizes are efficient at breaking down the rocks that make up a planetary surface into smaller pieces through shock, compression, and excavation (Shoemaker et al. 1967, Gault 1970, French 1999). The relatively higher rate of smaller impacts over larger ones (Melosh 2011) means that smaller impactors disproportionately contribute to surface breakdown, resulting in regolith formation (Melosh 2011, Hörz and Cintala 1997). At the smallest length scales, microscopic dust impacts contribute specific observable textures including glass and shocked material (Hörz et al. 2020), while also playing a significant role in space weathering (Adams and McCord 1971, Keller and McKay 1997, Sasaki et al. 2001, Loeffler et al. 2008). However, due to the equilibrium resulting from impacts into already-shattered material (Gault 1970, Melosh 2011) macroscopic impacts are still necessary for both the breakdown of larger rocks (Hörz et al. 2020, Cambioni et al. 2021) and "gardening" overturn of broken-down fragments (Hörz 1977). Acting together over geologic time, these processes develop the meters-to-kilometers-thick regolith we observe on the Moon (Shoemaker et al. 1967, Oberbeck and Quaide 1968, Gault et al. 1974, Papike et al. 1982, Wilcox et al. 2005) and the diversity of regoliths found on asteroids (Veverka et al. 2001, Keihm et al. 2011, Tsuchiyama et al. 2011, Walsh et al. 2019, Yokota et al. 2021, Stickle et al. 2023).

The final physical characteristics of mature regolith grains may not resemble the initial ejecta fragments due to space weathering, fatigue, and other processes (Papike et al. 1982, McKay & Ming 1992, Hörz and Cintala 1997). However, the initial breakdown of surface blocks into finer particles is important to consider, as this initial ejecta surface is the starting material that subsequent regolith-maturing processes act on.

4.1.2. Metallic failure modes

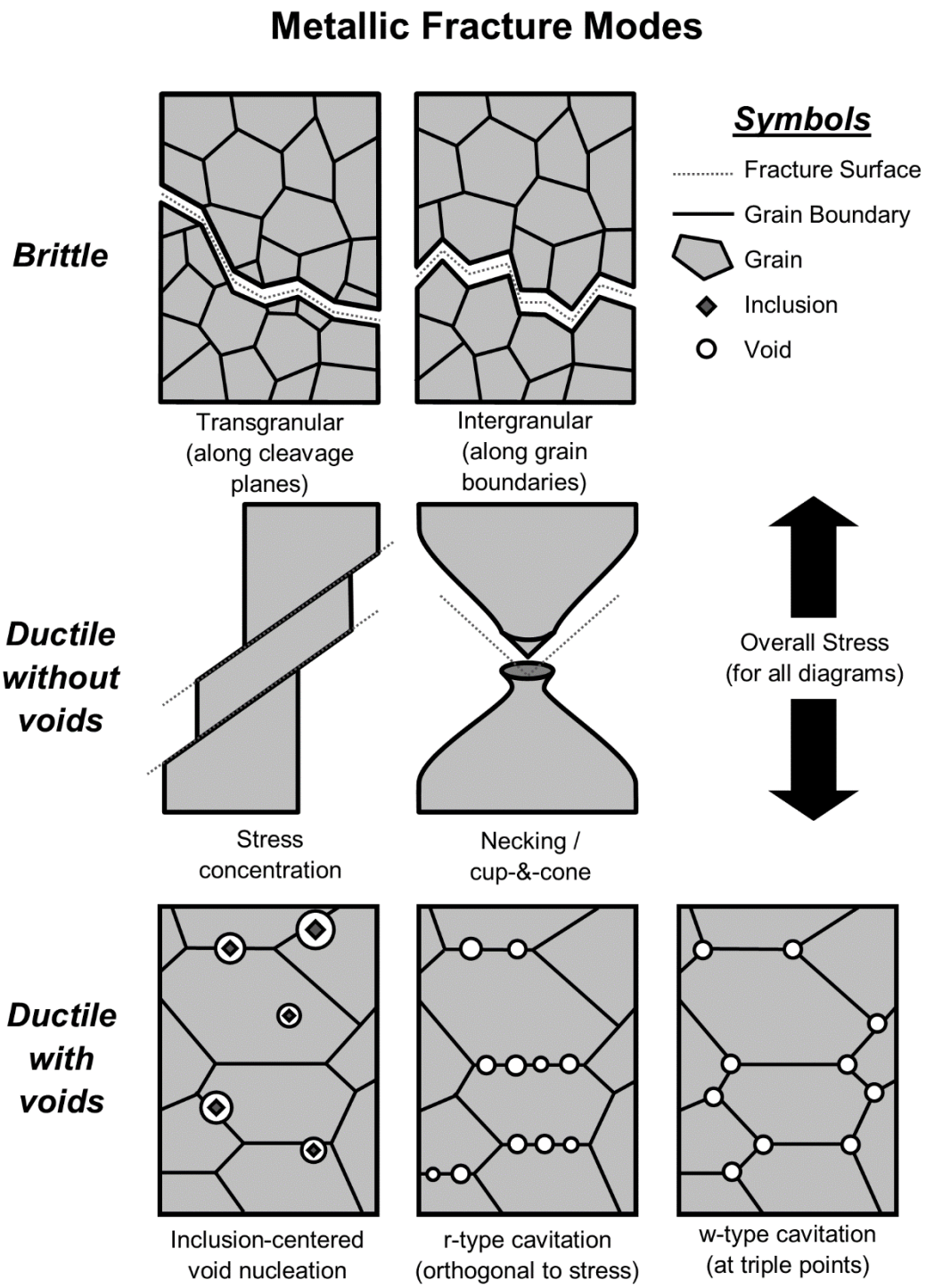

Figure 4.1. Cartoon depictions of fracture modes in metals, modified from Fig. 8.1 in Meyers and Chawla (2014) after Ashby (1999). Each of these failure modes has a

characteristic fracture surface, which can be identified in SEM to determine the mechanical conditions experienced during failure.

While impact mechanics are well-characterized in rocks typical of terrestrial planetary crusts and stony asteroids, metals can exhibit different mechanical behavior. Most rock-forming minerals behave as brittle materials under impact conditions (Petrovic 2001), meaning they tend to undergo only a small amount of elastic deformation before suddenly snapping along grain boundaries or cleavage planes upon reaching their ultimate yield stress (Meyers and Chawla 2014). In contrast, metals more typically behave as ductile materials, experiencing a clear transition from elastic to plastic deformation significantly below their ultimate yield stress, and undergoing a significant amount of deformation before failure (Figure 4.1) (Petrovic 2001, Meyers and Chawla 2014). It is also important to consider that both brittle and ductile failure can be influenced by the presence of inclusions or "impurities," which may be weaker than the bulk material or may nucleate voids by concentrating stress at structural weak points (Meyers and Chawla 2014).

Many metals, including Fe-bearing alloys, can switch to ductile failure when cooled below a certain transition temperature (Petch 1958, Armstrong 1964). However, body-centered cubic (BCC) crystal structures undergo brittle-ductile transition much more readily than face-centered cubic (FCC) crystals, which can remain ductile well below the BCC transition temperature (Cottrell 1958, Remo & Johnson 1974, Lawn & Wilshaw 1975). Meteoritic nickel-iron can contain both BCC and FCC phases, with low-Ni kamacite (α-FeNi, analogous to ferrite) and high-Ni taenite (γ-FeNi, analogous to austenite) forming a multi-component microstructure as the Fe-Ni metal cools, with the

precise mechanism depending on the abundance of both Ni and P due to the uptake of Ni by iron-nickel phosphide inclusions (Buchwald 1975, Yang and Goldstein 2005, Goldstein et al. 2009). It is therefore not necessarily obvious how a given iron meteorite will fracture under impact conditions on an asteroid surface.

4.1.3. Iron meteorite fracture mechanics

Previous studies of the bulk mechanical properties of iron meteorites have been relatively few, but nevertheless instructive. Petrovic (2001) provided the most recent literature review, summarizing previous quantitative bulk strength and ductility measurements of iron meteorites. Iron meteorites are significantly stronger than their stony counterparts in all reported experiments, and ductile-brittle transition behavior has been observed in iron meteorites in several previous experiments (Petrovic 2001). Invar and stainless steel, close chemical analogs for iron meteorites, are less useful mechanical analogs since iron meteorites have orders-of-magnitude larger grain sizes and microstructures than human-made alloys, having cooled over geologic time (Petrovic 2001).

A specific focus on iron meteorite fragmentation mechanics began in the 1970s. Gordon (1970) performed tensile failure experiments on samples of the Gibeon iron meteorite, a fine octahedrite with 7.9 wt.% Ni (Buchwald 1975), finding that neither nonmetallic inclusions nor cooling to 150 K significantly embrittled the Gibeon metal. Auten (1973) subsequently performed similar tensile failure experiments on Gibeon metal and observed a brittle-ductile transition below 150 K. Remo and Johnson (1974) re-assessed the results of both Gordon (1970) and Auten (1973), noting that while tensile tests simulate uniaxial loading, an impact would produce triaxial loading, raising the

brittle-ductile transition temperature from 50 K under Gordon's (1970) experimental conditions to 200 K. Subsequently, Remo and Johnson (1975) performed Charpy Impact experiments – an ASTM standard fracture test in which a sample with a notch on one side is impacted on the opposite side by a falling pendulum (Meyers and Chawla 2014) – on samples of the Henbury iron meteorite, a medium octahedrite with 7.1 wt.% Ni (Buchwald 1975), confirming a brittle-ductile transition at 195 K.

Additionally, Remo and Johnson (1974) noted the lack of a brittle-ductile transition in FCC alloys (Cottrell 1958), hypothesizing that the degree of ductile deformation in an iron meteorite would decrease in samples with more abundant taenite, the Ni-rich FCC phase, and thus with increasing bulk Ni content of the parent body. Subsequently, Johnson et al. (1979) performed Charpy impact experiments on samples of the Hoba iron meteorite, an ataxite with 16.4 wt.% Ni (Buchwald 1975), and imaged the resulting fracture surfaces with backscatter SEM. Specimens impacted at 195 K were ductile in the Charpy test, with fracture surfaces dominated by void-initiated ductile fracture. Specimens impacted at 77 K were brittle in the Charpy test, with fracture surfaces displaying a combination of void-induced failure and cleavage. Johnson et al. (1979) thus concluded that increased Ni content lowers the brittle-ductile transition temperature of iron meteorites and hypothesized that it would be lower than the present surface temperatures of Ni-rich iron meteorite parent asteroids.

One challenge when interpreting these experimental results is the choice of samples: the Widmanstätten microstructures of Gibeon and Henbury are less than 1 mm thick, and that of Hoba is microscopic (Buchwald 1975). The kamacite and taenite grains Gibeon, Henbury, and Hoba are therefore significantly smaller than the length scale of

the fractures produced by either a tensile failure test or a Charpy impact test, making it difficult to distinguish the brittle-ductile behavior of individual mineral phases from that of the iron meteorite bulk. Subsequent advances in metallurgical characterization enabled Ueki et al. (2021) to perform tensile failure tests on microscopic samples milled by ion beam etching from individual kamacite and taenite grains in Gibeon. Ueki et al. (2021) found the taenite grains to have 3 times higher yield strength and 3.5 times higher elongation-to-failure (a proxy of ductility) than the kamacite grains, suggesting that this increase in strength may result from either the higher Ni abundance of the taenite or solid-solution-strengthening by minor or trace elements present in the metal.

To summarize, meteoritic iron is significantly mechanically stronger than the stony minerals that make up previously explored planetary surfaces, as well as the nonmetallic inclusions contained within iron meteorites. Meteoritic iron undergoes a brittle-ductile transition below 200 K, with the exact transition temperature depending on the Ni content of the metal and corresponding abundance of taenite grains. We expect these properties to strongly control the size, quantity, and morphology of ejecta fragments produced by impacts into metallic asteroid surfaces, and in turn the properties of an impact-generated metallic regolith. However, it is difficult to predict *a priori* how the mechanical properties of an iron meteorite influence its behavior during impact and the physical properties of the resulting ejecta, thus necessitating experimental testing.

4.1.4. This study

The goal of this work was to learn more specifically what mechanics occur in an iron meteorite when it is impacted, and to characterize the ejecta produced. We investigated this by imaging ejecta fragments produced by aluminum pellets from a

hypervelocity impact gun into an iron meteorite target using scanning electron microscopy (SEM), subsequently assessing whether their fracture surface morphology is consistent with brittle or ductile failure mechanisms. Under brittle failure, we would expect planar or jagged surfaces consistent with cleavage or transgranular fracture. Under ductile failure, plastic deformation would result in curved surfaces that diverge from or obscure the pre-impact microstructure.

4.2. Methods:

4.2.1. Samples

Details of the impact experiment that produced the fragments we characterized can be found in (Marchi et al. 2020), and we summarize them here. Marchi et al. (2020) performed a battery of impact experiments into multiple iron meteorite and FeNi ingot targets in vacuum using the NASA Ames Vertical Gun Range. Here we examine ejecta from shot #3.09, the target material for which is a block of Santiago Papasquiero (ASU#721), an ungrouped iron meteorite with an interlocking equiaxial structure consisting of ~0.1 mm polygonal grains of kamacite with interstitial ~0.01 mm grains of taenite and tetrataenite. This is an unusual structure among iron meteorites and has been interpreted to suggest recrystallization of the meteorite after initial formation of its parent body (Buchwald 1975), but it presents a grain geometry that can be easily distinguished in electron microscope imaging if and where the structure is preserved after impact. A 4 cm cube of Santiago Papasquiero cooled to 129 K was impacted with a 6.350 mm diameter spherical aluminum projectile at 5.31 km/s and normal incidence, a velocity comparable to the 5.81 +/- 1.11 km/s impact velocities in the Main Belt (Farinella and Davis 1992). The resulting impact crater (Figure 4.2**)** is 21.5 mm in diameter by 7.6 mm

in depth. The interior of the crater is covered in structures resembling thin, concave petals, rising to an overhanging flap projecting several mm above and radially out from the crater rim (Marchi et al 2020). Numerous fractures are visible radiating out from the crater across the bulk surface of the impact target and extending internally as revealed by x-ray tomography, described by Alexander et al. (2022). Ejecta fragments were recovered by sweeping the impact chamber with a brush, followed by magnetic separation from any nonmetallic particles left within the chamber from previous experiments.

Figure 4.2. The crater in the center of the target block after impact. Petal-like structures cover the crater floor and extend into the raised, cantilevered rim flap. A set of fractures radiates out from the crater, in some places (e.g. the rear edge of the block) producing spallation fragments.

4.2.2. Microscopy

All the fragments are mounted on a one-inch SEM slide with a carbon tape round, except the largest (>5 mm) piece which is mounted separately to avoid beam shadowing effects while imaging the smaller fragments (Figure 4.3). Even though the metal fragments are conductive, we applied a carbon coating to minimize localized charging at

rough points on the fragment surfaces and maximize electrical contact with the flat tape surface. We imaged the fragments with two Field-Emission Scanning Electron Microscopes (FE-SEM) at the Eyring Materials Center at Arizona State University: initially an FEI XL30 and subsequently a Thermo Scientific Helios 5 UX which replaced it. We obtained mosaics of overlapping secondary and backscatter electron images at 200x magnification covering the entire slide, as well as higher resolution images up to 15,000x magnification of representative fragments and features. We used secondary electron imaging to characterize fragment surface morphology, as well as backscatter electron imaging to clearly identify fracture surfaces. Subsequently, we used energy-dispersive X-ray spectroscopy (EDS) to assess the elemental composition of certain contrast features within the backscatter electron images. Our goal was to capture features within the visible fracture surfaces on each fragment that could potentially indicate the mode of strain, deformation, and failure that occurred during impact. While we cannot necessarily quantify the relative contribution of each mode to the whole population of ejecta, we can gain an overall sense of the various ways the impact broke down the target material.

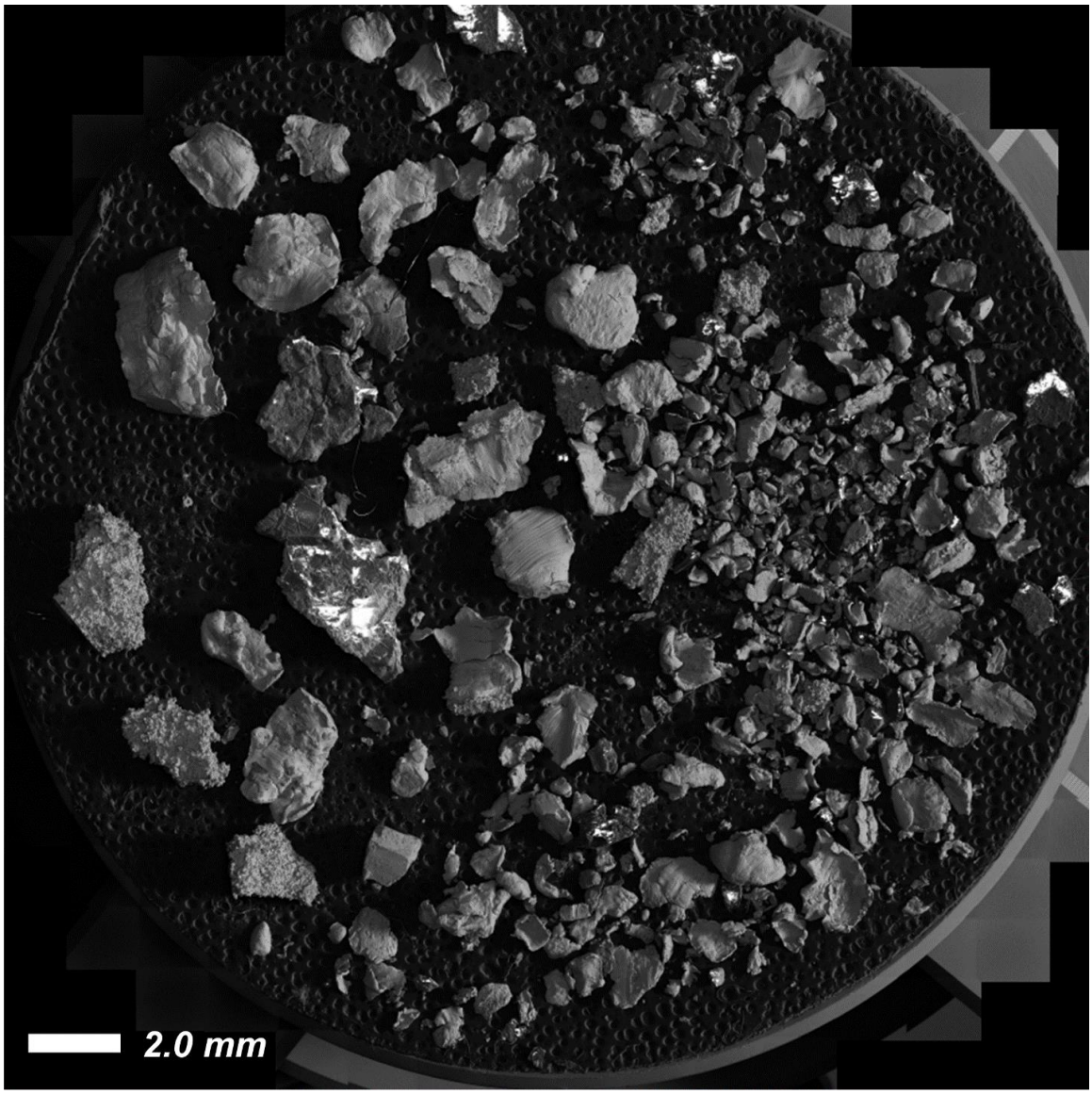

Figure 4.3. Backscatter electron image mosaic of 291 ejecta fragments mounted on a 1-inch slide (all but the largest piece). The individual images are backscatter electron at 200x magnification and 30 kV beam potential.

4.3. Results:

4.3.1 Survey of the ejecta fragments

We recovered 292 fragments, with a total mass of 0.75 g. The largest single fragment is 10 mm long, >5 mm in all dimensions, and has a mass of 0.45 g. The remaining fragments include 75 between 5.0 and 1.0 mm, 210 between 1.0 and 0.25 mm,

and the remainder <0.25 mm (Figure 4.4). Intriguingly, these fragments are approximately an order of magnitude larger than those produced by impacts into stony targets at similar velocities (Durda and Flynn 1999). However, this size distribution may not be a representative sample of all ejecta produced by an impact onto a meteoric iron target, since the collection method may not have captured all of the smallest metal particles produced. We can at least observe that an impact into Santiago Papasquiero is effective at producing ejecta fragments in the mm-to-sub-mm size range, which is consistent with inferences of regolith grain size from observations of (16) Psyche's thermal inertia (Landsman et al. 2018, de Kleer et al. 2021).

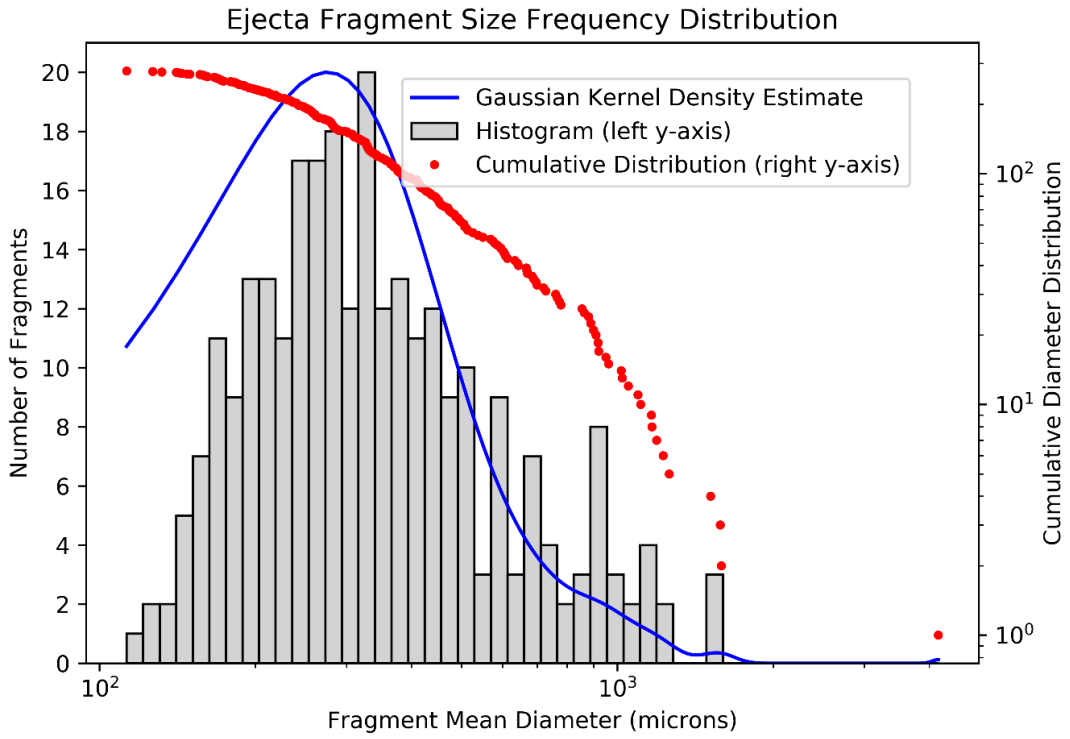

Figure 4.4. Size-frequency distribution of the ejecta fragments, plotted as a histogram (gray bars), Gaussian Kernel Density Estimate (blue curve) and Cumulative Distribution (red scatter plot).

The 291 fragments mounted on the same SEM slide are shown in Figure 4.3. Before taking this mosaic image, we first surveyed a few of the larger fragments to identify any challenges for high-resolution imaging of the entire slide. On a few fragments at relatively low electron beam potential (<10 kV), backscatter images show alternating dark and light regions (Figure 4.5a), which indicate compositional variation due to either different densities or atomic numbers. EDS point spectra show that the brighter backscatter region is composed of Fe and Ni in typical ratios for meteoritic iron (Figure 4.5b), while the darker backscatter region includes a significant amount of Al (Figure 4.5c). Fe and Al do not typically mix in iron meteorites (or elsewhere), as alloying because the two elements do not readily metallically bond with one another. Instead, the Al is residue from the impactor, deposited in a thin layer on top of FeNi bulk. Since the volume of the impactor is only a tiny fraction of the crater volume, we did not expect this layer to be more than a few microns thick. Imaging the sample at increasing electron beam potential (up to the Helios's maximum of 30 kV) extended the backscatter information volume fully into the Fe bulk beneath the micron-thickness Al layer, at which point the backscatter contrast feature to is no longer visible. We are thus confident that backscatter electron imaging at 30 kV captures the topography of this buried Fe surface rather than the Al coating on the few large particles where this backscatter contrast feature is visible.

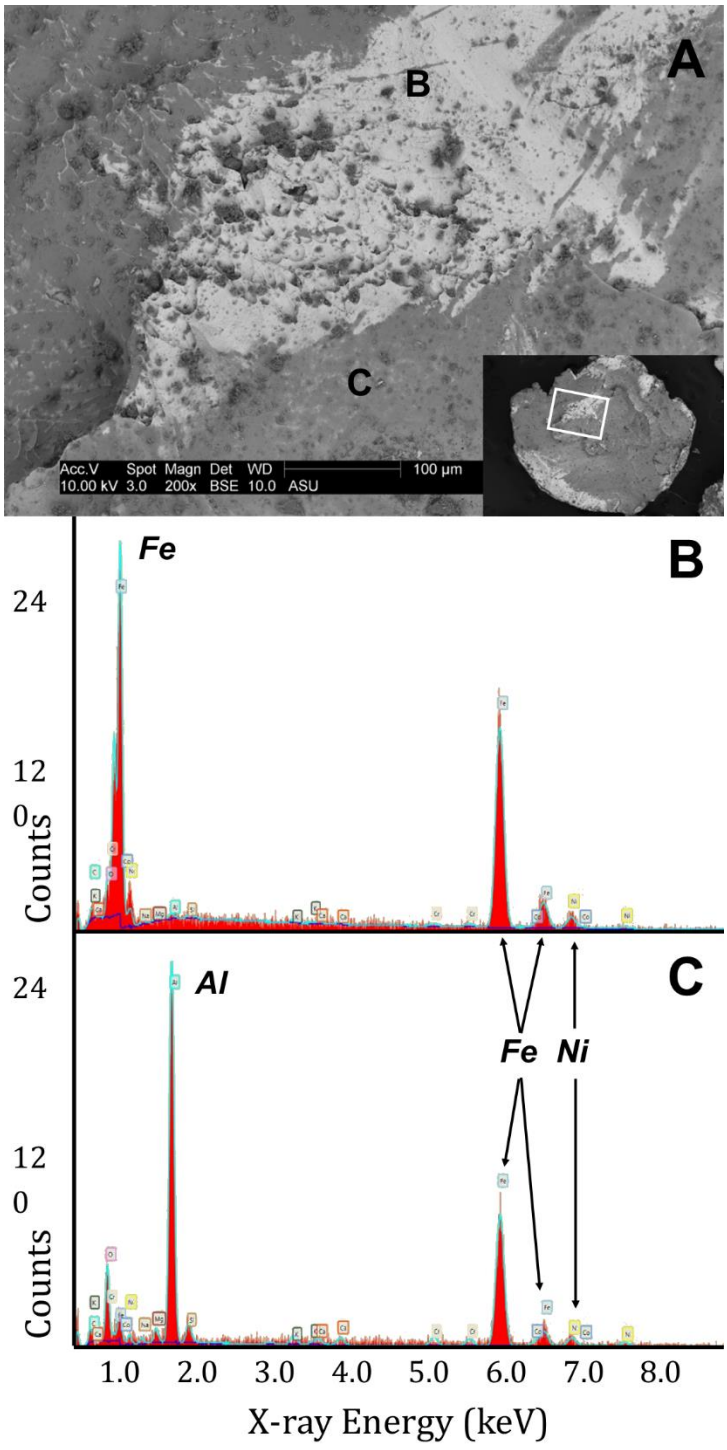

Figure 4.5. Backscatter contrast on the exposed faces of some fragments imaged at 2-5 kV indicates compositional heterogeneity (A). EDX spectra show that the higher-contrast (brighter) material (B) is the iron-nickel alloy of the target meteorite, while the lower-contrast (darker) material (C) contains aluminum from the impactor. The presence of Fe and Ni x-rays in the darker region indicates the Al is a surficial layer, and at high electron beam potential we are able to image the underlying FeNi fracture surface.

4.3.2 Fragment morphology types

Among the fragments in the Figure 4.4 mosaic image, we were able to identify six broad types of distinctive identifying features listed in Table 4.1. Many fragments exhibited multiple feature types, so the sum of values in the last column exceeds the total number of fragments. We describe each fragment type in more detail below.

Table 4.1.

TYPE	IMAGE	MORPHOLOGICAL INTERPRETATION	COUNT
Petals	Figure 4.6	Possibly related to crater rim/floor flaps	85
Radial Lineation	Figure 4.7	Shock wave interaction with internal interfaces	13
Preserved Grains	Figure 4.8	Intergranular brittle fracture	31
Plastic (micro)	Figure 4.8	Ductile deformation due to stress concentration	86
Plastic (macro)	Figure 4.9	Ductile deformation across whole fragment	121
Ungrouped/error	N/A	Non-metallic or non-conductive fragments	12

The first type of feature we observe is distinctive enough that it was identified by Marchi et al. (2020) with preliminary low-magnification optical microscopy. These fragments exhibit a petal-like morphology, visually similar to the overhanging flap projecting out from the crater rim or the smaller flaps within the crater bowl. The largest example of this type is shown in Figure 4.6, however the exact shapes and sizes of these fragments vary from mm-scale pieces containing multiple attached curved petals to open hemispherical or cup-shaped pieces tens of microns in diameter. 85 fragments are of this type, approximately 34% of the total number.

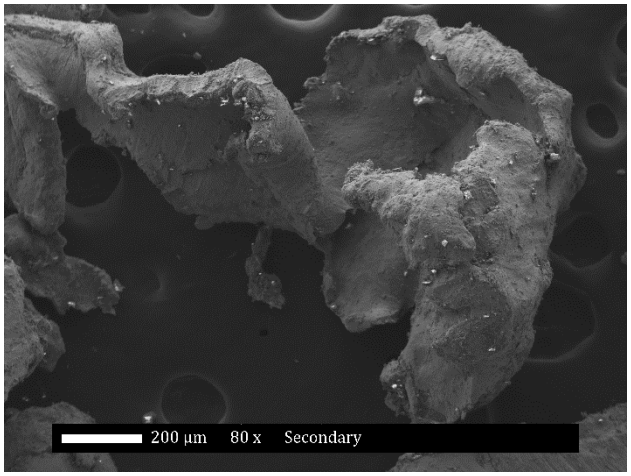

Figure 4.6. A petal-like fragment, defined by a thin, irregular, concave surface, visually similar to the petal structures in the impact crater floor and rim.

Other feature types were not specifically described in Marchi et al. (2020) and are difficult to resolve with the optical microscopy technique used by Marchi's team. The first such type is defined by lineations radiating in a conical or branching pattern from a single point on one side of the fragment (Figure 4.7). Only 13 such fragments exist, the smallest grouping among fragments that can definitively be shown to originate from the Santiago Papasquiero target.

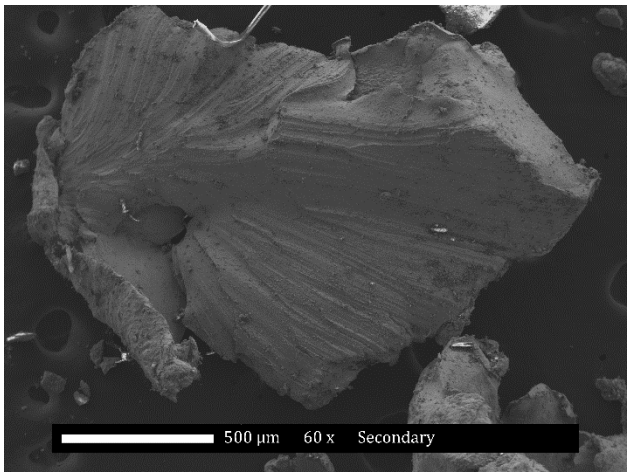

Figure 4.7. A branching fragment, defined by lineations radiating in a conical or branching pattern from a single point at the fragment edge.

Some of the fragments appear to preserve the pre-impact microstructure of Santiago Papasquiero: interlocking polygonal grains of kamacite with interstitial taenite (Figure 4.8). The exposed fracture surfaces on these fragments run directly along grain boundaries, and in some cases further intergranular fractures run deeper into the fragment but not all the way through. The largest fragment is one such piece, along with 30 other smaller pieces (31 total). However, imaging these fragments at higher magnification reveals that not all the individual grains are preserved intact. The smallest features of Santiago Papasquiero's microstructure are the 10-μm interstitial taenite grains, all of which exhibit significant plastic deformation, and some of which straddle fractures between adjacent larger grains. Additionally, some of the larger grains protruding from the fracture surface exhibit similar plastic deformation, with non-planar faces and elongated tips, while directly adjacent and contacting grains appear unmodified. A total of 86 fragments include this feature: all of the 31 fragments with preserved grains include some of these plastically-deformed grains, plus 55 more which either do not exhibit any preserved grains or which are smaller than a single 100-μm grain of the pre-impact meteorite.

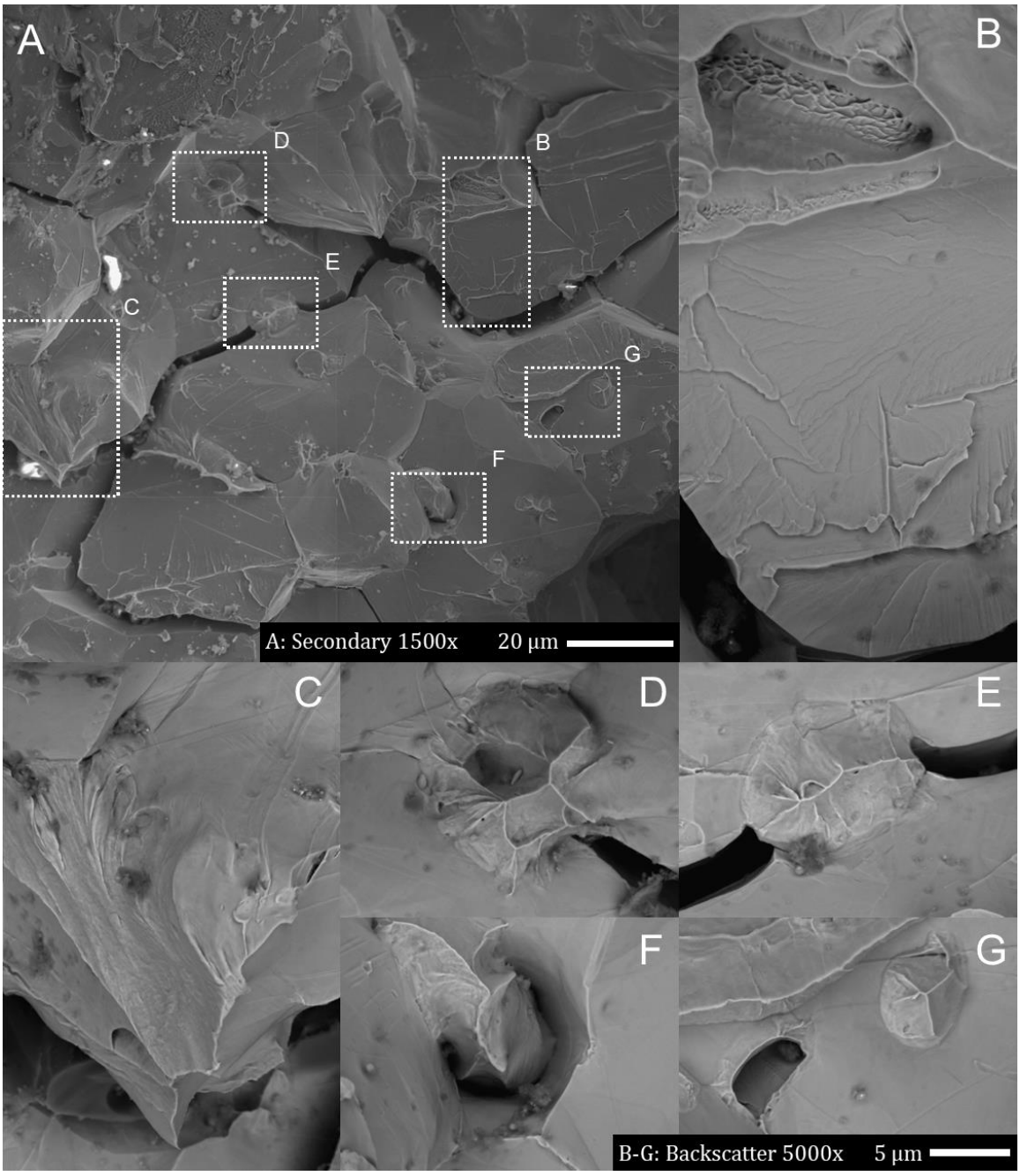

Figure 4.8. *(A) A portion of the largest (>5 mm diameter) fragment, showing interlocking 20-µm grains closely resembling the pre-impact microstructure of the Santiago Papasquiero meteorite, with intergranular fractures. (B) The exposed face of a kamacite grain displaying a planar surface with rough edges, bordered at the top by a heavily plastically deformed region. (C) Plastically deformed tip of a protruding kamacite grain, adjacent to unmodified grains with planar faces. (D-G) Heavily deformed 5-µm interstitial taenite grains at boundaries between larger kamacite grains which are significantly less deformed.*

The largest group of fragments exhibits plastic deformation larger than the 20-micron grain size of the pre-impact meteorite. A variety of textures is included in this type. Most of these fragments are smooth, rounded, and appear compositionally homogeneous (Figure 4.9A, D). Some exhibit curved “lips” or “rims” folded back over the fragment edge (Figure 4.9C), superficially similar to the “petal” type described above but smaller and not comprising the entire fragment. On other fragments we observe surfaces covered in “peaks” spaced a few ~10s of μm apart from one another across a wide area of the fragment surface (Figure 4.9B). These peaks superficially resemble the plastically elongated tips of the grains in Figure 4.8C above but with no visible grain boundary surfaces or other evidence of the pre-impact microstructure. We group all these various features into a single type with 121 members, defined by plastic deformation greater than 20 microns in length scale.

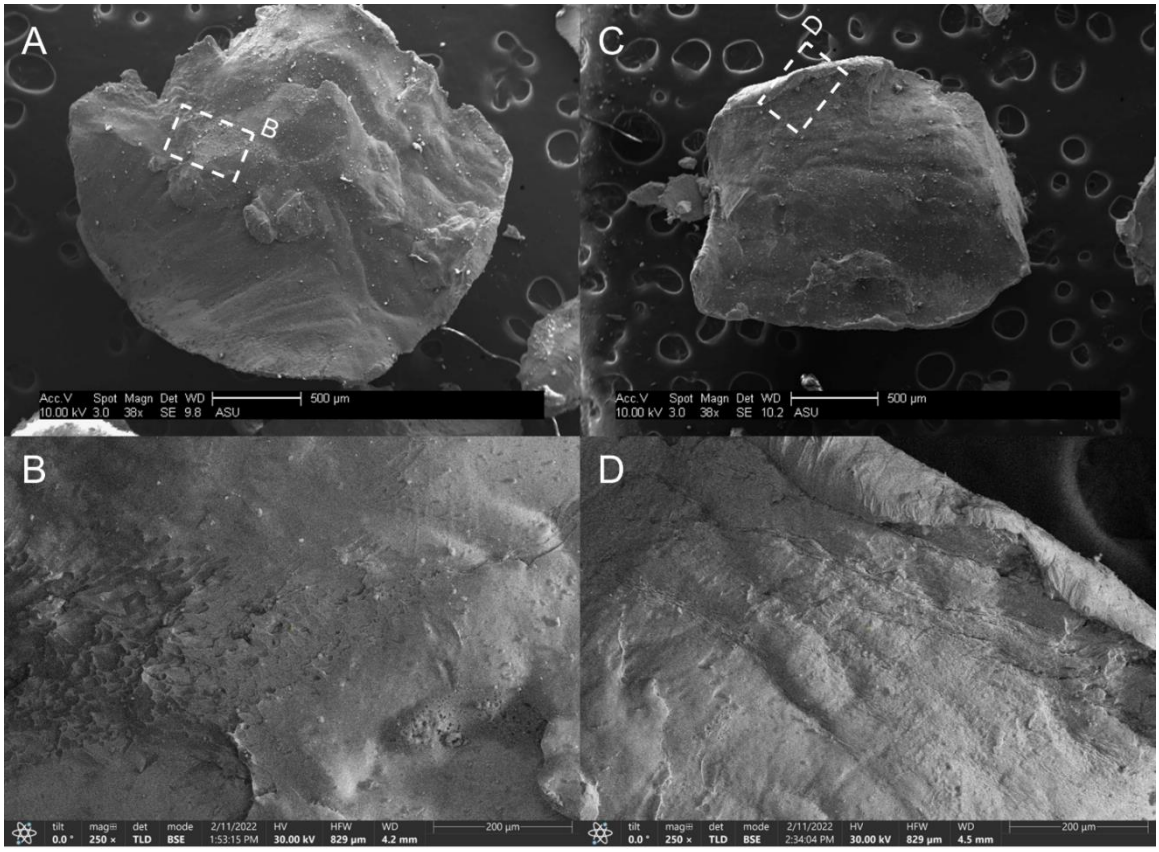

Figure 4.9. Two fragments (A, C) exhibiting plastic deformation larger than the Santiago Papasquiero grain size. Higher-magnification detail images of each fragment show a series of sharp peaks on the face of one fragment (B), and a raised lip curving around the edge of the other fragment (D).

The final fragment type includes those which are not definitively metallic, either due to lower backscatter coefficient or persistent charging even after carbon coating, implying low electrical conductivity; only twelve exist, and they are discounted from our analysis.

4.4. Discussion:

4.4.1. Interpretation of each fragment type.

The petal fragments are the most difficult to interpret. Their superficial morphological similarity to the overhanging rim flap and crater floor petals suggests a common origin, as suggested by Marchi et al. (2020). We have no way of assessing

whether this similarity indicates a shared formation mechanism, and the formation of the overhanging rim flap and crater floor petals is itself mysterious. It is unlikely that the petal fragments may have been molten when ejected and subsequently solidified, since (Alexander et al. 2022) found that the target block likely was not heated sufficiently for any portion of its mass to melt. Alternately, the petal fragments and rim flaps might both be related to the conical curtain of material ejected early in the impact process, which also forms during impacts into stony targets but almost immediately separates from the surface instead of remaining attached (Melosh 2011). In any case, the petal fragments are a product of extreme plastic deformation of the target metal.

The radial linear morphology superficially resembles shatter cones, a shock product found in stony terrestrial impact sites. The precise mechanism of shatter cone formation has been uncertain for some time; proposed mechanisms have included: the main compressive shock wave scattering off inclusion interfaces (Johnson and Talbot 1964), superposition of internally reflected tensile stresses on top of the compressive shock wave (Gash 1971), constructive interference between tensional hoop stresses at the shock tail and internally scattered tensional stresses (Baratoux and Melosh 2003), and interactions between the fracture front wave and heterogeneities in the rock substrate (Sagy et al. 2004). Beyond the apparent visual similarity and the presence of shock waves during the impact test, we lack direct evidence that the structure of the radial linear fragments is related to any proposed shatter cone formation mechanism. However, interactions between the impact shock wave and internal interfaces of the meteorite's microstructure are likely to have occurred, whether these radial linear fragments are the product of such interactions or not.

Some of these fragments exhibit preserved pre-impact microstructure, including the largest piece, which includes portions of the flat outside face of the target block. The fracture surfaces of these fragments match the internal texture of the fractures on the post-impact block (Figure 4.2). We therefore interpret these fragments as pieces spalled out from these radial fractures, rather than from the interior of the crater. If this interpretation is correct, it would be important for understanding metallic regolith formation, as it would support the hypotheses that material from outside the crater can contribute to ejecta, and that metallic block the size of the impact target can be broken down into smaller pieces by crater-induced fracture, as observed on non-metallic asteroids (Cambioni et al. 2021, Ballouz et al. 2023).

The preservation of the pre-impact grain structure indicates intergranular fracture, which in metals is typically a brittle deformation mode (Figure 4.1). Intergranular fracture in metals predominates when the boundaries between metal grains are weaker than the crystal lattice of the grains themselves (Meyers and Chawla 2014). Industrial metals typically experience transgranular fracture below the brittle-ductile transition temperature, propagating along internal cleavage planes from grain to grain (Broek 1982). Moreover, Johnson et al. (1979) observed cleavage surfaces in samples of Hoba fractured at 77 K. However, one would expect the 20-micron-long grain boundaries in Santiago Papasquiero to be weaker than the much smaller grain boundaries in either an industrial metal or an ataxite, since strength tends to increase with decreased grain size in metals according to the Hall-Petch relationship (Hall 1951, Petch 1953, Meyers and Chawla 2014). Therefore, transgranular fracture or cleavage is less likely than intergranular fracture, and in any case we do not observe surfaces on our fragment grains

that can be easily distinguished as cleavage planes rather than the planar grain boundaries present in unmodified Santiago Papasquiero.

The brittle intergranular fracture hypothesis is complicated by the ubiquitous individual plastically deformed grains present even in fragments with little visible deformation larger than the 20-μm pre-impact grain size of Santiago Papasquiero. Some amount of ductile deformation occurred on these fragments during failure, but the precise mechanism requires interpretation. We can rule out the most typical mode of ductile failure in metals, cup-and-cone fracture (Meyers and Chawla 2014), which only occurs under uniaxial tensile stress which is not characteristic of impacts (Remo and Johnson 1974). We can also rule out w-type cavitation, which occurs as slip along grain boundaries concentrates stress at intergranular triple points to form cavities (Meyers and Chawla 2014), because it requires higher temperatures over a longer duration than would be consistent with this impact experiment (Alexander et al. 2022). A more precise mechanism of ductile deformation must be invoked.

The presence of plastically deformed grains adjacent to apparently unmodified grains is most consistent with strain concentration by compositional or orientational differences between adjacent grains, a process observed in shocked meteorites (Moreau et al. 2018). While the kamacite and taenite grains are similar compositionally, grain orientation differences alone can be enough to form intergranular voids, both under low-strain-rate conditions such as r-type cavitation (Meyers and Chawla 2014), and under high-strain-rate conditions such as shock (Moreau et al. 2018). The presence of highly deformed taenite grains straddling intergranular fractures (Figure 4.8E) is also consistent with inclusion-centered void nucleation (Figure 4.1) (Lawn and Wilshaw 1975):

intergranular fractures may nucleate by ductile deformation of the interstitial taenite grains, becoming more brittle as they propagate between kamacite grains.

Additionally, we must consider that while BCC grains undergo brittle-ductile transition, FCC grains do not (Cottrell 1958, Remo and Johnson 1974). Even at the 129 K temperature of the target before the impact test, the entire block would not have transitioned to the brittle regime, and the target would have been heated above that initial temperature during the impact (Alexander et al. 2022). We would expect the BCC kamacite grains to undergo brittle deformation, while the FCC taenite and tetrataenite grains would remain in the ductile regime. This difference in behavior would be pronounced in our sample of Santiago Papasquiero as compared to previous experiments (Johnson et al. 1979, Petrovic 2001) because brittle-ductile transition temperatures can be elevated with larger grain sizes (Armstrong 1964, Qiu et al. 2014). Thus, while brittle intergranular failure and plastic deformation are ordinarily competing mechanisms in metals (Armstrong 1964), the presence of adjacent grains with different preferred deformation modes raises the possibility of fractures propagating by brittle and ductile deformation simultaneously in different regions of a meteorite's highly heterogeneous microstructure.

The fragments which lack any evidence of pre-impact microstructure are enigmatic, however they are all inconsistent with brittle failure and so, in one way or another, they all point to ductile deformation with a contribution from impact-generated heat. Post-impact simulations indicate the target block experiences little to no melting during impact (Alexander et al. 2022), and so we assume most of these fragments merely experienced a high degree of ductile deformation. The peaks observed on Figure 4.9B

clearly point to ductile failure across a large surface area comprising multiple grains, requiring the entire fragment be above the brittle-ductile transition temperature, though the exact temperature these fragments would have to reach is unclear. The “lips” and “rims” around the edges of some fragments (Figure 4.9C) suggest there may be some commonality of deformation mode and stress conditions with the petal-type fragments, but this is speculative.

The range of deformation modes observed – complete melting through varying degrees of ductile deformation to brittle deformation and shock – indicates that strain, strain rate, and temperature were likely all heterogeneous throughout the target during impact. The most common morphology by number of fragments is bulk plastic deformation, followed by approximately equal numbers of petals and grain-scale plastic deformation. The likely mechanisms associated with each of these fragment types require different pressure and temperature conditions, providing further evidence that different fragment types originate from multiple locations within and around the impact structure.

4.4.2. Properties of resulting regolith

Metallic regolith is possible, thanks to the diverse array of ejecta particle sizes and morphologies formed by impacts into metal. The mm-to-sub-mm fragments resulting from this experiment are at the high end of the metallic clast size range predicted by de Kleer et al. (2021), and subsequent breakdown into smaller fragments by gardening is possible. All these particles are significantly smaller than the meter-scale spatial resolution of the Psyche Multispectral Imager, so direct observations of a metallic regolith will require measuring and modeling the photometric properties of such metallic particles.

A regolith resulting from impacts analogous to this experiment could include a mix of angular clasts formed by spallation from fractures around the crater, rounded clasts formed by plastic deformation of material excavated from within the crater, and petal-like fragments possibly related to the crater bowl and rim. Impact experiments into silicate targets can also produce plate-like and needle-like ejecta fragments (Michikami et al. 2016), in contrast to the metal fragments which include curved and cup-like textures. We hypothesize that the presence of both the angular clasts and the petal-like pieces might result in a more cohesive regolith as compared with silicate regolith, resulting in higher angle-of-repose slopes and less susceptibility to mass wasting at lower slopes (Jaumann et al. 2022). To quantify the sedimentary behavior and resulting geomorphology of a regolith with these particle morphologies, we recommend researchers with appropriate apparatus perform lab experiments on metallic sedimentary analogs with similar morphologies, simulating slope formation, vibrational settling, mass wasting, impacts, cyclic heating and cooling, and other airless body surface processes.

4.5. Conclusion:

Using SEM, we have characterized the ejecta fragments produced by an impact gun experiment into an iron meteorite target. The size distribution of these ejecta fragments is consistent with that inferred for metallic particles in the regolith of asteroid (16) Psyche based on millimeter-wave observations. The surface morphologies of these ejecta fragments are diverse, indicating a variety of fracture modes in both brittle and ductile mechanical regimes. Consistent with previous work on the mechanics of meteoritic metal (Johnson et al. 1975, Petrovic 2001, Moreau et al. 2018, Ueki et al. 2021), we find that nickel content, taenite grain abundance, crystallographic orientation,

grain boundary geometry, presence of inclusions, and position relative to the crater all influence the localized stress conditions experienced by any given piece of material ejected during impact. We therefore predict that an impact-generated metallic regolith would comprise a heterogenous mixture of ejecta fragment sizes and morphologies: angular, rounded, and flat pieces from mm-scale to microscopic. The optical and geomorphological properties of such a metallic regolith warrant further investigation, however we can predict such a heterogeneous regolith would be relatively cohesive and maintain steep slopes as compared to silicate regolith.

CHAPTER 5: SYNTHESIS AND FUTURE WORK

5.1. Connections between the processes studied in each experiment.

We have focused on three surface processes which independently yet simultaneously modify asteroids' physical properties. The thermal energy from micrometeoroid impacts both promotes diffusion of atoms in the bulk material toward the surface (Loeffler 2008) and controls the depth profile of ions implanted into the irradiated surface as shown in Chapter 2 (Christoph et al 2022). Thermal energy also drives mechanical expansion and contraction that can initiate fractures as shown in Chapter 3, as well as propagating those fractures through subsequent episodes of thermal stress, as in thermal fatigue (Molaro et al. 2012, 2017, 2020). Finally, the thermal state of the surface plays a role in determining the mode of failure of a metallic block during impact, whether it is driven by brittle or ductile deformation, as discussed in Chapter 4.

Beyond the multiple mechanisms and scales by which thermal energy modifies an airless body surface that we have observed in our experiments, we hypothesize that other sources of energy may also drive airless body surface modification via multiple mechanisms. Ion irradiation in particular can both modify the surface chemistry as observed in Chapter 2 and may also alter the mechanical properties of a metallic surface through such mechanisms as hydrogen embrittlement (Martin et al 2018) that do not occur in stony minerals and would be unique to metals. Evaluating the effects and extent of such processes will require additional future experimentation, as we discuss later.

5.2. Predictions for (16) Psyche.

Metallic regolith is possible and has multiple plausible formation mechanisms. The impact gun experiments described in Marchi et al. (2020) indicate that relatively

small impactors are effective at breaking down 10-cm-scale metallic blocks (i.e. boulders or cobbles) into smaller fragments at millimeter and submillimeter scales. Laser irradiation experiments show that micrometeoroid impacts can break down cm-scale or mm-scale fragments to even smaller sizes, approximately the finest scale regolith observed an asteroid (Massironi et al. 2012). Even if these micron-scale fragments are not produced as efficiently on Psyche as in our experiments, the cm-scale and mm-scale fragments would be similar to regoliths with larger grain sizes on other asteroids, for example the near-Earth asteroids Bennu and Ryugu (Molaro et al. 2020). We can therefore predict that Psyche's surface will have regolith particles that are approximately in the size range observed on other asteroid surfaces but composed of metal (likely mixed with silicates or other materials).

Based on the experimental results from our laser irradiation and impact ejecta characterization, we can expect metallic regolith particles to have a wide range of morphologies. In addition to the petal-like rim flap fragments that Marchi et al. (2020) observed and which we have further characterized, we can expect a variety of brecciated pieces including crack spallation fragments originating outside craters, melted and recrystallized tektites, particles that experienced a high degree of thermally driven plastic deformation, and the delaminated or exfoliated fragments observed in laser irradiation experiments described in Chapter 3. The grain size and microstructure of the impacted or irradiated surface will play a major role in determining how that material breaks down, for example whether multi-mineral or single-crystal regolith grains would be preferentially produced. As discussed in Chapter 4, the concave morphology of metallic fragments produced by multiple mechanisms may increase the cohesive properties of a

metal-rich sediment, resulting in higher angle of repose slopes as compared to stony asteroid surfaces.

An intriguing likelihood is that metal particles like those produced in our experiments may be mixed with silicates and/or other minerals on Psyche's surface. Recent observations of Psyche indicate a surface composed of mixed metal and silicates, with impactors providing one possible source for the silicate component (Takir et al. 2017, de Kleer et al. 2021). The presence of surficial Al on some ejecta fragments in Chapter 4 demonstrates that material from both impactor & target can be incorporated into metallic regolith fragments, although Al metal is an unlikely analog material for real impactors in the asteroid belt. It will therefore be useful to look for evidence of impactor material incorporated into ejecta fragments from impact experiments using a silicate projectile. Any silicate or rocky component on Psyche's surface will presumably form a regolith according to familiar mechanisms, as on the Moon and stony asteroids.

A challenge that remains in linking the results described in this dissertation to predicted observations for the Psyche mission is that the phenomena that we can observe in laboratory experiments may not be easily detectable by the Psyche mission's instruments. As discussed in Chapter 2, the Psyche Multispectral Imager (a visible and near-infrared imaging system) will have a pixel scale of order meters to tens of meters in the closest planned orbit around asteroid Psyche's surface. The Gamma Ray and Neutron Spectrometer meanwhile has a 10-50 km radius footprint and sensitivity depth of 10 cm or greater in the likely Psyche surface materials that might be compositionally modified by space weathering. It will be difficult to constrain the extent of a given unit solely looking at the bulk composition as measured by the GRNS, or to observe the fine scale

features typical of regolith with particle sizes smaller than boulders. Addressing these limitations will require multiple lines of future investigation: multicomponent compositional mixing models which include the extent of space weathering as a free parameter, and photometric and/or polarimetric experiments and modeling to quantify the optical reflective behavior of metal-rich asteroid surfaces.

A key question unresolved by the ion irradiation experiments in Chapter 2 is, where does the sulfur go? The sulfur atoms preferentially sputtered away from a sulfide surface unit could either escape into space or settle back onto the surface. Ejection of sulfur atoms at greater than escape velocity would over time decrease the relative abundance of sulfur on the surface as compared to the bulk composition of Psyche when it formed. Sulfur atoms ejected at significantly less than Psyche escape velocity would redeposit, distributing the sulfur from an exposed sulfide unit across a wider area, potentially complicating identification of those sulfide surface units' lateral extent. Based on previous work on ion sputtering in both lunar and asteroid space weathering (Szabo et al. 2022), the ejection velocity of any given sputtered surface atom is unlikely to be high enough for a significant fraction to escape, which raises the possibility of a thin, surficial layer of volatile sulfur atop surfaces surrounding FeS deposits. Nevertheless, there is a need to quantify the ejection velocity distribution, beyond just a characteristic root-mean-square velocity, to assess the full velocity range, given Psyche's small size. How much of the velocity distribution exceeds Psyche's escape velocity will influence how sulfur will be distributed across the surface, how much sulfur remains from the asteroid's formation, where we will detect sulfur on its surface with GRNS, and ultimately our interpretation of its redox state, per the Psyche mission's Level 1 science requirements.

Although the Santiago Papasquiero meteorite is unlikely to originate from Psyche (Buchwald 1975), the ejecta fragment analysis in Chapter 4 may still prove a useful analog for certain hypothetical units on Psyche's surface. Santiago Papasquiero's unique microstructure indicates it likely cooled much faster than octahedrites (Buchwald 1975). Such high cooling rates would represent not the solidification of an entire parent body, the typical hypothesis of other iron meteorites' origins, but a smaller volume of melt produced during a large impact into a metallic surface (Buchwald 1975). Several large impact structures have been proposed on Psyche (Landsman et al. 2018, Marchi et al. 2022, Shepard et al. 2022), and other hypothesized mechanisms are also capable of generating metallic surface melt (Abrahams and Nimmo 2019). If such a melt existed on Psyche's surface, it could cool into a metallic equivalent of a lunar mare unit with a microstructure like Santiago Papasquiero, which subsequent smaller impacts would disrupt in a similar manner to the Marchi et al. (2020) impact experiments. However, this "metallic mare" interpretation implies that the metallic equivalent of "primordial crust" that cools slowly over time would have a Widmanstätten microstructure more typical of iron meteorites and is thus less useful for interpreting Psyche's bulk composition.

Finally, the relative contribution of each process to forming Psyche's current surface remains unknown. For example, the balance of impacts versus fatigue in driving mechanical breakdown is uncertain. Even though fatigue is now hypothesized to be the major contributor to regolith formation on the smallest asteroids (Molaro et al. 2020), impacts at the scale of the impact gun experiment in Chapter 4 will still be relevant because: (a) Psyche's surface gravity is not negligible; (b) boulder-disrupting impacts are disproportionately responsible for impact-driven regolith formation (Melosh et al. 2011);

and (c) these impact experiments still inform the mechanical failure process as an iron meteorite block is mechanically stressed, even for non-impact sources of stress. Initial calculations suggest that Psyche's surface experiences extreme diurnal & annual surface temperature variation and thus may be susceptible to fatigue (Bierson et al. 2022), and multiple impact basins are hypothesized from interpretation of its surface shape model (Shepard et al 2022).

5.3. Future work

Our experiments have produced regolith particles with a variety of irregular shapes, in particular those particles which originate from rim flaps, crack spallation, or delamination. As discussed in Chapter 4, although silicate regoliths can take on a wide variety of textures, sizes, and morphologies, the specific shapes that we observe in metallic ejecta samples are novel. We hypothesize that the irregular concave shapes of metallic regolith particles may increase their sedimentary cohesiveness and angle of repose, but there is still ample ambiguity in metallic sedimentary properties. For that reason, future experiments must study how these particles settle in microgravity environments, and quantify the angle of repose, mass wasting, response to secondary impacts, vibrational stability, and other geomorphological characteristics of a metal-rich regolith.

The rate at which space weathered particles on the surface of a metallic asteroid are gardened by impact overturn and redeposition will have a strong controlling effect on how deep the weathered material is able to be distributed in the surface regolith, as described at the end of Chapter 2. This is important because if a space-weathered layer remains only as deep as the tens of nanometers penetration depth of solar wind ions and

equilibrium depth of atomic depletion, then the space-weathered layer may be too shallow to detect either with the Psyche Mission's GRNS or Multispectral Imager. Whereas if the space-weathered layer is propagated to meter-scale depth by gardening, then the weathered material will dominate the cross section of surface that the GRNS is able to measure, and the optical reflectance of the surface will be dominated by weathered material. Both the rate and the extent of gardening on a metallic surface will depend on both impact rates and the efficiency with which impacts can break down the metallic surface into smaller particles. While the impact and laser irradiation experiments in Chapters 3 and 4 show that such breakdown is possible, an estimate of metallic surface gardening rates will require additional types of data, such as the number and size distribution of particles produced in a given impact, and the fraction of those that remain on the surface instead of escaping.

Future work performing space weathering laboratory experiments should extend to other constituent mineral phases of iron meteorites and other metal-rich asteroid analogs. While space ion and laser irradiation experiments on oxides (Chaves et al. 2022) and chondrites (Laczniak et al. 2021) have begun to expand the scope of minerals and rock types investigated for space weathering, many of the most common phases in iron meteorites are still yet to be investigated. These include sulfides beyond pyrrhotite (e.g., daubréelite), phosphides (e.g., schreibersite), low-Fe silicates, and FeNi metal itself.

Ejecta fragment characterization will also continue with samples of Gibeon and Coahuila, the other two meteorites used as impact targets by Marchi et al. (2020). The Widmanstätten microstructure of octahedrites and the single-crystal kamacite structure of hexahedrites are not only geometrically different from Santiago Papasqiuero's

interlocking polygonal grains, they can also exhibit more complex grain boundaries with diverse crystallization textures, including plessitic rims and cloudy zones (Buchwald 1975). Therefore, we should not assume ejecta from impacts into octahedrites will exhibit similar deformation to Santiago Papasquiero.

Additional techniques would be worth exploring to better understand the fundamental physics of space weathering and impacts as they occur on asteroid surfaces. Helium Ion Microscopy (HIM) would enable simultaneous irradiation of sample surfaces with ions at solar wind energies and fluences, while also using that same ion beam to image the surface (Wirtz et al. 2019). Atom Probe Tomography (APT) can potentially enable laser irradiation experiments simulating micrometeoroid impacts or surface heating to simultaneously collect data on the material sputtered away from the sample surface and also directly measure the rate of thermally driven diffusion on the surface during impact (Bachhav et al. 2011). Finally, more energetic irradiation techniques such as X-ray Synchrotron irradiation and Neutron Beam Tomography may be able to directly measure where vacancy sites and implanted ions preferentially accumulate within the crystal lattice of irradiated metal (Connolly et al. 2018), which may reveal specific locations in the microstructure where fractures are likely to nucleate in response to impacts or heating, which may reveal even more about the mechanics of how they break down.

Beyond just investigation of Psyche, several cross-applications of this research may be relevant for both future space exploration and for other areas of geology and materials science. Metal-bearing surfaces may be found on silicate asteroids, planets, and moons throughout the solar system, both as a by-product of space weathering and the

result of other geologic processes. While we have previously understood the metallic surfaces formed by space weathering to be the end product of that process, it is worth investigating how those metallic surfaces themselves undergo weathering over subsequent geologic time. Our interpretations of rocky planetary surfaces may hide additional complexity in these microscopic metal grains.

The interactions of metallic materials with the space environment potentially have some spinoff applications for metallurgy. Because of the constraints on how long it takes to synthesize a metallurgical sample for engineering purposes, the grain sizes that are typically produced for metallurgical materials are significantly finer than even the microscopic Widmanstätten lattices found in ataxites (Buchwald 1975, Petrovic 2011). However, due to slow geologic-timescale cooling rates iron meteorites can feature grain sizes that range from microscopic to centimeters. A metallic material with such large grain sizes presents an opportunity to explore the meso-scale effects of a variety of processes that are relevant for metallurgical engineers and materials scientists. Hydrogen embrittlement has been a long-running problem for industrial metallurgy, particularly in corrosive environments, high-radiation applications, and in hydrogen infrastructure where metal is directly exposed to H_2 gas or cryogenic liquid (Martin et al. 2018). Moreover, long-duration exposure of materials to the space environment is becoming especially relevant as we are planning long-term spacecraft missions, not just to more remote destinations in the solar system, but also with permanent or semipermanent human exploration of the near solar system, such as cis-lunar space and near-Earth asteroids. Investigating how solar wind protons affect the microstructure of meteoritic metals potentially provides an avenue to understand the fundamental physical processes

occurring in engineered materials at mesoscales and over long durations of exposure, in ways a synthetic metal sample would not be able to replicate. Even though meteorites are only a limited analog for industrial metals, investigating the meso-scale and long-duration properties of metals is nevertheless necessary to understanding why engineered materials behave in the ways they do, how they fail, and the modes of modification that they can experience in their use environment.

REFERENCES

Abrahams, J.N.H. and Nimmo, F. (2019) Ferrovolcanism: Iron Volcanism on Metallic Asteroids, *Geophysical Research Letters* 46, p. 5055-5064

Adams, J. B. & McCord, T. B. (1971) Alteration of lunar optical properties: age and composition effects. *Science* 171, 567-571

Alexander, A., Marchi, S., Gestos, A., and Chocron, S. (2022) Material properties and analysis of impact-induced porosity in the Santiago Papasquiero meteorite, *Meteoritics and Planetary Science* 57

Allen, N. P. and Earley, C. C. (1950) The transformations $\alpha \rightarrow \gamma$ and $\gamma \rightarrow \alpha$ in iron-rich binary iron-nickel alloys, *Journal of the Iron and Steel Institute of Japan* 166, p. 281–288

Arai, T., Okada, T., Yamamoto, Y. et al. (2008) Sulfur abundance of asteroid 25143 Itokawa observed by X-ray fluorescence spectrometer onboard Hayabusa, *Earth Planet Space* 60, 21–31.

Arredondo, R., Oberkofler, M., Schwarz-Selinger, T., von Toussaint, U., et al. (2019) Angle-dependent sputter yield measurements of keV D ions on W and Fe and comparison with SDTrimSP and SDTrimSP-3D *Nuclear Materials and Energy* 18, 72–76.

Armstrong, R. W. (1964) On determining the ductile-brittle transition temperature, *Philosophical Magazine*, p. 1063-1067

Ashby, M. F. (1999) *Materials Selection in Mechanical Design*, 2nd Edition. Oxford: Elsevier

Auciello, O. (1984) Historical Overview of ion-induced morphological modification of surfaces, In *Beam Modification of Materials*; Elsevier, Amsterdam

Auten, T. A. (1973) On the brittleness of Gibeon meteoritic iron. *Meteoritics* 8, 189-196

Bacchav, M. N., Danoix, R., Vurpillot, F., Hannoyer, B., Ogale, S. B., Danoix, F. (2011) Evidence of lateral heat transfer during laser assisted atom probe tomography analysis of large band gap materials, *Applied Physics Letters* 99

Backlund, H.G. (1938) The Problems of the Rapakivi Granites, *The Journal of Geology* 46, p. 339-396

Bagus, P.S, Nelin, C.J., Brundle, C.R., Crist, B.V., Lahiri, N., and Rosso, K.M., (2021) Combined multiplet theory and experiment for the Fe 2p and 3p XPS of FeO and Fe_2O_3, *The Journal of Chemical Physics* 154, 094709.

Ballouz, R.-L., Barnouin, O.S., Daly, R. T., Ernst, C. M., Sugita, S., Walsh, K. J., Pajola, M., Lucchetti, A., Raducan, S., Jutzi, M., Schwarts, S. R., Cambioni, S., Asphaug, E., Nolan, M. C., and Kohout, T. (2023) Disrupted Boulders on the Surfaces of Near-Earth Asteroids Bennu, Ryugu, and Dimorphos, *Lunar and Planetary Science Conference LIV,* Abstract #2505

Baragiola, R.A., (2004) Sputtering: survey of observations and derived principles. *Philosophical Transactions of the Royal Society of London A: Mathematical, Physical and Engineering Sciences* 362, 29-53.

Baratoux, D. and Melosh, H.J. (2003) The formation of shatter cones by shock wave interference during impacting, *Earth and Planetary Science Letters* 216, 43-54

Barr, T. L. and Seal, S. (1995) Nature of the use of adventitious carbon as a binding energy standard, *Journal of Vacuum Science & Technology* 13, 1239-1246.

Barucci, M. A., Fulchignoni, M., Fornasier, S., Dotto, E., Vernazza, P., Birlan, M., Binzel, R. P., Carvano, J., Merlin, F., Barbieri, C., and Belskaya, I. (2005) Asteroid target selection for the new Rosetta mission baseline: 21 Lutetia and 2876 Steins, *Astronomy and Astrophysics* 430 p. 313-317

Barucci, M. A., Fornasier, S., Dotto, E., Lamy, P. L., Jorda, L., Groussin, O., Brucato, J. R., Carvano, J., Alvarez-Candal, A., Cruikshank, D., and Fulchignoni, M. (2008) Asteroids 2867 Steins and 21 Lutetia: surface composition from far infrared observations with the Spitzer space telescope, *Astronomy and Astrophysics* 477 p. 665-670

Belskaya et al. 2010 Puzzling asteroid 21 Lutetia: our knowledge prior to the Rosetta fly-by

Betz, G. and Wehner, G.K., 1983. Sputtering of multicomponent materials. In *Sputtering by Particle Bombardment II* (pp. 11-90). Heidelberg: Springer.

Bercovici, D. and Ricard, Y. (2012) Mechanisms for the generation of plate tectonics by two-phase grain-damage and pinning, *Physics of the Earth and Planetary Interiors* p.27-55 http://dx.doi.org/10.1016/j.pepi.2012.05.003

Bezaeva, N. S., Gattacceca, J., Rochette, P., Duprat, J., Rizza, G., Vernazza, P., Trukhin, V. I., and Skripnik, A. (2015) The effect of irradiation on the magnetic properties of rock and synthetic samples: Implications to irradiation of extraterrestrial minerals in space, *Physics of the Solid Earth* 51 336-353.

Biesinger, M. C., Payne, B. P., Grosvener, A. P., Laua, L. W. M., Gerson, A. R., and Smart, R. St. C. (2011) Resolving surface chemical states in XPS analysis of first

row transition metals, oxides and hydroxides: Cr, Mn, Fe, Co and Ni, *Applied Surface Science* 257 2717-2730.

Bierson, C. J., Elkins-Tanton, L. T., and O'Rourke, J. G. (2022) The Geologic Impact of 16 Psyche's Surface Temperatures, *The Planetary Science Journal* 3 p. 196

Birlan, M., Vernazza, P., Fulchignoni, M., Barucci, M. A., Descamps, P., Binzel, R. P., and Bus, S. J. (2006) Near infra-red spectroscopy of the asteroid 21 Lutetia: I. New results of long-term campaign, *Astronomy and Astrophysics* 454, p. 677-681

Bohdansky, J., Bay, H. L., and Roth, J. (1977) In: Proceedings of the 7th International Vacuum Congress and 3rd Interactional conference of Solid Surfaces, ed. by R. Dobrozemsky, F. Rudenauer, F.P. Viehbock, A. B. Reth, Private publisher: Vienna.

Bowell, E., Chapman, C. R., Gradie, J. C., Morrison, D., and Zellner, B. (1978), *Icarus* 35, p. 313

Boydens, F., Leroy, W.P., Persoons, R., and Depla, D. (2013) The influence of target surface morphology on the deposition flux during direct-current magnetron sputtering, *Thin Solid Films*, 531, 32-41.

Brion, D. (1980) Etude par spectroscopie de photoelectrons de la degradation superficielle de FeS2, CuFeS2, ZnS et PbS a l'air et dans l'eau, *Applications of Surface Science* (in French) 5, 133-152.

Broek, D. (1982) *Elementary Engineering Fracture Mechanics, 3rd Ed.* The Hague, Netherlands

Buchwald, V. F. (1975) *Handbook of Iron Meteorites*, University of California Press

Burbine, T. H. (2017) *Asteroids*, Cambridge University Press

Burbine, T. H. and Binzel, R. P. (2002) Small Main-Belt Asteroid Spectroscopic Survey in the Infrared, *Icarus* 159, p. 468-499

Burns, R. G., & Burns, R. G. (1993). *Mineralogical applications of crystal field theory (No. 5).* Cambridge University Press.

Cambioni, S., Delbo, M., Poggiali, G., Avdellidou, C., Ryan, A. J., Desapriya, J. D. P., Asphaug, E., Ballouz, R. L., Barucci, M. A., Bennett, C. A., Bottke, W. F., Brucato, J. R., Burke, K. N., Cloutis, E., DellaGiustina, D. N., Emery, J. P., Rozitis, B., Walsh, K. J., and Lauretta, D. S. (2021) Fine-regolith production on asteroids controlled by rock porosity, *Nature* 598, 49-52

Campbell, B. A. (2002) *Radar Remote Sensing of Planetary Surfaces*, Cambridge University Press

Carey, W. C. & McDonnell, J. A. M. (1976) Lunar surface sputter erosion - A Monte Carlo approach to microcrater erosion and sputter redeposition in Lunar Science Conference, 7th, Houston, Tex., March 15-19, 1976, Proceedings. Volume 1. (A77-34651 15-91) Pergamon Press, Inc: New York.

Carslaw, H.S. and Jaeger, J.C. (1959), *Conduction of Heat in Solids*, 2nd Edition, Oxford

Cassidy, T. A., and Johnson, R. E. (2005) Monte Carlo model of sputtering and other ejection processes within a regolith, *Icarus* 176, 499

Chapman, C. R., Morrison, D., and Zellner, B. (1975) Surface Properties of Asteroids: A Synthesis of Polarimetry, Radiometry, and Spectrophotometry, *Icarus* 25 p. 104-130

Chapman, C.R. (1996) S-type asteroids, ordinary chondrites, and space weathering: the evidence from Galileo's Fly-bys of Gaspra and Ida. (Invited review). *Meteoritics & Planetary Science* 31, 699-726.

Chapman, C.R. (2004) Space weathering of asteroid surfaces, *Annual Review of Earth and Planetary Sciences* 32, 539-567

Chase, M.W., Jr. (1998) NIST-JANAF Themochemical Tables, Fourth Edition, *Journal of Physical Chemistry Reference Data*, Monograph 9, 1-1951.

Chaves, L.C., et al. (2021) Space Weathering Features in a Sulfide Grain from Asteroid Itokawa. Presented at *Lunar and Planetary Science Conference LII* Abstract #1770

Christoffersen, R. and Keller, L.P. (2011), Space radiation processing of sulfides and silicates in primitive solar systems materials: Comparative insights from in situ TEM ion irradiation experiments. *Meteoritics & Planetary Science* 46, 950-969. https://doi.org/10.1111/j.1945-5100.2011.01203.x

Christoph, J. M. (2021, April 2). Interpretation of solar wind ion irradiation experimental and model simulations. Retrieved from https://doi.org/10.17605/OSF.IO/ST79B

Christoph, J. M., Minesinger, G. M., Bu, C., Dukes, C. A., and Elkins-Tanton (2022) Space Weathering Effects in Troilite by Simulated Solar Wind Hydrogen and Helium Ion Irradiation, *Journal of Geophysical Research – Planets* 127

Clark B.E., Fanale, P., and Salisbury, J.W. (1992) Meteorite-asteroid spectral comparison: The effects of comminution, melting, and recrystallization, *Icarus* 97, 288-297

Clark R.N. (1999). Spectroscopy of rocks and minerals, and principles of spectroscopy. In *Manual of Remote Sensing, 3rd ed.*, edited by Rencz A. N. John Wiley & Sons. pp.3-58.

Coffa, S., Poate, J. M., and Jacobson, D. C. (1992) Determination of diffusion mechanisms in amorphous silicon, *PHYSICAL REVIEW B* 45

Connolly, M., Park, J. S., Bradley, P., Lauria, D., Slifka, A., and Drexler, E. (2018) Demonstration of a chamber for strain mapping of steel specimens under mechanical load in a hydrogen environment by synchrotron radiation, *Review of Scientific Instruments* 89

Cottrell, A. H. (1958) Theory of brittle fracture in steel and similar materials. *Trans. Met. Soc. AIME* 212, 192-203

DeBroglie, I., Beck, C., Liu, W. & Hofmann, F. (2015) Temperature Dependence of Helium--Implantation--Induced Lattice Swelling in Polycrystalline Tungsten: X--ray Micro--Diffraction and Eigenstrain Modelling, *Scripta Materialia* 107, 4

Delbo, M., Libourel, G., Wilkerson, J., Murdoch, N., Michel, P., Ramesh, K.T., Ganino, C., Verati, C., and Marchi, S. (2014) Thermal fatigue as the origin of regolith on small asteroids, *Nature* 508, p.233-236 doi:10.1038/nature13153

DeMeo, F. E., Binzel, R. P., Slivan, S. M., and Bus, S. J. (2009). An extension of the Bus asteroid taxonomy into the near-infrared, *Icarus* 202, p. 160–180

DeMeo, F., Binzel, R.P., Slivan, S.M., and Bus, S.J. (2020). Bus-DeMeo Asteroid Taxonomy V1.0. urn:nasa:pds:ast.bus-demeo.taxonomy::1.0. *NASA Planetary Data System*; https://doi.org/10.26033/089p-c283

Descostes, M., Mercier, F., Thromat, N., Beaucaire, C. and Gautier-Soyer, M. (2000) Use of XPS in the determination of chemical environment and oxidation state of iron and sulfur samples: constitution of a data basis in binding energies for Fe and S reference compounds and applications to the evidence of surface species of an oxidized pyrite in a carbonate medium, *Applied Surface Science* 165, 288-302

Dibb, S.D. and Bell, J.F. (2018) Optimization of Narrowband Visible to Near-IR Filters for the Psyche Multispectral Imager. Presented at *Lunar and Planetary Science Conference XLIX* Abstract #2083

Dibb, S. D., Bell, J. F., Elkins-Tanton, L. T., and Williams, D. A. (2021) Visible to Near-Infrared Reflectance Spectroscopy of Asteroid (16) Psyche: Implications for the Psyche Mission's Science Investigations, *Earth and Space Science* 10

Dobes, K., Naderer, P., Lachaud, N., Eisenmenger-Sittner, C., & Aumayr, F. (2011). Sputtering of tungsten by N+ and N2+ ions: Investigations of molecular effects. *Physica Scripta*, T145, 014017. https://doi.org/10.1088/0031-8949/2011/T145/014017

Dollfus, A., Mandeville, J. C., and Duseaux, M. (1979), *Icarus* 37, p. 124

Dukes, C. A., Baragiola, R. A., and McFadden, L. A. (1999) Surface modification of olivine by H^+ and He^+ bombardment, *Journal of Geophysical Research: Planets* 104, 1865-1872

Dukes, C. A., Chang, W., Famá, M., and Baragiola, R. A. (2011) Laboratory studies on the sputtering contribution to the sodium atmospheres of Mercury and the Moon, *Icarus* 212, 463-469

Durda, D.D. and Flynn, G. J. (1999) Experimental Study of the Impact Disruption of a Porous, Inhomogeneous Target, *Icarus* 142, p. 46-55

Durda, D., Chapman, C. R., Cintala, M. J., Flynn, G. J., Strait, M. M., and Minnick, A. (2011) Experimental investigation of the impact fragmentation of blocks embedded in regolith: Impact fragmentation of blocks in regolith, *Meteoritics and Planetary Science*, doi:10.1111/j.1945-5100.2010.01163.x

Ehsani, H., Boyd, J.D., Wang, J., and Grady, M.E. (2021) Evolution of the Laser-Induced Spallation Technique in Film Adhesion Measurement, *Applied Mechanics Reviews* https://doi.org/10.1115/1.4050700

Elkins-Tanton, L. T., Asphaug, E., Bell, J. F., Bercovici, H., Bills, B., Binzel, R., Bottke, W. F., Dibb, S., Lawrence, D. J., Marchi, S., McCoy, T.J., Oran, R., Park, R. S., Peplowski, P. N., Polanskey, C. A., Prettyman, T. H., Russell, C. T., Schaefer, L., Weiss, B. P., Wieczorek, M. A., Williams, D. A., and Zuber, M. T. (2020) Observations, Meteorites, and Models: A Preflight Assessment of the Composition and Formation of (16) Psyche, *Journal of Geophysical Research – Planets* 125

Farinella, P. and Davis, D. R. (1992) Collision rates and impact velocities in the main asteroid belt, *Icarus* 97, p. 111-123

Farrell, W.M., Hurley, D.M., and Zimmerman, M.I. (2015) Solar wind implantation into lunar regolith: Hydrogen retention in a surface with defects, *Icarus* 255, 116-126

Feierberg, M. A., Witteborn, F. C., and Lebovsky, L. A. (1983), *Icarus* 56, p. 393

Ferro, D., Piacente, V., and Scardala, P. (1989) Decomposition enthalpies of iron sulfides, *The Journal of chemical thermodynamics* 21, p. 583-494

Fick, A. (1855). Ueber Diffusion, *Annalen der Physik* (in German) 94, 59–86

Fink, D., Meirav, O., Paul, M., Ernst, H., Henning, W., Kutschera, W., Kaim, R., Kaufman, A., and Magaritz, M. (1984) Experiments on the sputtering if group VI elements, *Nuclear Instruments and Methods in Physics Research Section B: Beam Interactions with Materials and Atoms* 1, 275-281

Formisano, M., Turrini, D., Federico, C., Capaccioni, F., and De Sanctis, M. C. (2013) The onset of differentiation and internal evolution: the case of 21 Lutetia, *The Astrophysical Journal* 770, p. 50

French, B.M. (1999) *Traces of catastrophe: A handbook of shock-metamorphic effects in terrestrial meteorite impact structures*, Lunar and Planetary Institute

Gaffey, M., Bell, J.F., Brown, R., Burbine, T., Piatek, J., Reed, K., and Chaky, D. (1993) Mineralogical variations within the s-type asteroid class, *Icarus* 106, 573-602

Gash, P.J.S. (1971) Dynamic mechanism for the formation of shatter cones, *Nature Physical Science*

Gault, D.E. (1970) Saturation and equilibrium conditions for impact cratering on the lunar surface: Criteria and implications. *Radio Science* 5, p. 273-291

Gault, D.E., Hörz, F., Brownlee, D.E., and Hartung, J. B. (1974) Mixing of the lunar regolith. In *Proceedings of the Fifth Lunar Science Conference*, Houston, TX p. 2365

Gertsch, R., Gertsch, L.S., and Remo, J. L. (2006) Mining Near-Earth Resources, *New York Academy of Sciences*

Gillis-Davis, J.J., Lucey, P.G., Bradley, J.P., Ishii, H.A., Kaluna, H.M., Misra, A., and Connolly, H.C. (2017) Incremental laser space weathering of Allende reveals non-lunar like space weathering effects, *Icarus* 286, p.1-14

Gold, T. (1955) The lunar surface, *Royal Astronomical Society* 115, 585-604

Goldstein, J. I. and Doan, A. S. (1972) The effect of phosphorous on the formation of the Widmanstätten pattern of iron meteorites. *Geochimica et Cosmochimica Acta* 36, p.51–69

Goldstein, J. I., Scott, E. R. D., and Chabot, N. L. (2009) Iron meteorites: Crystallization, thermal history, parent bodies, and origin, *Chemie der Erde* 69, p. 293-325

Gordon, R.B. (1970) Mechanical properties of iron meteorites and the structure of their parent bodies. *Journal of Geophysical Research* 75, 439-447

Goretzki H., Rosenstiel P.V., Mandziej S., and Fres. Z. (1989) *Analytical Chemistry* 333, 451

Grady, M. C., Pratesi, G., and Cechi, V. M. (2014) *Atlas of Meteorites,* Cambridge University Press

Grava, C., Killen, R.M., Benna, M., et al. (2021) Volatiles and Refractories in Surface-Bounded Exospheres in the Inner Solar System. *Space Science Reviews,* 217, 61, https://doi.org/10.1007/s11214-021-00833-8

Graves, K.J., Minton, D.A., Molaro, J.L., and Hirabayashi, M. (2019) Resurfacing asteroids from thermally induced surface degradation, *Icarus* 322, p.1-12

Greeley, R. (2013) *Introduction to Planetary Geomorphology*, Cambridge University Press

Gregossian, A., Tavassoli, S.H, and Shokri, B. (2009) Laser ablation of aluminum from normal evaporation to phase explosion, *Journal of Applied Physics* 105 https://doi.org/10.1063/1.3131689

Grosskreutz, J.C. (1970) *Technical Report AFML-TR-70-55*, USAF Materials Laboratory, Wright-Patterson AFB, Ohio

Hall, E. O. (1951) *Proceedings of the Royal Society*, London, 474

Hapke, B. (2001) Space weathering from Mercury to the asteroid belt, *Journal of Geophysical Research* 106, 10,039-10,073

Hapke, B. and Cassidy, W. (1978) Is the Moon really as smooth as a billiard ball? Remarks concerning recent models of sputter-fractionation on the lunar surface, *Geophysical Research Letters* 5, 297

Harries and Langenhorst (2014) The mineralogy and space weathering of a regolith grain from 25143 Itokawa and the possibility of annealed solar wind damage, *Earth, Planets, and Space* 66, 1-11

Hausch, G. (1990) High temperature specific heat of FeNi and FePt Invar alloys, *Journal of Magnetism and Magnetic materials* 92, p. 87-91

Haynes, W. M., Lide, D. R., & Bruno, T. J. (2016) *CRC handbook of chemistry and physics: a ready-reference book of chemical and physical data*. 97th ed. CRC Press: Boca Raton, Florida.

Heln, A. M., Matheson, R., and Fries, D. (2020) A techno-economic analysis of asteroid mining, *Acta Astronautica* 168

Hofsäss, Zhang, and Mutzke (2014) *Applied Surface Science* 310, 134-141.

Holzhausen, G.R. (1989) Origin of sheet structure, 1. Morphology and boundary conditions, *Engineering Geology* 27, p.225-278

Hörz, F. (1977) Impact cratering and regolith dynamics, *Physics and Chemistry of the Earth* 10, p. 3-15

Hörz, F. and Cintala, M. J., (1997) Impact experiments related to the evolution of planetary regoliths, *Meteoritics and Planetary Science* 32, 179-209

Hörz, F., Basilevsky, A.T., Head, J.W., and Cintala, M. J. (2020) Erosion of lunar surface rocks by impact processes: A synthesis, *Planetary and Space Science* 194

Housen, K.R., Wilkening, L.L., Chapman, C.R., and Greenberg, R. (1979) Asteroidal regoliths, *Icarus* 39, 317-351

Idczak, K., Idczak, R., and Konieczny, R. (2016) An investigation of the corrosion of polycrystalline iron by XPS, TMS and CEMS, *Physica B: Condensed Matter* 491, 37-45

Ihlemann, J., Wolff, B., and Simon, P. (1992) Nanosecond and femtosecond excimer laser ablation of fused silica, *Applied Physics A* 54, p. 363-368

Janssen, M., Zuidema, J., and Wanhill, R.J.H., (2002) *Fracture Mechanics*, Delft University Press

Jaumann, R., Bell, J. F., Polanskey, C. A., Raymond, C. A., Asphaug, E., Bercovici, D., Bills, B. R., Binzel, R., Bottke, W., Christoph, J. M., Marchi, S., Neesemann, A., Otto, K., Park, R. S., Preusker, F., Roatsch, T., Williams, D. A., Wieczorek, M. A., and Zuber, M. T. (2022) The Psyche Topography and Geomorphology Investigation, *Space Science Reviews* 218

Johnson, A. A., Remo, J. L., and Davis, R. B. (1979) The low temperature impact properties of the meteorite Hoba, *Journal of Geophysical Research* 84

Johnson, G. P. and Talbot, R. J. (1964) A theoretical study of the shock wave origin of shatter cones, *Air Force Institute of Technology, Wright-Patterson AFB*

Kajita, S., Ishida, T., Ohno, N., Hwangbo, D., and Yoshida, T. (2016) Fuzzy nanostructure growth on Ta/Fe by He plasma irradiation, *Scientific Reports* 6, 1-10

Kargel, J. S. (1994) Metalliferous asteroid as potential sources of precious metals, *Journal of Geophysical Research – Planets* 99 p. 21129-21141

Keihm, S., Tosi, F., Kamp, L., Capaccioni, F., Grassi, D., Gulkis, S., Grassi, D., Hofstadter, M., Filacchione, G., Lee, S., Giuppi, S., Janssen, M., and Capria, M. (2011) Interpretation of combined infrared, submillimeter, and millimeter thermal flux data obtained during the Rosetta fly-by of Asteroid (21) Lutetia, *Icarus* 221 p. 395-404

Keller, L. P., Loeffler, M. J., Christoffersen, R., Dukes, C., Rahman, Z., and Baragiola, R. (2010) Irradiation of FeS: Implications for the lifecycle of sulfur in the interstellar medium and presolar FeS grains, *Lunar and Planetary Science Conference XLI*

Keller, L. P. and McKay, D.S. (1997) The nature and origin of rims on lunar soil grains, *Geochimica et Cosmochimica Acta* 61, 2331-2341

Keller, L. P. and Rahman, Z. (2014) Relative sputtering rates of FeS, MgS, and Mg Silicates: Implications for ISM Gas Phase Depletions of Rock-Forming Elements, *NASA NTRS*

Keller, L. P., Rahman, Z., Hiroi, T., Sasaki, S., Noble, S. K., Hörz, F., and Cintala, M. J. (2013) Asteroidal space weathering: the major role of FeS. Presented at *Lunar and Planetary Science Conference XLIV* Abstract #2404

Killen, R. M. (2003) Depletion of sulfur on the surface of asteroids and the moon, *Meteoritics & Planetary Science* 38, 383-388

Kirchhoff, W.H. (2012) Logistic Function Profile Fit: A least-squares program for fitting interface profiles to an extended logistic function, *Journal of Vacuum Science & Technology A* 30, 5

de Kleer, K., Cambioni, S., and Shepard, M. (2021) The Surface of (16) Psyche from Thermal Emission and Polarization Mapping, *The Planetary Science Journal* 2 p. 149

Kracher, A. and Sears, D.W.G. (2005) Space weathering and the low sulfur abundance of Eros, *Icarus* 174, 36-45

Laczniak, D. L., Thompson, M. S., Christofferson, R., Dukes, C.A., Clemett, S.J., Morris, R.V., and Keller, L.P. (2021) Characterizing the spectral, microstructural, and chemical effects of solar wind irradiation on the Murchison carbonaceous chondrite through coordinated analysis. *Icarus* 364, https://doi.org/10.1016/j.icarus.2021.114479

Landsman, Z.A., Campins, H., Pinilla-Alonzo, N., Hanus, J., and Lorenzi, V. (2015) A new investigation of hydration in the M-type asteroids, *Icarus* 252, 186-198

Landsman, Z.A., Emery, J.P., Campins, H., Hanus, J., Lim, L.F., and Cruikshank, D.P. (2018) Asteroid (16) Psyche: Evidence for a silicate regolith from Spitzer space telescope spectroscopy, *Icarus* 304

Lawn, B.R. and Wilshaw, T.R. (1975) *Fracture of Brittle Solids*, Cambridge University Press

Lazarus, D. (1985) Diffusion in Crystalline and Amorphous Solids, Presented at *Symposium I – Phase Transitions in Condensed Systems--Experiments and Theory* 57, 297

Lazzarin, M., Marchi, S., Moroz, L. V., and Magrin, S. (2009) New visible spectra and mineralogical assessment of (21) Lutetia, a target of the Rosetta mission, *Astronomy and Astrophysics* 498, p. 307-311

Lennie, A. and Vaughan, D. J., ed. Dyar, M. D., McCammon, C., and Schaefer, M. W. (1996) Spectroscopic studies of iron sulfide formation and phase relations at low temperatures, *The Geochemical Society, Special Publication No.5*

Lewis, J. S. (1996) *Mining the Sky: Untold Riches from the Asteroids, Comets, and Planets*, Addison-Wesley, Reading, MA

Lewis, J. S. (2016) NIAC Phase I Final Report for NNX15AL85G: In-Space Production of Storable Propellants, *Deep Space Industries Inc.*

Lewis, J. S. and Nozette, S. (1983) Extraction and Purification of Iron-Group and Precious metals from Asteroidal Feedstocks, *Advances in Astronautical Science* 53, p. 351

Liechti, K. (2008) Delamination Mechanics, in *Handbook of Experimental Solid Mechanics*, p.961-984, Springer

Lipschutz, M. E. and Anders, E. (1964) Cohenite as a pressure indicator in iron meteorites?, *Geochimica et Cosmochimica Acta* 28, p. 699-711

Loeffler, M. J., Dukes, C. A., Chang, W. Y., McFadden, L. A., and Baragiola, R. A. (2008) *Laboratory simulations of sulfur depletion at Eros*, Icarus 299, 240-252

Loeffler, M.J., Dukes, C.A., and Baragiola, R.A. (2009) Irradiation of olivine by 4keV He^+: Simulation of space weathering by the solar wind, *Journal of Geophysical Research Planets* v. 114 https://doi.org/10.1029/2008JE003249

Loeffler, M.J., Dukes, C.A., Christoffersen, R., and Baragiola, R.A. (2016) Space weathering of silicates simulated by successive laser irradiation: In situ reflectance measurements of Fo_{90}, Fo_{99+}, and SiO_2, *Meteoritics & Planetary Science* 51, 261-275

Mahjoub, A., Poston, M.J., Blacksberg, J., Eiler, J.M., Brown, M.E., Ehlmann, B.L., Hodys, R., Hand, K.P., Carlson, R., and Choukroun, M. (2017) Production of Sulfur Allotropes in Electron Irradiated Jupiter Trojans Ice Analogs, *The Astrophysical Journal* 846, 148

Marchi, S., Durda, D. D., Polanskey, C. A., Asphaug, E., Bottke, W. F., Elkins-Tanton, L. T., Garvie, L. A. J., Ray, S., Chocron, S., and Williams, D. A. (2020) Hypervelocity Impact Experiments in Iron-Nickel Ingots and Iron Meteorites: Implications for the NASA Psyche Mission, *Journal of Geophysical Research – Planets* 125, e2019JE005927. https://doi.org/10.1029/2019JE005927

Martel, S.J. (2017) Progress in understanding sheeting joints over the past two centuries, *Journal of Structural Geology* 94, p. 68-86

Martin, M. L., Connolly, M. J., DelRio, F. W., and Slifka, A. J. (2020) Hydrogen embrittlement in ferritic steels, *Applied Physics Reviews* 7

Massironi, M., Marchi, S., Pajola, M., Snodgrass, C., Thomas, N., Tubiaa, C., Vincent, J. B., Cremonese, G., Da Deppo, V., Ferri, F., Magrin, S., Sierks, H., Barbieri, C., Lamy, P., Rickman, H., Rodrigo, R., and Koschny, D. (2012) Geologic map and stratigraphy of asteroid 21 Lutetia, *Planetary and Space Science* 66, p. 125-236

Matsumoto, T., Harries, D., Langenhorst, F., Miyake, A., and Noguchi, T. (2020) Iron whiskers on asteroid Itokawa indicate sulfide destruction by space weathering. *Nature Communications* 11, 1117 https://doi.org/10.1038/s41467-020-14758-3

Matsumoto, T., Noguchi, T., Tobimatsu, Y., Harries, D., Langenhorst, F., Miyake, A., and Hidaka H. (2021) Space weathering of iron sulfides in the lunar surface environment. *Geochimica et Cosmochimica Acta*, 299, 69-84, https://doi.org/10.1016/j.gca.2021.02.013

Mcintyre, N. S., and Zetaruk, D. G. (1977) X-ray photoelectron spectroscopic studies of iron oxides, *Analytical Chemistry* 49, 1521-1529.

McKay, D.S. and Ming, D.W. (1992) Properties of Lunar Regolith, *Developments in Soil Science* 19 p. 449-462

McSween, H. Y., Binzel, R. P., De Sanctis, M. C., Ammannito, E., Prettyman, T. H., Beck, A. W., Reddy, V., Le Corre, L., Gaffey, M. J., McCord, T. B., Raymond, C. A., Russell, C. T., and the Dawn Science Team. (2013) Dawn; the Vesta-HED connection; and the geologic context for eucrites, howardites, and diogenites, *Meteoritics and Planetary Science* 48, p. 2090-2104

Melosh, J. (2011) "Regolith" in *Planetary Surface Processes*, Cambridge University Press

Meteoritical Bulletin (2023) Accessed April 5, 2023. https://www.lpi.usra.edu/meteor/

Meyer, F.W. (2018) He-ion induced surface morphology change and nanofuzz growth on hot tungsten surfaces, *Journal of Physics B: Atomic, Molecular, and Optical Physics* 52, 1-22

Meyers, M, and Chawla, K. (2014) *Mechanical Behavior of Materials, 2nd Ed.* Cambridge University Press

Michkami, T., Hagermann, A., Kadokawa, T., Yoshida, A., Shimada, A., Hasegawa, S., and Tsuchiyama, A. (2016) Fragment shapes in impact experiments ranging from cratering to catastrophic disruption, *Icarus* 264, p. 316-330

Molaro, J. and Byrne, S. (2012) Rates of temperature change of airless landscapes and implications for thermal stress weathering, *Journal of Geophysical Research* 117, doi:10.1029/2012JE004138

Molaro, J., Byrne, S., and Le, J.-L. (2017) Thermally induced stresses in boulders on airless body surfaces, and implications for rock breakdown, *Icarus* 294, p.247-261 http://dx.doi.org/10.1016/j.icarus.2017.03.008

Molaro, J.L., Hergenrother, C.W., Chesley, S.R., et al. (2020) Thermal Fatigue as a Driving Mechanism for Activity on Asteroid Bennu, *Journal of Geophysical Research – Planets* 125 https://doi.org/10.1029/2019JE006325

Moore, C.B., Lewis, C. F., and Nava, D. (1969) Superior Analysis of Iron Meteorites, p. 738-748 in *Meteorite Research,* Millman, P. M. ed., D. Reidel Publishing Co., Dordrecht, Netherlands

Moreau, J., Kohout, T., and Wuennemann, K. (2018) Melting efficiency of troilite-iron assemblages in shock-darkening: Insight from numerical modeling, *Physics of the Earth and Planetary Interiors* 282

Moretti, P. F., Maras, A., and Folco, L. (2007) Space weathering, reddening and gardening of asteroids: A complex problem, *Advances in Space Research* 40, p. 258-261

Moulder, J. F., Stickle, W. F., Sobol, P. E., Bomben, K. D., ed. Chastein, J. (1991) *Handbook of X-ray Photoelectron Spectroscopy*, Physical Electronics Inc.: Chanhassen, MN

Mutzke, A., Schneider, R., Eckstein, W., Dohmen, R., Schmid, K., Toussaint, U. v., et al.(2019). SDTrimSP Version 6.00 (IPP 2019-02). Max-Planck-Institut für Plasmaphysik: Garching. doi:10.17617/2.3026474

Nakamura, T., Noguchi, T., Masahiko, T., Zolensky, M., Kimura, M., Tsuchiyama, A. et al. (2011) Itokawa Dust Particles: A Direct Link Between S-Type Asteroids and Ordinary Chondrites. *Science*, 333, 1113-1116, doi:10.1126/science.1207758

Narayan, C. and Goldstein, J. I. (1984) Nucleation of intragranular ferrite in Fe-Ni-P alloys, *Metallurgical Transactions A* 15, p. 861–865.

Neukum, G., Koenig, B., and Arkani-Hamed, J. (1974) A study of lunar impact crater size-distributions, *The Moon* 12, p. 201-229

Neumann, W., Breuer, D., and Spohn, T. (2013) The thermo-chemical evolution of Asteroid 21 Lutetia, *Icarus* 224, p. 126-143

Nittler, L.R., Starr, R.D., Lim, L., McCoy, T.,J., Burbine, T.H., Reedy, R.C., Trombka, J.I., Gorenstein, P., Squyres, S.W., Boynton, W.V., Mcclanahan, T.P., Bhangoo, J.S., Clark, P.E., Murphy, M.E., and Killen, R. (2001) X-ray fluorescence measurements of the surface elemental composition of asteroid 433 Eros, *Meteoritics & Planetary Science* 36, 1673-1695 https://doi.org/10.1111/j.1945-5100.2001.tb01856.x

Noguchi, T., Kimura, M., Hashimoto, T., Konno, M., Nakamura, T., Zolensky, M. E., Okazaki, R., Tanaka, M., Tsuchiyama, A., Nakato, A., Ogami, T., Ishida, H., Sagae, R., Tsujimoto, S., Matsumoto, T., Matsuno, J., Fujimura, A., Abe, M., Yada, T., Mukai, T., Ueno, M., Okada, T., Shirai, K., and Ishibashi, Y. (2014) Space weathered rims found on the surfaces of the Itokawa dust particles, *Meteoritics & Planetary Science* 49, 188-214

Oberbeck V. R., and W. L. Quaide (1968) Genetic implications of lunar regolith thickness variations, *Icarus* 9, 446-465.

Ockert-Bell, M. E., Clark, B. E., Shepard, M. K., Isaacs, R. A., Cloutis, E. A., Fornasier, S., and Bus, S. J. (2010), The composition of M-type asteroids: Synthesis of spectroscopic and radar observations, *Icarus* 210 p. 674-692

Oran, R., Wiess, B. P., and Cohen, O. (2018) Were chondrites magnetized by the early solar wind? *Earth and Planetary Science Letters* 492, 222-231 https://doi.org/10.1016/j.epsl.2018.02.013

Ostro, S. J. (1993) Planetary Radar Astronomy, *Reviews of Modern Physics* 65, 1235-1279

Papike, J.J., Simon, S.B., and Laul, J.C. (1982), The lunar regolith: Chemistry, mineralogy, and petrology, *Reviews of Geophysics* 20, p. 761-826

Paris, P. and Erdogan, F. (1963) A Critical Analysis of Crack Propagation Laws, *Journal of Basic Engineering* 85, 528-533 doi:10.1115/1.3656900

Pätzold, M., Andert, T. P., Asmar, S. W., Anderson, J. D., Barriot, J. P., Bird, M. K., Hausler, B., Hahn, M., Tellman, S., Sierks, H., Lamy, P., and Weiss, B. P. (2011) Asteroid 21 Lutetia: Low Mass, High Density, *Science* 334, p. 491-492

Payne, B. P., Biesinger, M. C. and McIntyre, N. S. (2011) X-ray photoelectron spectroscopy studies of reactions on chromium metal and chromium oxide surfaces, *Journal of Electron Spectroscopy and Related Phenomena* 184, 29-37

Peplowski, P.N., Lawrence, D.J., Beck, A.W., Burks, M., Chabot, N.L., Goldsten, J.O., Wilson, J., Yokley, Z, and the Psyche Science Team. (2018) Nuclear Spectroscopy of Asteroid 16 Psyche, Presented at *Lunar and Planetary Science Conference XLIX* Abstract #2114

Petch, N. J. (1953) The Cleavage Strength of Polycrystals, *Journal of the Iron and Steel Institute* 174, p. 25-28

Petch, N. J. (1958) The ductile-brittle transition in the fracture of α-iron: I, *Philosophical Magazine* 3, https://doi.org/10.1080/14786435808237038

Petrovic, J.J. (2011) Mechanical properties of meteorites and their constituents, *Journal of Materials Science* 36, 1579-1583

Pieters, C.M., Taylor, L.A., Noble, S.K., Keller, L.P., Hapke, B., Morris, R.V., Allen, C.C., McKay, D.S., and Wentworth, S. (2000) Space weathering on airless bodies: Resolving a mystery with lunar samples, *Meteoritics & Planetary Science* 35, 1101-1107

Pinos, J., Mikmekova, A., and Frank, L. (2017) About the information depth of backscattered electron imaging, *Journal of Microscopy* 226, 335-342

Porneala and Willis (2006) Effect of the dielectric transition on laser-induced phase explosion in metals, *International Journal of Heat and Mass Transfer* 49, 1928-1936

Powell, C.J., Jablonski, A. (2010) NIST Electron Inelastic-Mean-Free-Path Database, *NIST Standard Reference Database 71* v. 1.2

Prince, B. S., Magnuson, M. P., Chaves, L. C., Thompson, M. S., & Loeffler, M. J. (2020). Space weathering of FeS induced via pulsed laser irradiation. *Journal of Geophysical Research: Planets*, 125, e2019JE006242. https://doi.org/10.1029/2019JE006242

Qiu, H., Hanamura, T., and Torizuka, S. (2014). Influence of Grain Size on the Ductile Fracture Toughness of Ferritic Steel, *ISIJ International* 54, 1958–1964.

Raines, J.M., Gershman, D.J., Zurbuchen, T.H., Sarantos, M., Slavin, J.A., Gilbert, J.A., et al. (2013) Distribution and compositional variations of plasma ions in Mercury's space environment: the first three Mercury years of MESSENGER observations. *Journal of Geophysical Research – Space Physics*, 118, 1604-1619

Remo, J.L. and Johnson, A.A. (1974) The ductile-brittle transition in meteoritic irons, *Meteoritics* 9, 209-213

Remo, J.L., and Johnson, A.A. (1975) A preliminary study of the ductile-brittle transition under impact conditions in material from an octahedrite, *Journal of Geophysical Research* 80

Ringwood, A.E. (1960) Cohenite as a pressure indicator in iron meteorites, *Geochimica et Cosmochimica Acta* 20, p. 155-158

Rivkin, A.S., Howell, E.S., Lebofsky, L.A., Clark, B.E., and Britt, D.T. (2000) The nature of M-class asteroids from 3-µm observations, *Icarus* v. 145, p. 351-368

Robin, B. (1966) Cohenite in Meteorites: A Proposed Origin, *Science* 153, p. 60-62

Rossman, G. R., & Ehlmann, B. L. (2020). Electronic Spectra of Minerals in the Visible and Near-Infrared Regions. *Remote Compositional Analysis: Techniques for Understanding Spectroscopy*, 3-20.

Roth J. (1983) Chemical sputtering. In: Behrish R. (eds) *Sputtering by Particle Bombardment II. Topics in Applied Physics*, v 52. Springer, Berlin, Heidelberg. https://doi.org/10.1007/3-540-12593-0_3

Roth, J., Bohdansky, _., and W. Otternberger, Report IPP 9/26 (1979) Max Planck Institut fur Plasmaphysik, Garching, FRG Sanchez, J.A., Reddy, V., Shepard, M.K., Thomas, C., Cloutis, E.A., Takir, D., Contrad, A., Kiddell, C., and Applin, D. (2017) Detection of rotational spectral variation on the M-type asteroid (16) Psyche, *The Astronomical Journal* v. 153, p. 1-8

Sabins, F. F. (1997) *Remote Sensing*, 3rd Edition, Waveland Press, Long Grove, IL

Sagy, A., Fineberg, J., and Reches, Z. (2004) Shatter cones: Branched, rapid fractures formed by shock impact. *Journal of Geophysical Research: Solid Earth* 109

Sandor, B.I. (1972) *Fundamentals of Cyclic Stress and Strain*, University of Wisconsin Press, Madison, WI

Sasaki, S., Nakamura, K., Hamabe, Y., Kurahashi, E., and Hiroi, T. (2001) Production of iron nanoparticles by laser irradiation in a simulation of lunar-like space weathering, *Nature* 410, 555-557

Schaible, M. J., and Baragiola, R. A. (2014), Hydrogen implantation in silicates: The role of solar wind in SiOH bond formation on the surfaces of airless bodies in space, *Journal Geophysical Research Planets* 119, 2017–2028

Schaible, M. J., Dukes, C. A., Hutcherson, A. C., Lee, P., Collier, M. R., & Johnson, R. E. (2017). Solar wind sputtering rates of small bodies and ion mass spectrometry detection of secondary ions, *Journal of Geophysical Research: Planets* 122, 1968– 1983. https://doi.org/10.1002/2017JE005359

Schaible, M. J., Pinto, H. P., McKee, A. D., Leszczynsky, J., and Orlando, T. M. (2019) Characterization and Simulation of Natural Pyrite Surfaces: A Combined Experimental and Theoretical Study. *Journal of Physical Chemistry* 123, 26397-26405, https://doi.org/10.1021/acs.jpcc.9b07586

Scherzer, B.M.U. (1983) Development of Surface Topography dues to Gass ion Implantation, in *Sputtering by Particle Bombardment II*, ed. R. Behrisch, Springer-Verlag: New York

Schiller, M., Baker, J., Creech, J., Paton, C., Millet, M-A., Irving, A., and Bizzarro, M. (2011) Rapid Timescales for Magma Ocean Crystallization on the Howardite-Eucrite-Diogenite Parent Body, *The Astrophysical Journal Letters* 740

Schläppi, B., Altwegg, K., and Wurz, P. (2008) Asteroid exosphere: A simulation for the ROSETTA flyby targets (2867) Steins and (21) Lutetia, *Icarus* 195, 674-685

Schmitz, J., Mutzke, A., Litnovsky, A., Klein, F., Tan, X.Y., Wegener,T., Hansen, P., Aghdassi, N., Eksaeva, A., Rasinski, M., Kreter, A. J., Gonzalez-Julian, J., Coenen, J. W., Linsmeier, Ch., and Bram, M. (2019) Preferential sputtering induced Cr-Diffusion during plasma exposure of WCrY smart alloys, *Journal of Nuclear Materials* 526, 151767

Schröder, S. E., Keller, H. U., Mottola, S., Scholten, F., Preusker, F., Matz, K. D., and Hviid, S. (2015) Variegation and space weathering on asteroid 21 Lutetia, *Planetary and Space Science* 117, p. 236-245

Shabanova, I. N. and Trapeznikov, V. A. (1975) A study of the electronic structure of Fe3C, Fe3Al and Fe3Si by photoelectron spectroscopy, *Journal of Electron Spectroscopy and Related Phenomena* 6, 297-307

Shepard, M. K., Richardson, J., Taylor, P. A., Rodrigues-Ford, L. A., Conrad, A., de Pater, I., Adamkovics, M., de Kleer, K., Males, J. R., Morzinski, K. M., Close, L. M., Kaaasalainen, M., Viikinkoski, M., Timerson, B., Reddy, V., Magri, C., Nolan, M. C., Howell, E. S., Benner, L. A. M., Giorgini, J. D., Warner, B. D., and Harris, A. W. (2017) Radar observations and shape model of asteroid 16 Psyche, *Icarus* 281 p. 388-403

Shirley, D.A. (1972) High-Resolution X-Ray Photoemission Spectrum of the Valence Bands of Gold *Physical Review B* 5, 4709

Shoemaker, E.M., Batson, R.M., Hold, H.E., Morris, E.C., Rennilson, J.J., and Whitaker, E.A. (1967) Surveyor V: Television pictures, *Science* 158, p. 642-652

Sinha, S. and Mukherjee, M. (2018) A study of adventitious contamination layers on technically important substrates by photoemission and NEXAFS spectroscopies, *Vacuum* 148, 48-53

Skala, R., Cosarova, I., and Drabek, M. (2006) Inversion twinning in troilite, *American Mineralogist* 91, 917-921

Skinner, W. M., Nesbitt, W. H., and Pratt, A. R. (2004) XPS identification of bulk hole defects and itinerant Fe 3d electrons in natural troilite *Geochimica et Cosmochimica Acta* 68, 2259–2263

Smith, C.S. (1948) Grains, Phases, and Interfaces: An Interpretation of Microstructure, *Institute of Materials Division Meeting*, New York

Stadlmayr, R. et al. (2018). Fluence dependent changes of surface morphology and sputtering yield of iron: Comparison of experiments with SDTrimSP-2D. *Nuclear Instruments and Methods in Physics Research Section B: Beam Interactions with Materials and Atoms* 430, 42-46. doi:10.1016/j.nimb.2018.06.004.

Starukhina, L.V. (2001) Water detection on atmosphereless celestial bodies: Alternative explanations of the observations, *Journal of Geophysical Research* 106, 14,701-14,710

Stickle, A. M., DeCoster, M. E., Graninger, D. M., Kumamoto, K. M., Owen, J. M., Rainey, E. S. G., Syal, M. B., Barnouin, O. S., Chabot, N. L., Cheng, A. F., Collins, G. S., Daly, R. T., Davison, T. M., Dotto, E., Ernst, C. M., Fahenstock, E. G., Ferrari, F., Hirabayashi, T., Karatekin, O., Luccetti, A., Luther, R., Marchi, S., Mitra, N., Pajola, M., Parro, L. M., Pearl, J., Ramesh, K. T., Rivkin, A. S., Rossi, A., Sanchez, P., Senel, C. B., Schwartz, S. R., Tusberti, F., Wunnemann, K., Zhang, Y., and The DART Investigation Team (2023) Dimorphos's Material Properties and Estimates of Crater Size from the DART Impact, *Lunar and Planetary Science Conference LIV*, Abstract #2563

Szabo, P. S. et al. (2018) Solar wind sputtering of wollastonite as a lunar analogue material – Comparisons between experiments and simulations. *Icarus*, 314, 98-105

Szabo, P. S. et al. (2020a). Dynamic Potential Sputtering of Lunar Analog Material by Solar Wind Ions. *The Astrophysical Journal* 891, 100

Szabo, P. S., Biber, H., Jäggi, N., Wappl, M., Stadlmayr, R., & Primetzhofer, D., et al. (2020b). Experimental insights into space weathering of phobos: laboratory investigation of sputtering by atomic and molecular planetary ions. *Journal of Geophysical Research: Planets*, 125, e2020JE006583. https://doi.org/10.1029/2020JE006583

Taglauer, E. and Heiland, W. (1976) Surface analysis with low energy ion scattering, *Applied Physics* 9, 261–275

Takir, D., Reddy, V., Sanchez, J. A., Shepard, M. K., and Emery, J. P. (2017) Detection of Water and/or Hydroxyl on Asteroid (16) Psyche, *The Astronomical Journal* 153 p. 31

Tanyeli, I., Marot, L., Mathys, D., van de Sanden, M.C.M, and De Temmerman, G. (2015) Surface Modification Induced by High Fluxes of Low Energy Helium Ions, *Scientific Reports* 5, 1-9

Terranova, U., Mitchell, C., Sankar, M., Morgan, D., and de Leeuw, N. H. (2018) Initial oxygen incorporation in the prismatic surfaces of troilite FeS, *Journal of Physical Chemistry* 122, 12810-12818

Tholen, D. J. (1984) *Asteroid Taxonomy from Cluster Analysis of Photometry*, PhD Dissertation, The University of Arizona

Thomas, J. E., Skinner, W. M., and Smart, R. (2003) A comparison of the dissolution behavior of troilite with other iron(II) sulfides; implications of structure, *Geochimica et Cosmochimica Acta* 67, 831–843

Thompson, M.S., Zega, T.J., and Howe, J.Y. (2017) In situ experimental formation and growth of Fe nanoparticles and vesicles in lunar soil, *Meteoritics & Planetary Science* 52, 413-427 https://doi.org/10.1111/maps.12798

Thompson, M.S., Loeffler, M.J., Morris, R.V., Keller, L.P., and Christoffersen, R. (2019) Spectral and chemical effects of simulated space weathering of the Murchison CM2 carbonaceous chondrite, *Icarus* 319, 499-511

Thompson, M.S., Loeffler, M.J., Morris, R.V., Keller, L.P., and Christoffersen, R. (2019) Spectral and chemical effects of simulated space weathering of the Murchison CM2 carbonaceous chondrite, *Icarus* 319, 499-511

Tosi, F., Carrozzo, F.G., Raponi, A., De Sanctis, M.C., Thangjam, G., Zambon, F., Ciarniello, M., Nathues, A., Capria, M.T., Rognini, E., Ammannito, E., Hoffmann, M., Krohn, K., Longobardo, A., Palomba, E., Pieters, C.M., Stephan, K., Raymond, C.A. and Russell, C.T. (2018), Mineralogy and temperature of crater Haulani on Ceres. *Meteoritics and Planetary Science*, 53: 1902-1924

von Toussaint, U.; Mutzke, A.; Sugiyama, K., and Schwarz-Selinger, T. (2016) Simulation of coupled sputter-diffusion effects. *Physica Scripta* T167, 014023

Tsuchiyama, A., Uesugi, M., Matsushima, T., Michikami, T., Kadono, T., et al. (2011) Three-Dimensional Structure of Hayabusa Samples: Origin and Evolution of Itokawa Regolith, *Science* 333, p. 1125-1128

Ueki, S., Mine, Y., and Takashima, K. (2021) Excellent mechanical properties of taenite in meteoric iron, *Scientific Reports* 11

Vernazza, P., Brunetto, R., Binzel, R. P., Perron, C., Fulvio, D., Strazzulla, G., and Fulchignoni, M. (2009) Plausible parent bodies for enstatite chondrites and mesosiderites: Implications for Lutetia's fly-by, *Icarus* 202, p. 477-486

Veverka J., Thomas, P. C., Robinson, M., Murchie, S., Chapman, C., Bell, M., Harch, A., Merline, W. J., Bell, J. F., Busey, B., Carcich,, B., Cheng, A., Clark, B., Domingue, D., Dunham, D., Farquhar, R., Gaffey, M. J., Hawkins, E., Izenberg, N., Joseph, J., Kirk, R., Li, H., Lucey, P., Malin, M., McFadden, L., Miller, J. K., Owen, W. M., Peterson, C., Prockter, L., Warren, J., Wellnitz, D., Williams B. G., and Yeomans, D. K. (2001) Imaging of small-scale features on 433 Eros from NEAR: Evidence for a complex regolith, *Science*, 292, 484-488

Wagner, C.D., Davis, L.E., Zeller, M.V., Taylor, J.A., Raymond, R.H. and Gale, L.H. (1981), Empirical atomic sensitivity factors for quantitative analysis by electron spectroscopy for chemical analysis. *Surface and Interface Analysis* 3, 211-225. https://doi.org/10.1002/sia.740030506

Walsh, K. J., Jawin, E. R., Ballouz, R. L., Barnouin, O. S., Bierhaus, E. B., Connolly, H. C., Molaro, J. L., McCoy, T. J., Delbo, M., Hartzell, C. M., Pajola, M., Schwartz, S. R., Trang, D., Asphaug, E., Becker, K. J., Beddingfield, C. B., Bennett, C. A., Bottke, W. F., Burke, K. N., Clark, B. C., Daly, M. G., DellaGiustina, D. N., Dworkin, J. P., Elder, C. M., and The OSIRIS-REx Team (2019) Craters, boulders, and regolith of (101955) Bennu indicative of an old and dynamic surface, *Nature Geoscience* 12, 242-246

Wasson, J. T. (1967) *Geochimica et Cosmochimica Acta* 31, p. 161-180

Wasson, J. T. (1998) *Geochimica et Cosmochimica Acta* 62, p. 715-724

Wasson, J. T. (1999) *Geochimica et Cosmochimica Acta* 63, p. 2875-2889

Wasson, J. T. (2012) Vesta, iron meteorites from extensively differentiated asteroids, and the provenance of the HED meteorites, *Lunar and Planetary Science Conference XLIII*

Wasson, J. T. and Richardson, J. W. (2001) *Geochimica et Cosmochimica Acta* 65, p. 951-970

Wasson, J. T. and Wang, J. (1986) *Geochimica et Cosmochimica Acta* 50, p. 725-732

Watson, E. B.; Cherniak, D. J.; Frank, E. A. (2009) *Geochimica Cosmochimica Acta* 73, 4792

Weisburg, M. K. et al. (2006) in *Meteorites and the Early Solar System I*: eds D. Lauretta and H. Y. McSween, University of Arizona Press, Tucson, AZ, p. 19-52

Weiss, B. P., Elkins-Tanton, L. T., Barucci, M. A., Sierks, H., Snodgrass, C., Vincent, J. B., Marchi, S., Weissman, P. R., Pätzold, M., Richter, I., Fulchignoni, M., Binzel, R. P., and Schulz, R. (2012) Possible evidence for partial differentiation of asteroid Lutetia from Rosetta, *Planetary and Space Science* 66, p. 137-146

Wilcox, B. B., M. S. Robinson, P. C. Thomas, B. R. Hawke (2005) Constraints on the depth and variability of the lunar regolith, *Meteoritics and Planetary Science*, 40, 695-710

Wirtz, T., De Castro, O., Audinot, J. N., and Philipp, P. (2019) Imaging and Analytics on the Helium Ion Microscope, *Annual Review of Analytical Chemistry* 12

Wittmaack, K., & Mutzke, A. (2017). Highly accurate nuclear and electronic stopping cross sections derived using Monte Carlo simulations to reproduce measured range data. *Journal of Applied Physics* 121, 105104. doi:10.1063/1.4978016.

Wu, Y., Li, X., Yao, W., and Wang, S. (2017) Impact Characteristics of Different Rocks in a Pulsed Laser Irradiation Experiment: Simulation of Micrometeorite Bombardment on the Moon. *Journal of Geophysical Research: Planets*, 122, 1956-1967. https://doi.org/10.1002/2016JE005220

Yamamura, Y. and Tawara, H. (1996) Energy Dependence Of Ion-Induced Sputtering Yields From Monatomic Solids At Normal Incidence, *Atomic Data and Nuclear Data Tables*, v. 62, p. 149-253Yang, J.C., Pitts, W.M., Fernandez, M., and Prasad, K. (2013) Measurements of Effective Diffusion Coefficients of Helium and Hydrogen through Gypsum, *International Journal of Hydrogen Energy* 38, 8125-8131

Yang, J. and Goldstein, J. I. (2003). The mechanism for the formation of the Widmanstätten structure in low P iron meteorites, *Meteoritics & Planetary Science* 38, A33.

Yang, J. and Goldstein, J. I. (2005) The formation of the Widmanstätten structure in meteorites, *Meteoritics and Planetary Science* 40, p. 239-253

Yang, J. and Goldstein, J. I. (2006) Metallographic cooling rates of the IIIAB iron meteorites, *Geochimica et Cosmochimica Acta* 70, p. 3197-3215

Yang, C. W., Williams, D. B., and Goldstein, J. I. (1996) A revision of the Fe-Ni phase diagram at low temperature. *Journal of Phase Equilibria* 17, p. 522-531

Yang, J., Goldstein, J. I., and Scott, E. R. D. (2010) Main-group pallasites: Thermal history, relationship to IIIAB irons, and origin, *Geochimica et Cosmochimica Acta* 74, p. 4471-4492

Yao Y., Hargitai, Z., Albert, M., Albridge, R.G., Barnes, A.V., Gilligan, J.M., Pratt Ferguson, B., Lüpke, G., Gordon, V.D., and Tolk, N.H. (1998) New Molecular Collisional Interaction Effect in Low-Energy Sputtering, *Physical Review Letters* 81, 550

Yokota, Y., Honda, R., Tatsumi, E., Domingue, D., Schröder, Matsuoka, M., Morota, T., Sakatani, N., Kameda, S., and Kouyama, T. (2021) Opposition Observations of 162173 Ryugu: Normal Albedo Map Highlights Variations in Regolith Characteristics, *The Planetary Science Journal* 2, 177

Yon, S. A. and Pieters, C. M. (1987) Interactions of light with rough dielectric surfaces – Spectral reflectance and polarimetric properties. Proceedings, *Lunar & Planetary Science Conference XVIII*, 581-592

Zellner, B. (1973) Polarimetric Albedos of Asteroids, *Bulletin of the American Astronomical Society* 5, p. 388

Zellner, B. and Gradie, J. (1976) Minor planets and related objects. XX. Polarimetric evidence for the albedos and compositions of 94 asteroids. *Astronomical Journal* 81, 262-280

Zhang, L.; Tang, G.; Ma, X., (2010) Long range effect of ion irradiation on diffusion, *Physics Letters A*, 374, 2137-2139.

Zhu, C., Góbi, S., Abplanalp, M. J., Frigge, R., Gillis-Davis, J. J., & Kaiser, R. I. (2019). Space weathering-induced formation of hydrogen sulfide (H_2S) and hydrogen disulfide (H_2S_2) in the murchison meteorite. *Journal of Geophysical Research: Planets*, 124, 2772– 2779.

Ziegler, J. F., Biersack, J. P., and Ziegler, M. D. (1985) *SRIM – The Stopping and Range of Ions in Solids*, SRIM Co.: Chester, MD

Zurbuchen, T.H., Raines, J.M., Gloeckler, G., Krimigis, S.M., Slavin, J.A., Koehn, P.L., et al. (2008) MESSENGER observations of the composition of Mercury's ionized exosphere and plasma environment. *Science,* 321, 90-92

APPENDIX A

COAUTHOR PERMISSIONS FOR CHAPTER 2

In accordance with the Arizona State University Graduate College's policy on using previously published work in a culminating experience document, I affirm that all coauthors of (Christoph et al. 2022) have granted permission for this paper to be used as CHAPTER 2 and for its supporting information to be used as APPENDIX B in this dissertation. The policy may be read in full at the following link: https://graduate.asu.edu/sites/default/files/policy-on-using-previously-published-work.pdf

APPENDIX B

SUPPORTING INFORMATION FOR CHAPTER 2

Journal of Geophysical Research - Planets

Supporting Information for

Space weathering effects in troilite by simulated solar-wind hydrogen and helium ion irradiation

Christoph*, J. M.[1]; Minesinger, G. M.[2]; Bu, C.[2,3]; Dukes, C. A.[2]; and Elkins-Tanton, L. T.[1]

[1]School of Earth and Space Exploration, Arizona State University, Tempe, AZ 85287

[2] Laboratory for Astrophysics and Surface Physics, University of Virginia, Charlottesville, VA 22904

[3] Columbia Astrophysics Laboratory, Columbia University, New York, NY 10027

Contents of this file

Introduction

Text S1 to S5

Figures S1 to S7

Introduction

The material included here represents additional details of our methods (Text S1 to S5) and data (Figures S1 to S7) which are extraneous to the main text of the paper, but which may be of interest for other readers, particularly those desiring to compare our techniques and results to other similar work.

Text S1. Irradiation Instrument Details

We irradiated the Toluca sample at ultra-high vacuum (UHV) in the PHI 560 with a base pressure of ~10^{-10} Torr (Fig. S1-top). To simulate the solar wind, we performed an initial irradiation with 4 keV He^+ to 6 × 10^{16} He^+ cm^{-2}, followed by irradiation with 2 keV H_2^+ to 2.8 × 10^{18} cm^{-2}. All ions were produced (separately) in the same electron-bombardment ion source using either He or H_2 gas of purity > 99.999%; for protons the source was held at a potential of 2 keV, so that upon approach to the surface the H_2 molecule separates into two 1 keV H components (Dukes et al. 1999). The ion beam was rastered for uniformity over an area of 8 × 8 mm^2 at normal incidence. The average ion flux was (1.1 ± 0.1) ×10^{13} He^+ cm^{-2} s^{-1} and (2.2 ± 0.2) ×10^{13} H^+ cm^{-2} s^{-1}, measured by a Faraday-cup mounted

adjacent to the sample before and after each irradiation. A dual-anode (Al/Mg) X-ray source and a double-pass, cylindrical-mirror electron energy analyzer (CMA) on the PHI 560 allowed us to perform in-situ XPS measurements. We took XPS survey spectra at pass energy of 200 eV at binding energies of 1 – 1350 eV, as well as high-resolution (HR) XPS spectra at a pass energy of 30 eV for photoelectrons: Fe-2p, O-1s, S-2p, and C-1s. The X-ray analysis covers an area with a diameter of ~6 mm, well within the irradiated region

We irradiated the Canyon Diablo sample at normal incidence with 4 keV He^+ using a floating-column low-energy ion gun on the Versaprobe III (Fig. S1-bottom) at an average flux of 1.3×10^{13} He^+ cm^{-2} s^{-1}. The beam was rastered over an area of 3×3 mm^2. Base pressure in the Versaprobe III was 5×10^{-11} Torr; irradiation and analysis pressures reached 8×10^{-9} Torr due to the increased partial pressure of helium. We measured ion-beam current density on a separate Faraday cup before and after the experiment, using average flux to determine the fluences. The Versaprobe III is a high-resolution, imaging XPS microprobe, equipped with a monochromated Al-Kα source and spherical capacitor analyzer (SCA) for improved energy resolution. Surveys for elemental analysis used a pass energy of 140 eV, while high-resolution spectra for chemical analysis used a pass energy of 55 eV. At the first two fluence steps, we took XPS data on six separate locations within the irradiation area using a 200 μm X-ray beam spot to locate the center of the ion beam, then selected two locations as close as possible to the center for subsequent fluence steps. Survey spectra as a function of 4 keV He^+ fluence for Point 6 are shown in Fig. S1 as an example, where spectra are vertically shifted for clarity. Surface spectra are utilized for compositional analysis.

Text S2. XPS Analysis Methodology and Sensitivity Factors

Analysis of both the XPS survey and higher energy-resolution (HR) data for the Toluca sample acquired on the PHI 560 was done by integrating the peak area using CasaXPS after Shirley background subtraction. Because the X-ray source on this instrument is non-monochromatic, quantification was accomplished after X-ray satellite subtraction, using the Fe-3p, S-2p, O-1s, C-1s, Ca-2p, and N-1s features. No other elements were identified in the Toluca near-surface. The Fe-3p photoelectron peak was used for quantification rather than the more prominent Fe-2p, since the Fe-3p is a better match the information depth between the Fe and S, and because the Fe-3p feature background is more easily modeled than the frequently used Fe-2p feature, improving the reliability and repeatability of the analysis (e.g. Fig. S2). Loeffler et al. (2008) did not report a new sensitivity factor for the Fe-3p, thus we used sensitivity factors provided by the manufacturer for the Model 560 double-pass cylindrical mirror analyzer [C1s: 0.25; O1s: 0.66; Fe3p: 0.26; and S2p: 0.54] (Wagner et al. 1981) for compositional analysis of Toluca. These sensitivity factors were used previously for the olivine concentration analysis in Dukes et al. (1999).

The Versaprobe III XPS, used for Canyon Diablo measurements, was equipped with an X-ray monochromator, eliminating the requirement for X-ray satellite removal during analysis. The spherical capacitor analyzer with input lens has a different geometry and electron transmission function, necessitating the use of a different set of sensitivity factors which were provided by the manufacturer [C1s: 0.25; O1s: 0.58; Fe3p: 0.31; and S2p: 0.65]. PHI Multipak v9.8 was used for peak area determination after Shirley background subtraction, in a manner similar to the Toluca analysis.

Text S3. XPS Compositional Errors

Error bars for XPS measurements were derived from (1) experimental/sampling variation and (2) data analytical methodologies, subsequently added in quadrature. Sampling error was determined by comparison of elemental compositional differences between two nearby points for multiple ion fluences, resulting in measurement variations of: 4.16% (O), 8.32% (S), 2.73% (Fe), and 54.51% (C) for the Versaprobe data and 4.99% (O), 13.30% (S), 7.05% (Fe), and 35.33% (C) for the PHI 560 data. For all elements except for C, sampling was not the dominant source of error and did not strongly impact the S:Fe measurements. Analytical error was determined by comparing compositional results using different background models, a variety of photoelectron peaks (Fe-2p, Fe-2p3/2, and Fe-3p), and different sensitivity factors for the PHI 560 (Wagner et al. 1981 vs. Loeffler et al. 2008); only the manufacturer sensitivity factors were available for the Versaprobe, where accuracy was confirmed with fractured, minimally-oxidized pyrite (Fe:S = 0.5). Analytical errors were combined to 14.59% (O), 15.53% (S), 14.83% (Fe), and 16.98% (C) for Versaprobe data, and 25.46% (O), 26.98% (Fe), 25.44% (S), and 25.31% (C) for measurements taken on the PHI 560. The increased error with the PHI 560 was due to the inclusion of the two sets of sensitivity factors. We note that these error bars are included in Figs. 3, 5, 6, 7, and S4.

Text S4. SDTRIMSP running parameters

These simulations were run in dynamic mode on 10 – 32 parallel processors depending on the fluence (32 processors at the largest fluence), which is defined in units of (1016 atoms/cm2). The parameter NH (number of target compositional updates) was modified so that fluence/NH was on the order of 0.01 (10^{14} atoms/cm2). For the best statistics, the parameter NR (number of projectiles between target updates) was set between 1000 to 10,000. Note that NR is independent of the real flux and fluence, and influences only the nature of the target compositional updates. For a fluence of 3.6×10^{18} ions/cm^2, NH=10,000 and NR=1,000 in the He^+ and H^+ irradiation studies. Sputtering studies at low fluences relevant to Psyche required NR=10,000.

Text S5. Description of SDTrimSP Diffusion Calculation

The dynamic version of SDTrimSP employs Fick's laws to describe the diffusion of unbound target atoms toward the surface as a function of depth (x) and fluence (φ), where φ = flux (k) × time (t), and the atomic concentration C(x) within a narrow volume at x is:

$$C(x) = \frac{N(x)}{A \times \Delta x} \tag{2}$$

where N(x) is the number of atoms within a thin slice Δx over an area A. With the use of Fick's first law, variation in concentration over a short time can be considered in terms of changing flux (J):

$$\frac{C(t+dt) - C(t)}{\Delta t} = -\frac{J(x+dx) - J(x)}{(\Delta x)} \tag{3}$$

$$\frac{\partial J(x)}{\partial x} = D_T \times \frac{\partial}{\partial x}\left(\frac{\partial C(x)}{\partial x}\right) = D_T \times \frac{\partial^2 C(x)}{\partial x^2} \tag{4}$$

And adapted to:

$$\frac{\partial C(t)}{\partial \varphi\,(t)} = \frac{\partial C(t)}{\partial t} \times \frac{\partial t}{\partial \varphi\,(t)} = \frac{\partial C(t)}{\partial t} \div k \; = \frac{D_T}{k} \times \frac{\partial^2 C(x)}{\partial x^2} = \; \eta_T \times \frac{\partial^2 C(x)}{\partial x^2} \tag{5}$$

where η_T is the flux-dependent diffusion coefficient output by SDTrimSP in units of Å^4/atom. Thus, the extrapolated sulfur diffusion coefficient was multiplied by the flux of sulfur through the target (in units of atoms/Å^2/s), before comparison with previously published D_T values. Outgassing of projectile ions (H^+, He^+) in SDTrimSP 6.0 is modeled on the basis of equation (5). Additional detail can be found in the SDTrimSP manual and recent publications (Mutzke et al. 2019; von Toussaint et al. 2016; and Schmitz et al. 2019).

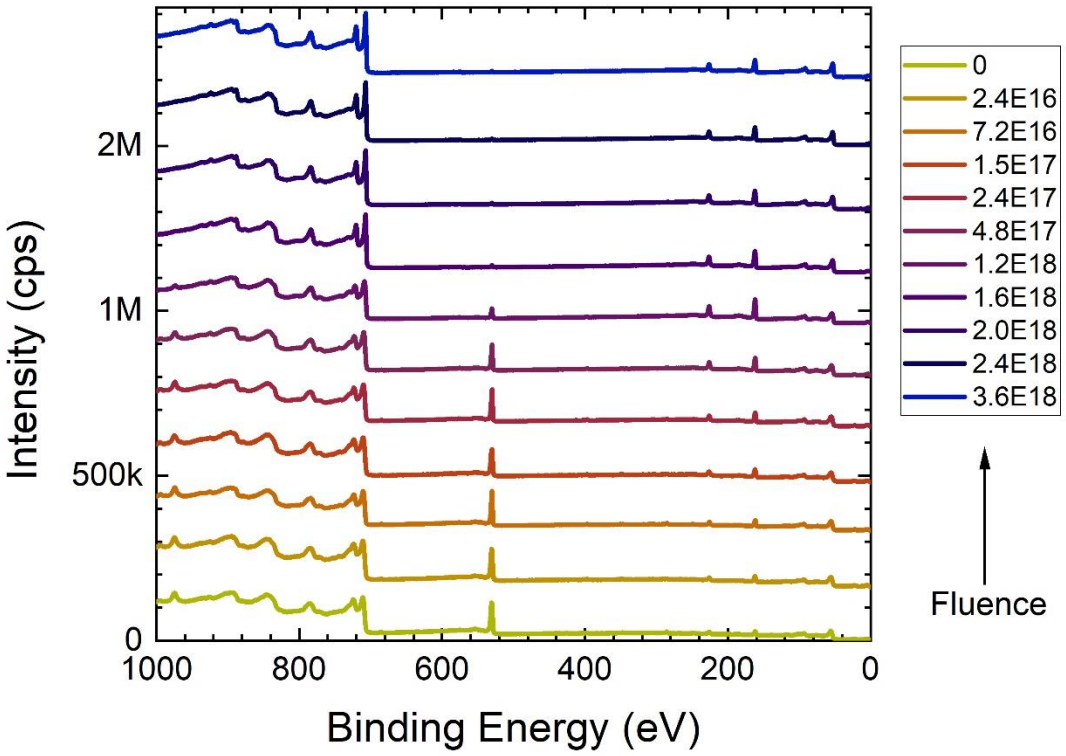

Figure S1: *XPS Survey spectra collected on the Versaprobe III were used to determine surface composition of the Canyon Diablo sample as a function of fluence (legend in units of He^{+} cm^{-2}). Spectral composition in Figure 3a was derived from this data, acquired at Point 6, as described in S2.*

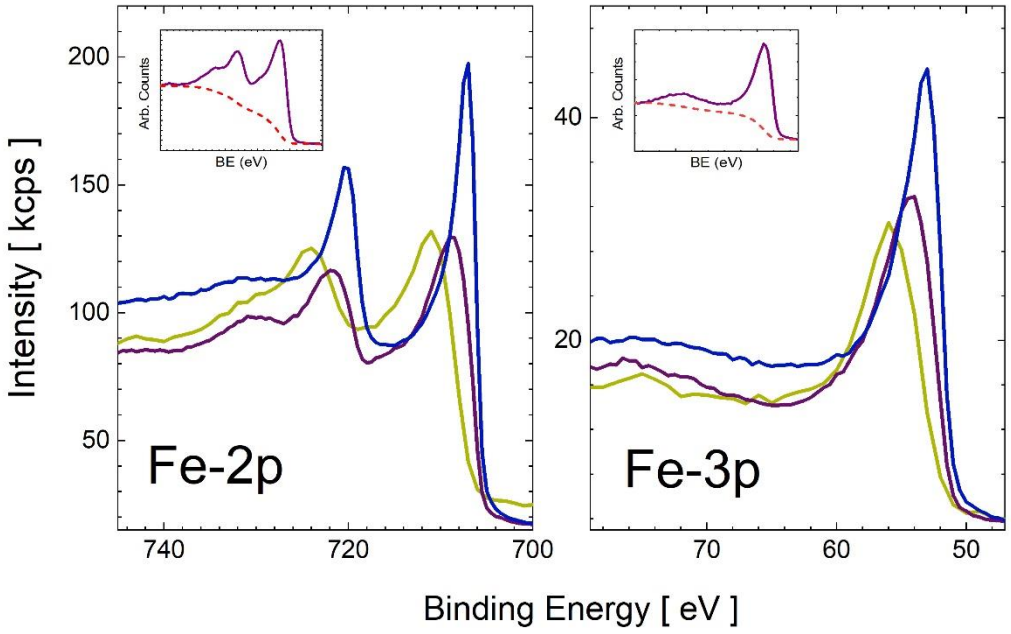

Figure S2: *For XPS compositional analysis of FeS, the Fe-3p photoelectron features were used for quantification, rather than the more prominent Fe-2p features. Analyses were done in this manner for two reasons: (1) the Fe-3p photoelectron kinetic energy is ~100 eV from the S-2p, ensuring a similar information depth which gives more meaningful concentration comparisons; (2) the multiplet structure of the Fe-2p spin-orbit couplet with shake satellite structure (*left panel*) is significantly more complex than for the Fe-3p feature (*right panel*); difficulty in separation of intrinsic and extrinsic features, along with significant variation in modeling of the inelastic background structure with end-point selection, increased error in quantification. Illustrations of the iterated Shirley background simulation are shown in the inset figures for the Fe-2p (*left*) and Fe-3p (*right*) photoelectron features, based on recommendations outlined in Bagus et al. (2021). Representative spectra shown are for 0, 1.2 x 10^{18}, and 3.6 x 10^{18} He^{+} cm^{-2}.*

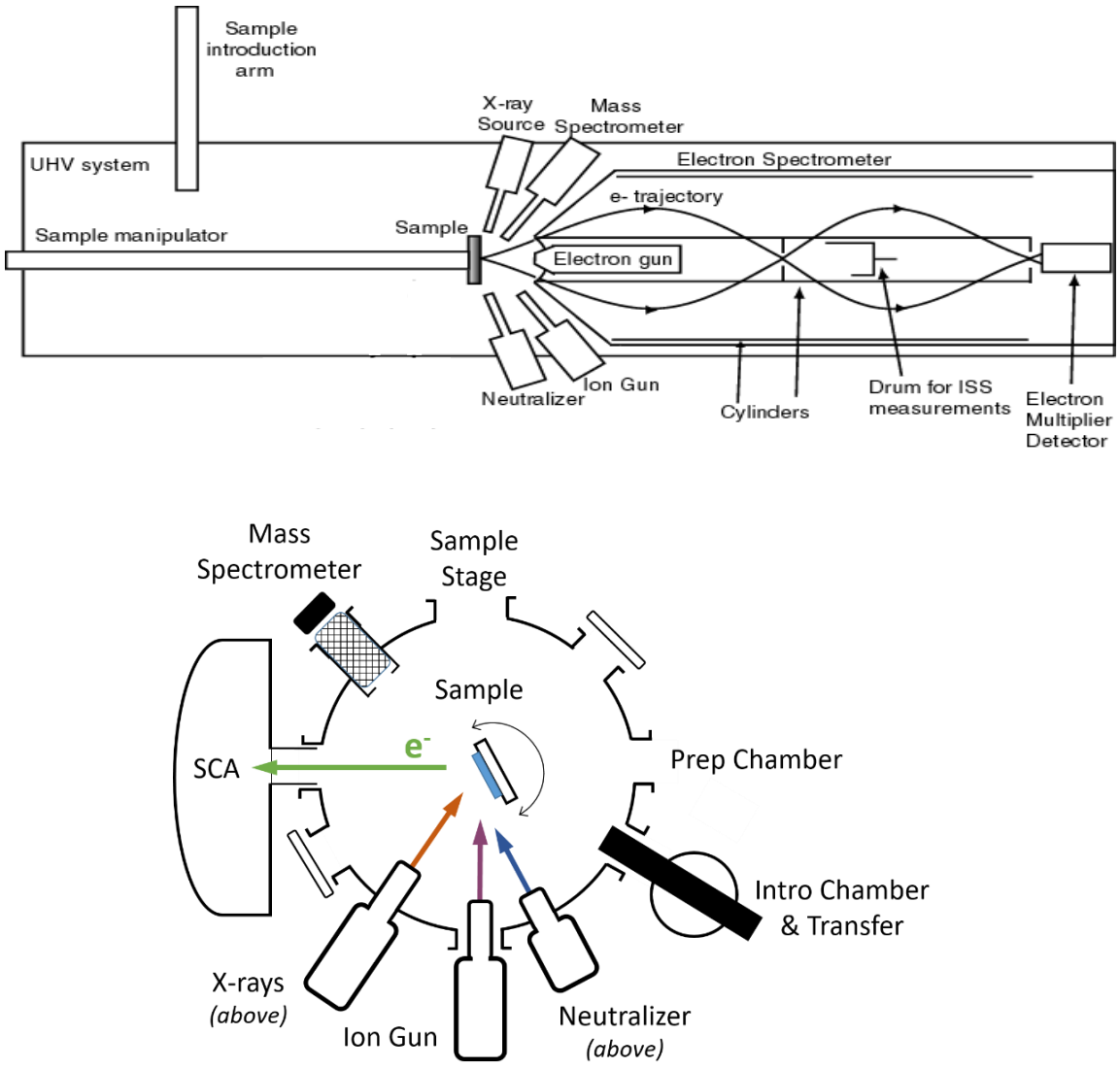

Figure S3: *Top: The PHI 560 XPS/SAM chamber with cylindrical mirror electron energy analyzer (adapted from Loeffler et al., 2008) was used for irradiation and characterization of the Toluca sample. The sample can be positioned for in-situ transfer, ion irradiation, and analysis using X-ray photoelectron spectroscopy (XPS). Bottom: The Versaprobe III, with integrated high-resolution imaging X-ray photoelectron spectrometer, ion gun, and sample introduction chamber was used for He^+ irradiation and characterization of the Canyon Diablo sample. Samples were irradiated at normal incidence, then rotated toward the SCA for XPS analysis. The X-ray source and neutralizer are mounted above, directed down onto the sample.*

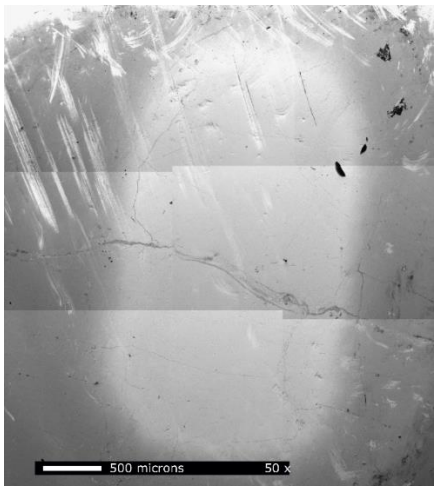

Figure S4. *Low-magnification (50x) SEM context image mosaic showing the irradiated region on Canyon Diablo, the relatively bright rectangle in the middle. The* Figure 1 *high-resolution (20,000x) images of Canyon Diablo were taken near the center of this area and in the region outside it.*

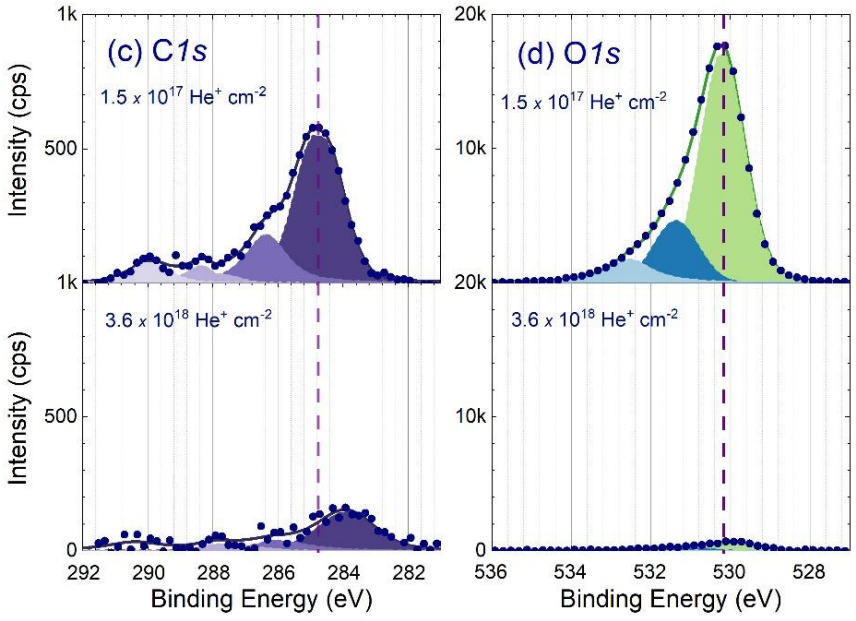

Figure S5: *High-resolution XPS spectra for C (a) and O (b) observed on Canyon Diablo described changes in chemistry with He fluence. (a) The C-1s photoelectron peaks show*

surficial adventitious carbon, with C-C and C-H bonds (dark purple) and smaller concentrations of C-O (medium purple), C=O (light purple) and other hydrocarbons (lavender). After irradiation, most of the carbon has been removed except recoil implanted atoms; the small (~1 eV) shift to lower binding energy for the C-C feature indicates the formation of minor Fe-carbide or graphitic-type molecules. (b) Fe(II)-O and Fe(III)-O (light-olive) features appear at ~530.2 eV, typical for metal oxide. Oxygen at higher binding energy derives from OH (531.4 eV; blue) and adsorbed H_2O (532.6 eV; light-blue) on the surface. Ion irradiation efficiently removes the surface oxides.

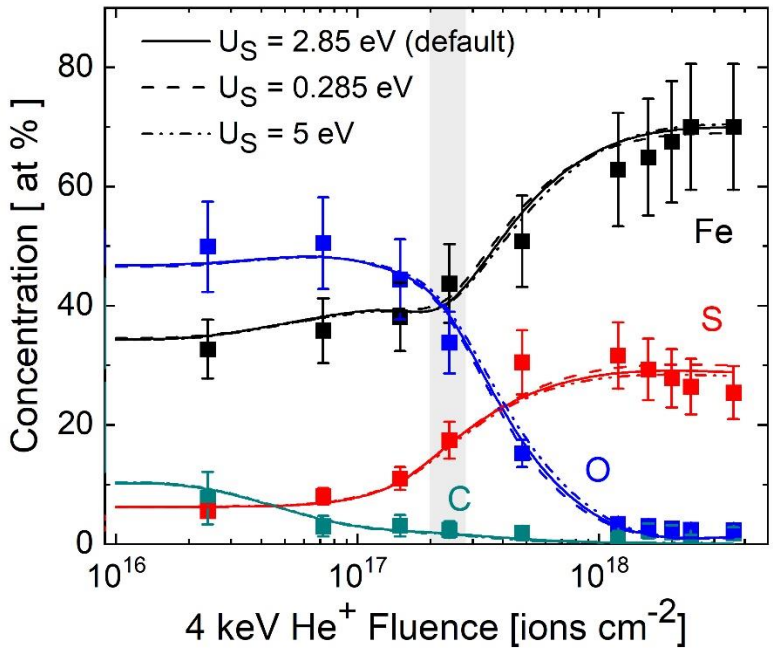

Figure S6: *Variation of the surface binding energy of sulfur had a minimal effect on surface compositional changes of the simulated target from 4 keV He^+ irradiation in SDTrimSP. No significant difference is noted either with U_s independent of surface composition or weighted by molecular concentration. Diffusion is included in these simulations.*

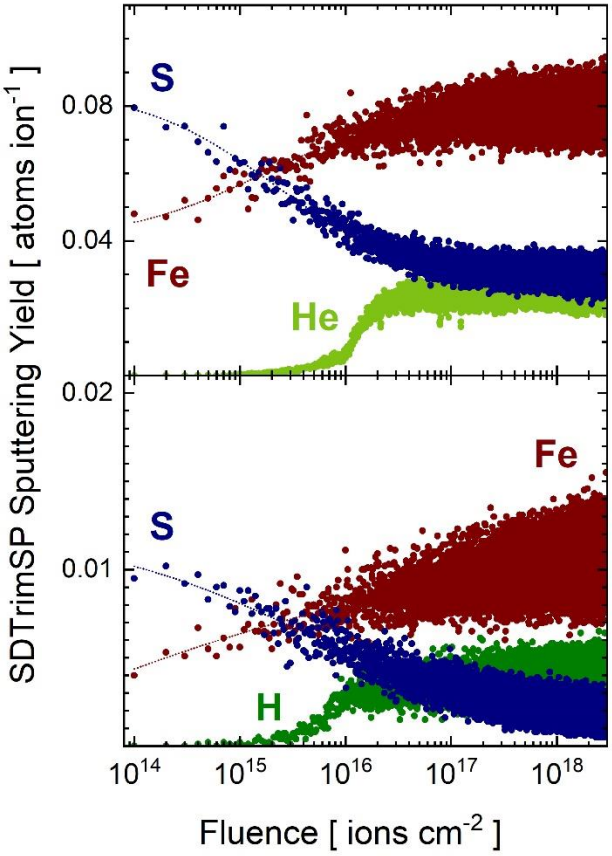

Figure S7: *The sputtering yields for constituent atoms and projectiles at low fluence through steady-state values were calculated for Psyche-relevant solar-wind ion fluxes using a mixture of (a) 4 keV He^+ and (b) 1 keV H^+ incident on troilite using SDTrimSP. The total ion flux at 2.9 A.U. was estimated to be 2.4 × 10^7 ions cm^{-2} s^{-1}. The fluence-dependent yields are driven by changes in FeS surface composition, which becomes significantly enriched in Fe after a fluence > 10^{16} ions/cm^2. Diffusion was included in these simulations, with coefficients extrapolated from XPS data as described in the primary text. Atomic heat of sublimation was used for surface binding energies. For unaltered troilite, the sputtering yields for sulfur and iron are 0.08 S/He^+, 0.01 S/H^+, 0.046 Fe/He^+ and 0.004 Fe/H^+, while equilibrium (> 10^{17} ions cm^{-2}) values are 0.03 S/He^+, 0.002 S/H^+, 0.08 Fe/He^+ and 0.01 Fe/H^+. Implanted helium and protons are sputtered (or outgassed) from troilite at 0.025 He/He^+ and 0.004 H/H^+, respectively, in equilibrium.*